Technical Physics Letters, Vol. 29, No. 8, 2003, pp. 617–619. Translated from Pis'ma v Zhurnal Tekhnicheskoĭ Fiziki, Vol. 29, No. 15, 2003, pp. 1–8.

Diffraction of Combined Optical Vortices

A. V. Volyar and T. A. Fadeeva

Tauride National University, Simferopol, Ukraine

Received January 28, 2003

Abstract—The diffraction of light on the lens of a Gaussian beam past a uniaxial crystal is equivalent to the beam diffraction on a helicoidal phase grating of two partial beams with different curvatures of the wave front. This diffraction significantly distorts the Gaussian beam profile and an extended region with three beam waists is formed near the focal plane. The beam waist region can be rectified by varying the radii of the primary beam waist and the lens pupil. *© 2003 MAIK "Nauka/Interperiodica".*

The unique ability of singular beams of trapping, carrying, and rotating microscopic particles of matter with dimensions from a few microns to several tens of microns [1] is indicative of the existence of an effective potential well, the shape and size of which can vary during the beam propagation. A three-dimensional profile of this potential well allows a number of particles to be trapped and structured simultaneously [2], thus forming sufficiently complicated spatial patterns. The synthesis of laser beams for such devices (called laser forceps) is based on the use of phase gratings significantly modifying the structure of the primary Gaussian beam. The modified beam is frequently erroneously also considered as Gaussian [3]. However, focusing such a singular beam on a lens can dramatically change the shape of the effective potential well.

In this paper, we will consider the case of singular beams with a composition close to that described in [3]. Recently [4], we demonstrated the possibility of obtaining optical vortices by passing a primary circularly polarized Gaussian beam with a zero topological charge $l = 0$ along the optical axis of an anisotropic crystal. If a quarter-wave plate and an analyzer with the axes mutually rotated by $\beta = \pi/4$ are placed past the crystal, an optical vortex with a double topological charge is formed on the beam axis. However, the beam structure is subject to changes in the course of subsequent propagation. This work is aimed at studying the diffraction of such a singular beam focused with a thin spherical lens.

Consider the field of a circularly polarized paraxial Gaussian beam passed along the optical axis z through a uniaxial crystal. The wave function of this beam can be written as [4]

$$\Psi_l(r, \varphi, z) = \frac{1}{\xi}\left(\frac{r}{\xi}\right)^{|l|}\exp\left(-\frac{r^2}{\rho^2\xi}\right)\exp[il\varphi]\exp(-ikz)\begin{pmatrix} g_x \\ g_y \end{pmatrix}, \quad (1)$$

where $\xi = 1 + iz/z_0$; $z_0 = k\rho^2/2$ is the Rayleigh length; ρ is the beam waist radius; k is the wavenumber; $g_x = \cos\delta/2 + i\sin\delta/2\exp(i\sigma 2\varphi)$ and $g_y = i\sigma[\cos\delta/2 - i\sin\delta/2\exp(i\sigma 2\varphi)]$ are elements of the Jones column vector; $\delta = k\Delta n r^2/\sqrt{r^2 + L^2} \approx 2\alpha r^2$; $\alpha = k\Delta n/2L$ is the phase difference (caused by the crystal anisotropy) between local orthogonal components of the electric field; $\Delta n = n_e - n_o$ (n_e and n_o being the extraordinary and ordinary refractive indices); l is the topological charge, r and φ are the radial and azimuthal coordinates, respectively; $\sigma = \pm 1$ is the direction of circulation of the electric field vector (helicity); and L is the crystal thickness along the z axis (it is assumed that the crystal entrance face $z = 0$ coincides with the beam waist plane).

Let us place a lens with the focusing distance f and the aperture radius r_0 at a distance of d from the entrance face of the crystal and consider the process of beam focusing. For each polarization component $\Psi^{(x, y)}$, the field at each point (r', φ', z) in the space behind the crystal can be described in terms of the Kirchhoff integral [5], whereby the beam wave function has the form

$$\Psi^{(x, y)}(r', \varphi', z) = \frac{iA}{\lambda q_2^{|l|+1}}\exp(-ikr'^2/2z)\exp(-ik[z + d])$$
$$\times \int_0^{2\pi} d\varphi \exp\left\{i\frac{kr'}{z}r\cos(\varphi - \varphi')\right\}$$
$$\times \int_0^{r_0} dr\{[a_0^{x, y}\cos\alpha r^2\exp(il\varphi) \quad (2)$$
$$+ b_0^{x, y}\sin\alpha r^2\exp(i\{l + 2\sigma\})\varphi]$$
$$\times \exp[-ikr^2(1/q_2 + 1/z)/2]r^{|l|+1}\},$$

where $b = kr'/z$, $a_0^x = 1$, $a_0^y = i\sigma$, $b_0^x = i$, $q_1 = q + d$, and $1/q_2 = 1/q_1 - 1/f$. For the sake of simplicity, we will consider two variants of diffraction frequently encountered in applications, with the beam waist radius being (i) much smaller than the lens aperture radius ($r_0 \gg \rho$,

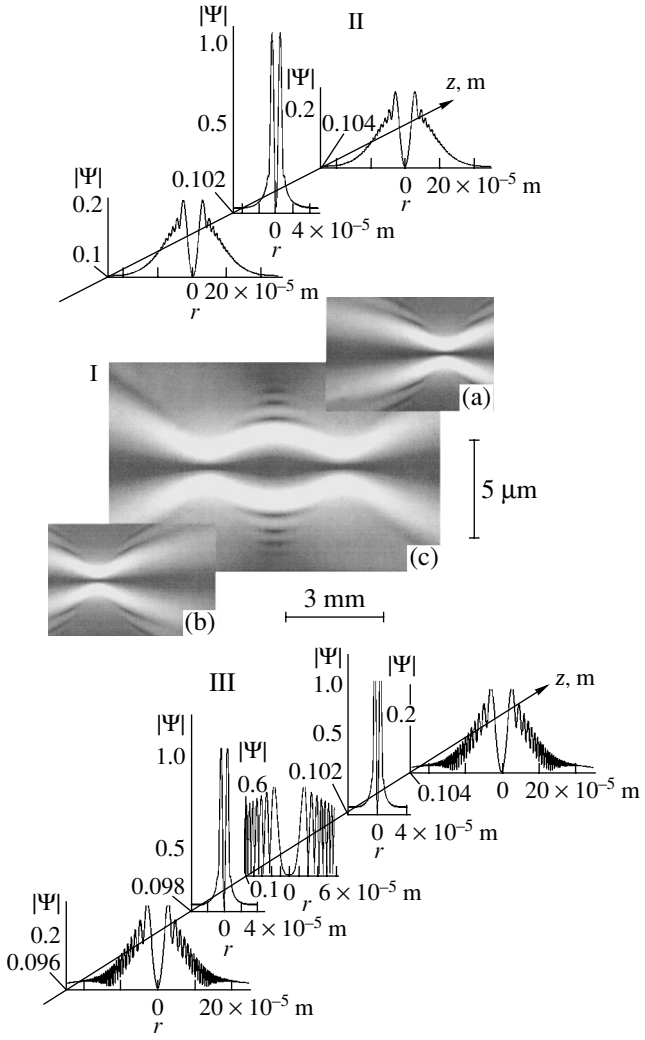

Fig. 1. Free beam diffraction: (I) a meridional section of the amplitude modulus for a paraxial beam with (a) α^+, (b) α^-, and (c) combined beam; (II) evolution of the partial beam amplitude profile with α^+; (III) evolution of the combined beam amplitude profile.

$\rho \gg \lambda$) and (ii) comparable with the aperture radius ($r_0 \propto \rho$, $\rho \gg \lambda$).

Free beam focusing ($r_0 \gg \rho$, $\rho \gg \lambda$). In this case, the wave function (2) can be rewritten as

$$\Psi_{x,y}^{(l\sigma)}(r', \varphi', z) = (i)^{l+1}\frac{kA}{2q_2^{|l|+1}}\exp(-ikr'^2/2z) \times \exp(-ik[z+d])\exp(il\varphi')\{a_0^{x,y}[D^{(+)}(r', z) + D^{(-)}(r', z)] + (i)^{2\sigma+1}b_0^{x,y}\exp(i2\sigma\varphi')[D_{(l\sigma)}^{(+)}(r', z) - D_{(l\sigma)}^{(-)}(r', z)]\}, \quad (3)$$

where

$$D_{(l\sigma)}^{\pm} = \int_0^\infty r^{|l|+1}J_{|l+2\sigma|}(br)\exp(-iCr^2) = 2^{|l|+1}\gamma(|l|+2, b^2/i4C)/b^{|l|+2}, \quad l\sigma \geq 0,$$

$$D^{\pm} = \int_0^\infty r^{|l|+1}J_{|l|}(br)\exp(-iCr^2)dr = b^{|l|}/[2^{l+1}(iC)^{|l|+1}]\exp[ib^2/4C].$$

Here, the index (+) corresponds to $C = C_1 + \alpha$, $C_1 = k(1/q_2 + 1/z)/2$; the index (–) corresponds to $C = C_1 - \alpha$; $\gamma(n, z)$ is the incomplete gamma function; and $J_n(x)$ is the nth-order Bessel function of the first kind.

When a clockwise circularly polarized ($\sigma = +1$) fundamental Gaussian beam ($l = 0$) passes through a uniaxial crystal and then through a quarter-wave plate and an analyzer (e.g., as in [4]), the beam wave field exhibits special regions (optical vortices) with spatial positions depending on the mutual orientation of the optical axes of the plate and the polarizer. If the axes make an angle of $\beta = \pi/4$, the wave function [6] retains only the term at b_0 and can be written in the following form:

$$\Psi^{(0)}(r', \varphi', z) = 4\frac{ik}{z}\frac{A}{q_2}\exp[-ik(d+z)]\exp\left[-i\frac{kr'^2}{2}\frac{q_3 - \frac{\zeta^2}{z}}{q_3^2 - \zeta^2}\right] \times \exp(i2\varphi')\left\{\left[(B_1 - B_2) + i\frac{z^2}{k^2r'^2}\right]\exp(-iB) - \left[(B_1 + B_2) + i\frac{z^2}{k^2r'^2}\right]\exp(iB)\right\}, \quad (4)$$

where

$$\zeta = 2\alpha z q_2/k, \quad B_1 = \frac{zq_3q_2}{2k(q_3^2 - \zeta^2)}, \quad B_2 = \frac{\alpha q_2^2 z^2}{k^2(q_3^2 - \zeta^2)},$$

$$B = \frac{\alpha q_2^2 r'^2}{(q_3^2 - \zeta^2)}, \quad q_3 = q_2 + z$$

and the incomplete gamma function was expressed as $\gamma(2, x) = 1 - (1 + x)e^{-x}$.

Near the optical axis ($kr' \ll 1$), the quantity in braces in Eq. (4) is proportional to the radius squared ($\{\ldots\} \propto r'^2$) and, hence, $\Psi^{(0)} \propto r'^2e^{i2\varphi'}$. This implies that an optical vortex with a double topological charge exists near the axis in the transmitted wave (as well as in the primary wave). As the radius r' increases, the shape of the initial Gaussian envelope of the wave function is significantly distorted. The term in braces in Eq. (4) has two components corresponding to the contributions of two beams forming the combined beam under consideration. Indeed, the diffraction integral (2) in fact contains two initial wave functions (differing by the sign of the parameter α in the amplitude and phase) and can be separated into two integrals. Each of these integrals represents a differential transformation of the

primary Gaussian beam on the phase grating with a helicoidal relief $T = \exp(i2\varphi + ikz)$. Since each beam is characterized by its own curvature of the wave front (determined by the parameter α), the two beams will be differently focused by the lens.

The beam focusing is illustrated in Fig. 1. Here, each partial beam is focused within a certain region at the plane $z = f$ (Fig. 1, Ia and Ib). As the partial beam with α^+ approaches the waist (Fig. 1, II), oscillations of the amplitude modulus change to a smooth behavior of the envelope; after the waist, the envelope oscillations arise again. Adding the two beams in the combined wave yields two foci on both sides of the focal plane $z = f$ (Fig. 1, Ic). Figure 1, III shows evolution of the amplitude profile for a combined singular beam. Note that the system of ring dislocations (toroidal vortices) is formed only in the focal plane $z = f$, whereas no phase singularities are present in the side waist planes.

Singular beam confined by a circular lens aperture ($r_0 \propto \rho$, $\rho \gg \lambda$). In this case, the wave function acquires the following form:

$$\Psi_{x,y} = ikA\exp[ik(z+d)] \times \exp(-ikr'^2/2z)I^{(b)}_{x,y}\exp(i2\varphi')/q_2, \quad (5)$$

where

$$I^{(b)}_{x,y} = -i[\exp-\{i(C_1+\alpha)r_0^2\} - \exp\{-i(C_1-\alpha)r_0^2\}]J_0(br_0)/b^2 + [1/b^2 - i(B_1-B_2)]\{U_1(w^+,u) + iU_2(w^+,u)\} - [1/b^2 - i(B_1+B_2)]\{U_1(w^-,u) + iU_2(w^-,u)\},$$

$w^{\pm} = 2(C_1 \pm \alpha)r_0^2$, $u = br_0$, and $U_m = (w, u)$ is the Lommel function of two arguments [6].

Similarly to the first case, a purely screw dislocation is present on the beam axis. However, the peripheral toroidal vortices are displaced from the central focal plane by the new toroidal vortices generated as a result of interference of the main beam and two diffracted edge waves. Small changes in the lens aperture induce a chain of dislocation reactions leading to the generation and annihilation of ring dislocations and to additional distortions of the envelope. Nevertheless, these very distortions allow the shape of the waist region to be controlled, which is especially important for the singular beams used in the optical forceps.

Figure 2 shows one of the possible methods of "rectification" of the focal waist region. We have fixed the lens pupil radius r_0 and varied the beam waist radius on the lens. For comparison, the central panel shows a meridional section of the beam with a waist radius much smaller than the aperture radius. When the r_0/ρ ratio is large, the edge waves form an involved pattern around the beam channel (Fig. 2b). As the r_0/ρ value decreases, the beam appears as rectified (Figs. 2c and 2d)

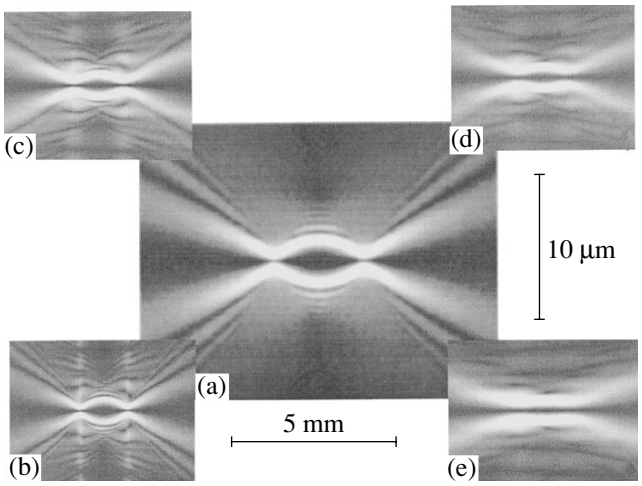

Fig. 2. Meridional sections illustrating rectification of the combined beam waist by varying the primary beam waist to the lens aperture ratio: $r_0/\rho = 10$ (a), 3 (b), 2 (c), 1.5 (d), 1 (e).

under the joint action of the toroidal vortices closest to the axis in the plane of three waists. For $r_0 = \rho$ (Fig. 2e), the beam exhibits virtually no divergence over about 3 mm (at a focal spot size of $\rho_f \approx 3$ μm).

Thus, we have demonstrated that a singular beam, despite possessing a Gaussian shape at the exit from a crystal, exhibits a significant change in the beam structure in the course of subsequent propagation; in particular, it forms three waists near the geometric focus. The shape of these waists can be controlled by varying the radii of the primary beam waist and the lens aperture. It should be noted that the character of diffraction is independent of the position of the polarization filter: displacement of the filter along the whole diffraction zone does not change the potential well profile.

REFERENCES

1. N. R. Heckenberg, M. E. J. Friese, and N. H. Rubinsztein-Dunlop, *Optical Vortices*, Ed. by M. Vasnetsov and K. Staliunas (Nova Science, New York, 1999).
2. M. P. MacDonald, L. Paterson, K. Volke-Sepulveda, *et al.*, Science **296**, 1101 (2002).
3. D. Ganic, X. Gan, M. Gu, *et al.*, Opt. Lett. **27**, 1351 (2002).
4. A. V. Volyar, T. A. Fadeeva, and Yu. A. Egorov, Pis'ma Zh. Tekh. Fiz. **28** (22), 70 (2002) [Tech. Phys. Lett. **28**, 958 (2002)].
5. D. Marcuse, *Integrated Optics* (IEEE Press, New York, 1973; Mir, Moscow, 1974).
6. G. N. Watson, *Treatise on the Theory of Bessel Functions* (Cambridge University Press, Cambridge, 1952; Inostrannaya Literatura, Moscow, 1949).

Translated by P. Pozdeev

Technical Physics Letters, Vol. 29, No. 8, 2003, pp. 620–623. Translated from Pis'ma v Zhurnal Tekhnicheskoĭ Fiziki, Vol. 29, No. 15, 2003, pp. 9–16.

Electron Photodetachment from the 1*s* Shell of a Negative Lithium Ion

V. K. Ivanov, K. V. Lapkin, and M. A. Kulov

St. Petersburg State Polytechnical University, St. Petersburg, Russia

e-mail: ivanov@tuexph.stu.neva.ru; const@tuexph.stu.neva.ru

Received March 17, 2003

Abstract—We have calculated the cross sections for electron photodetachment from the 1*s* shell of a negative lithium ion. The main attention is given to the behavior of the 1*s* electron ionization cross section near and above the threshold with simultaneous excitation of the outer 2*s* electron to a discrete state. The results are compared to the experimental data and to the values obtained within the framework of the R-matrix formalism [Phys. Rev. Lett. **87**, 023001 (2001)] predicting unusually strong resonances in the cross section. © *2003 MAIK "Nauka/Interperiodica".*

Recent calculations of the photodetachment cross sections for the 1*s* core shell electrons of Li^- ion within the framework of the R-matrix formalism [1] predicted the existence of strong (~40 Mb) resonances both near and above the 1*s* ionization threshold. Among the over-threshold resonances, the maximum cross section (~20 Mb) was attributed to the photodetachment of 1*s* electrons with simultaneous excitation of the outer 2*s* electron to a 2*p* state of neutral lithium. Since the resonance behavior of the photodetachment cross section dominated over the background, it was suggested [1, 2] that physical processes in the core shells of negative ions are basically different from the analogous processes in neutral atoms.

Subsequent experimental determinations of both absolute [3] and relative [2] cross sections also revealed some resonances above the 1*s* ionization threshold, but these values were significantly smaller than theoretical predictions. Moreover, experiments showed no resonances at the 1*s* threshold. Analogous results were obtained for the 2*p* shell of Na^- ion [4].

The aim of our study was to calculate the photodetachment cross section for 1*s* electrons of Li^- ion near the ionization threshold within the framework of the many body theory [5, 6] and, in particular, to consider the process of 1*s* level ionization with simultaneous excitation of the outer 2*s* electron to the nearest excited 2*p* state of neutral lithium.

Let us consider two reaction channels in the dipole approximation:

$$Li^-(1s^22s^2) + \omega \longrightarrow Li^*(1s2s^2) + \varepsilon p, \qquad (1a)$$

$$Li^-(1s^22s^2) + \omega \longrightarrow Li^*(1s2s2p) + \varepsilon l', \qquad (1b)$$

where ω is the photon energy, ε is the electron energy in the continuum, and l' corresponds to the *s* and *d* states in the continuum. The cross sections of both processes can be calculated using the conventional formulas (here and below, we use the atomic system of units with $\hbar = e = m = 1$ and energies are expressed in Rydbergs; see, e.g., [5]):

$$\sigma^{(r,\nabla)}_{nl\to\varepsilon l'}(\omega) = \frac{4\pi^2\alpha}{3}\frac{N_{nl}\omega}{2l+1}\left|D^{(r,\nabla)}_{nl\to\varepsilon l'}\right|^2, \qquad (2)$$

where α is the fine structure constant, N_{nl} is the number of electrons in the nl state, and $D^{(r,\nabla)}_{nl\to\varepsilon l'}$ is the reduced amplitude of the $nl \longrightarrow \varepsilon l'$ transition calculated using the length and velocity operators with allowance for multielectron correlations.

The amplitudes and matrix elements are calculated using the Hartree–Fock (HF) wave functions as the basis set. However, the one-electron HF energies of the ground state of a negative lithium ion ($E_{1s} = -63.21$ eV and $E_{2s} = -0.40$ eV) significantly differ from the experimental binding energies ($E_{\exp 1s} = -56.9$ eV and $E_{\exp 2s} = -0.618$ eV) [3, 7]. In order to refine the binding energies and the corresponding wave functions of the ground state, it is necessary to go outside the HF approximation. In particular, the exact one-particle wave functions ϕ_E and energies can be determined from an integral equation obtained from the Dyson equation for a one-particle Green's function [8]:

$$\hat{H}^{(0)}\phi_E(\mathbf{r}) + \int\Sigma_E(\mathbf{r},\mathbf{r}')\phi_E(\mathbf{r}')d\mathbf{r}' = E\phi_E(\mathbf{r}). \qquad (3)$$

Here, $\hat{H}^{(0)}$ is the HF Hamiltonian of the ion, $\Sigma_E(\mathbf{r},\mathbf{r}')$ is the self-energy part of the one-particle Green's func-

tion, playing the role of a nonlocal energy-dependent potential. In our study, this potential is calculated in the second-order perturbation theory using a basis set of the HF wave functions. In the diagram representation, the matrix element $\Sigma_E(\mathbf{r}, \mathbf{r}')$ of a part between states i and i' has the following form:

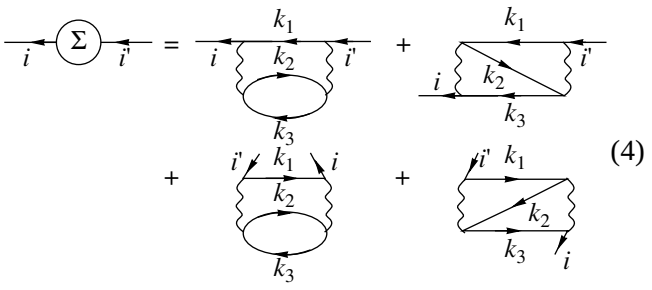

(4)

where the lines with arrows pointing leftward (rightward) correspond to a hole (particle) and wavy lines correspond to the Coulomb interaction. The first two terms correspond to the direct and exchange interactions for the forward time processes, while the next two terms represent the same for the reverse time processes. The summation and integration is performed over all intermediate k_1, k_2, and k_3 states. Physically, these diagrams describe the polarization of core electrons under the action of the 1*s* electron studied.

The matrix element (4) is analytically expressed as follows:

$$\langle i|\Sigma_E|i'\rangle = \left(\sum_{\substack{k_1>F\,k_2>F\\ k_3\le F}}\sum + \sum_{\substack{k_1\le F\,k_2\le F\\ k_3>F}}\sum\right) \times \frac{\langle i, k_3|\hat{U}|k_2, k_1\rangle\langle k_1, k_2|\hat{V}|k_3, i'\rangle}{E - E_{k_1} - E_{k_2} + E_{k_3} + i\delta(1-2n_{k_1})}, \quad (5)$$

where $\langle \hat{V} \rangle$ is the Coulomb matrix element, $\langle \hat{U} \rangle$ is the combined matrix element including both direct and exchange interactions [5], E_k is the energy of the kth state, and n_k is a step function. The polarization potential was calculated for the 1*s* and 2*s* states of Li^- ion, taking into account monopole, dipole, quadrupole, and octupole terms in expression (5). This potential was substituted into the Dyson equation (3), which was solved to find the new wave functions (Dyson orbitals) and energies. The new values of the ground state energy proved to be much closer to the experimental data: $E_{D1s} = -57.5$ eV and $E_{D2s} = -0.59$ eV.

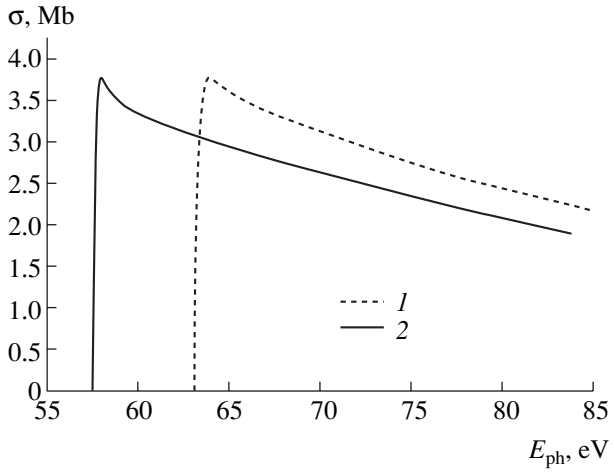

Fig. 1. The cross section for 1*s* electron photodetachment from Li^- ion calculated using (*1*) the RPE approximation and (*2*) the same with the Dyson wave functions of the ground state (E_{ph} is the photon energy).

The dipole amplitudes $D^{(r,\nabla)}_{1s\to\varepsilon p}$ were calculated in the random phase exchange (RPE) approximation [5]:

$$\langle \varepsilon p|\hat{D}(\omega)|1s\rangle = \langle \varepsilon p|\hat{d}|1s\rangle + \sum_{\substack{k_3\le F\\ k_4>F}}\left(\frac{\langle k_2|\hat{D}(\omega)|k_1\rangle\langle k_1, \varepsilon p|\hat{U}|k_2, 1s\rangle}{\omega - E_2 + E_1 + i\delta} - \frac{\langle k_1|\hat{D}(\omega)|k_2\rangle\langle k_2, \varepsilon p|\hat{U}|k_1, 1s\rangle}{\omega + E_2 - E_1 - i\delta}\right), \quad (6)$$

where $\langle \hat{d} \rangle$ is the dipole matrix element in the one-particle approximation. The $D^{(r,\nabla)}_{1s\to\varepsilon p}$ values were determined for two sets of the ground state wave functions: HF and Dyson orbitals. The wave functions of excited states in the continuum were obtained within the framework of the frozen core HF approximation.

The results of our calculation of the cross section of process (1a) in the RPE approximation (Fig. 1) show a behavior typical of the photoionization cross section in the vicinity of a core shell threshold, with a small maximum at the 1*s* threshold followed by the gradual decay with increasing photon energy E_{ph}. No significant difference in behavior, except the anticipated energy shift, is observed on the passage from pure HF basis set (RPE) to the Dyson orbitals for the ground state of the negative ion (RPE + Dyson).

In order to consider the process of photodetachment (1b) involving $2s \longrightarrow 2p$ excitation, we used the

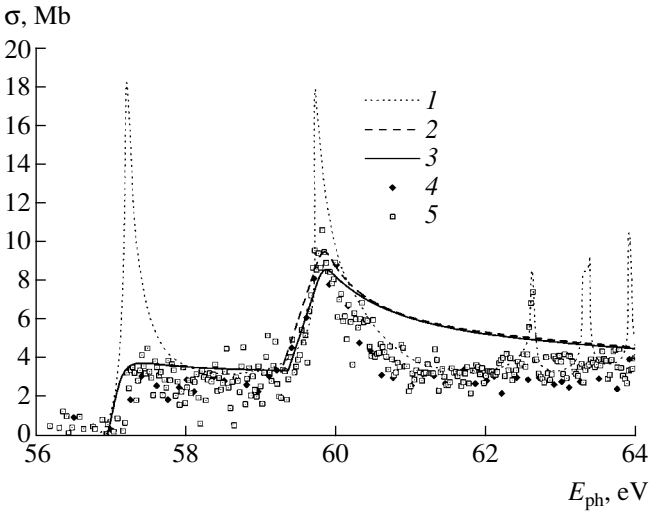

Fig. 2. The cross section for 1*s* electron photodetachment from Li^- ion: (*1*) calculation using the R-matrix formalism; (*2*) calculation with the *s*, *p*, *d* wave functions in the field of the Dyson frozen core; (*3*) calculation using the *p* wave function in the field of the Dyson frozen core and the *s*, *d* wave functions reconstructed in the field of the Li $1s2s2p$ state (theoretical $1s2s2p$ excitation threshold shifted by 0.5 eV); (*4*) experimental data from [3]; (*5*) experimental data from [2].

following diagrams of the perturbation theory:

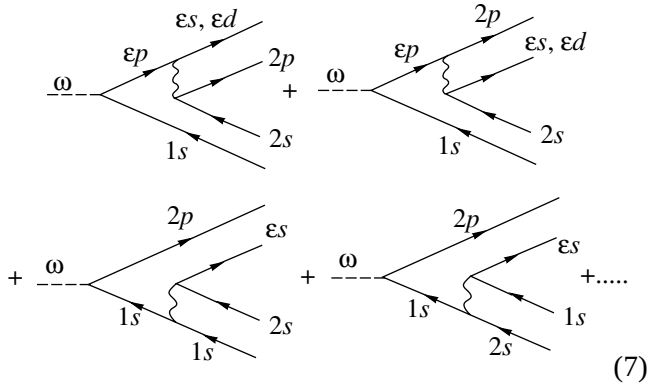

(7)

Here, the dashed lines correspond to the impinging photon, while a block at the vertex takes into account the RPE correlations for the amplitude of the photoeffect. The first two amplitudes describe the photoionization process, whereby one photoelectron excites another, while the other two amplitudes refer to the shake-up process.

The amplitudes according to diagrams (7) were calculated using the Dyson wave functions for the 1*s* and 2*s* hole states and various wave functions of the excited states. The wave functions of the electron excited to the 2*p* state of Li^- cannot be obtained within the framework of the frozen core HF approximation. For this reason, we selected the 2*p* wave function corresponding to the excited $1s2s2p$ state of neutral Li calculated in the self-consistent HF approximation.

The wave functions of the escaping ε*p* electron in the intermediate state with amplitudes (7) were calculated using the HF approximation for two cases, corresponding to (a) the field of the frozen core of the ground state of Li^- with a hole in the 1*s* shell (the field of the Dyson $1s2s^2$ core) and (b) the field of a fully reconstructed $1s2s^2$ core [5]. In the latter case, we first used the self-consistent HF approximation to calculate the excited $1s2s^2$ state and then determined the ε*p* wave functions in the field of this state.

The wave functions of the final ε*s*, ε*d* states were also calculated using two methods. In the first case, these wave functions were determined in the field of the Dyson frozen core with a hole in the 1*s* shell. In the second case, the ε*s*, ε*d* wave functions were considered as representing an external electron moving in the field of the final $1s2s2p$ state of the fully reconstructed core.

The partial cross section for the process (1b) of photodetachment with excitation was determined using formula (2), in which the amplitude $D^{(r,\nabla)}_{nl\to\varepsilon l'}$ was replaced by that according to (7). The total photoionization cross section is a sum of two contributions, representing the partial cross sections of process (1a) (RPE + Dyson) and process (1b) with amplitudes (7).

The results of calculations of the total cross section for the photodetachment of 1*s* electrons with various wave functions of the *s*, *p*, *d* electrons and amplitudes (7) are presented in Fig. 2. An analysis of these data reveals two main features: (i) the behavior of the cross section at the threshold exhibits no strong resonance predicted in [1] and agrees well with the experimental data [2, 3]; (ii) all calculations predict a resonance in the cross section at a photon energy corresponding to opening of the channel $1s^22s^2 \longrightarrow 1s2s2p\varepsilon l$ (1b). However, the cross section peak according to our calculations is much smaller than that predicted in [1, 2] and shows a better agreement with experiment. The best fit is provided by using the wave functions calculated within the framework of the Dyson frozen core.

Note that experimental data indicate a more pronounced and symmetric resonance in the cross section for excitation of the 2*p* state, while our calculations predict a behavior that is closer to a usual step at the threshold. Apparently, a better agreement with experiment will be obtained by going beyond the first-order perturbation theory and taking into account the effect of the dynamic polarization of the core on the escaping photoelectrons (as it was done for the ground state). It should also be noted that, on the whole, the multielectron effects are more pronounced in the inner shells of negative ions than in neutral atoms.

Acknowledgments. The authors are grateful to Prof. M.Ya. Amusia for the discussion of results. This study was supported by the Ministry of Education of the Russian Federation, project no. E02-3.2-267.

REFERENCES

1. H. L. Zhou, S. T. Manson, L. VoKy, *et al.*, Phys. Rev. Lett. **87** (2), 023001 (2001).
2. N. Berrah, J. D. Bozek, A. A. Wills, *et al.*, Phys. Rev. Lett. **87** (25), 253002 (2001).
3. H. Kjeldsen, P. Andersen, F. Folkmann, *et al.*, J. Phys. B: At. Mol. Opt. Phys. **34**, L353 (2001).
4. A. M. Covington, A. Agilar, V. T. Davis, *et al.*, J. Phys. B: At. Mol. Opt. Phys. **34**, L735 (2001).
5. M. Ya. Amusia, *Atomic Photoeffect* (Plenum, New York, 1990; Nauka, Moscow, 1987).
6. V. K. Ivanov, J. Phys. B: At. Mol. Opt. Phys. **32** (12), R67 (1999).
7. T. Andersen, H. H. Andersen, P. Balling, *et al.*, J. Phys. B: At. Mol. Opt. Phys. **30**, 3317 (1997).
8. G. F. Gribakin, B. V. Gul'tsev, V. K. Ivanov, *et al.*, J. Phys. B: At. Mol. Opt. Phys. **23**, 4505 (1990).

Translated by P. Pozdeev

Technical Physics Letters, Vol. 29, No. 8, 2003, pp. 624–626. Translated from Pis'ma v Zhurnal Tekhnicheskoĭ Fiziki, Vol. 29, No. 15, 2003, pp. 17–23.

A Planar Excimer–Halogen Radiation Source Pumped by Transverse RF Discharge

A. K. Shuaibov, A. I. Dashchenko, L. L. Shimon, and I. V. Shevera*

Uzhgorod National University, Uzhgorod, Ukraine

** e-mail: ishev@univ.uzhgorod.ua*

Received January 8, 2003

Abstract—We present the characteristics of a planar source of wideband shortwave radiation pumped by transverse RF (f = 1.76 MHz) discharge in a Kr/Xe/Cl_2 mixture ($P \le 500$ Pa). The spectral characteristics of the plasma emission were studied in the wavelength interval of 130–600 nm. The oscillograms of the voltage, current, and output radiation intensity and the diagrams of the output power depending on the gas pressure, partial composition of the working gas mixture, and discharge power are presented. It is established that the source produces emission predominantly in the spectral interval of 170–330 nm, representing a system of the molecular emission bands XeCl(D, B–X), KrCl(B–X), Cl_2(D'–A'), and Cl_2^{**}. For a maximum output power in the UV–VUV range, the optimum working gas mixture is Kr/Xe/Cl_2 with the partial pressures P(Kr)/P(Xe)/P(Cl_2) = 150–200/150–200/20–40 Pa. The maximum power irradiated within a solid angle of 4π via two output holes with a total area of $S \le 100$ cm^2 reaches 30–40 W. In the region of a threshold with respect to the transverse discharge initiation, there are narrow peaks of plasma emission that are probably related to the jumps in the density of electrons and the positive and negative ions at the boundary between the plasma and the RF discharge layer. © *2003 MAIK "Nauka/Interperiodica".*

In most of the modern excimer–halogen electric discharge lamps, the active medium is formed by means of a longitudinal glow discharge and a pulsed-periodic discharge via a dielectric [1–3]. These discharges are predominantly generated in cylindrical quartz tubes, so that the working output aperture of the lamp is also cylindrical. Some applications in microelectronics and plasmachemical technologies require a uniform illumination of flat objects with high-power UV and vacuum UV (UV–VUV) radiation, which can be provided by planar excimer–halogen lamps. Some characteristics of such a planar lamp operating on the system of bands of XeCl* molecules were reported in [4], where the active medium was provided by a short glow discharge in Xe/Cl_2(HCl) mixtures (P < 2.0 kPa). The radiation was extracted via a perforated electrode, and the output characteristics were significantly limited by the pump current ($I_{ch} \le 10$ mA, greater currents destroy the grid electrode).

A promising active medium for the effective high-power sources of spontaneous emission with a planar output aperture, based on heavy inert gas halides and halogen dimers, is offered by transverse RF discharge. A low-current inductive RF discharge was successfully used for pumping XeCl lamps (employing a Xe/Cl_2 mixture at a total pressure of $P \le 500$ Pa) with a cylindrical working configuration [5]. In order to increase the output UV–VUV power and use the high emissivity of the near-electrode plasma layers, it is of interest to employ a high-current transverse RF discharge (TRFD) in an excimer–halogen lamp. At a small value of the *pd* parameter (where p is the pressure and d is the interelectrode distance), the TRFD plasma will comprise predominantly the near-electrode layers, which are essentially analogous to the near-cathode region of a longitudinal dc glow discharge [6] and are characterized by increased emission intensity as compared to the positive plasma column. Previously [7, 8], we obtained a relatively high output power and efficiency with an excimer–halogen lamp operating on a system of 195–200/257 nm [Cl_2^{**}] bands (He/Cl_2 mixture) and 195–200/222/257 nm bands (Kr/Cl_2 mixture) with an active medium formed in an extended plasma region of the confined negative cathode dc glow discharge.

Here we report the results of investigation of the working characteristics of a planar RF discharge source employing a krypton–xenon–chlorine gas mixture.

The TRFD was initiated in a volume of 17 × 3 × 2 cm^3 at an interelectrode spacing of d = 2.2 cm. The electrode system comprised a nickel-coated brass electrode (with a length of 17 cm and an end radius of 3 cm) and a flat nickel electrode. The TRFD electrodes were mounted on a dielectric flange inside a 10-liter discharge chamber. The spectra of the output radiation extracted via the edge of the discharge volume were measured using a vacuum monochromator (for $\Delta\lambda$ = 130–355 nm) or an MDR-2 monochromator (for $\Delta\lambda$ = 210–660 nm), both with a FEU-106 photomultiplier. The opposite edge of the plasma medium was moni-

tored with a pulsed photomultiplier of the Foton type connected to a pulsed oscillograph (S1-99) measuring the total plasma emission pulses.

The system was supplied from an RF voltage source with an average power of ≤300 W, which generated pulse trains with a maximum duration of 12 ms and an amplitude of 5–6 kV filled with the RF oscillations (f = 1.76 MHz). The high-voltage signal was applied to the electrode system via a blocking capacitor ($C_0 \leq$ 200 pF). The total power of the output UV–VUV radiation was measured via a side window using a method described elsewhere [9]. The voltage applied to the discharge gap was measured using a low-inductance capacitive divider, while the current pulses were detected using a low-inductance probe (R = 1–5 Ω). The experiments were performed with krypton of a spectroscopic purity grade and chlorine of a technical purity grade. The discharge chamber was preliminarily evacuated to a residual pressure of 3–5 Pa and passivated with chlorine. The lamp was operating without forced cooling of the electrode system or the working gas medium.

At a total pressure of the Kr/Cl_2 gas mixture in the interval from 100 to 500 Pa, the system featured a spatially homogeneous TRFD in which 50–70% was a bright plasma of the near-electrode layers containing all characteristic regions of a cathode part of the dc glow discharge [6]. The main contribution to the emission from a TRFD plasma was due to an extended negative cathode glow region. Investigation of the spectral characteristics of the TRFD plasma showed that the emission is predominantly concentrated in the wavelength interval 180–280 nm and has the shape of a broad band similar to that reported for a spontaneously initiated pulsed-periodic discharge in a Kr/Cl_2 mixture [10]. Because of a low pressure of the working gas mixture, the emission bands at 222 nm [KrCl], 257 nm [Cl_2(D'–A')] and 200 nm [Cl_2^{**}] were strongly broadened and superimposed onto each other. The main factor responsible for the band broadening is incomplete vibrational relaxation of the excited states of KrCl and Cl_2 molecules [11]. In the visible spectral range (λ = 400–600 nm), the emission was represented predominantly by the spectral lines of KrI(5s–6p).

Figure 1 presents the results of optimization of the average output power of the TRFD plasma emission with respect to the pumping power at various pressures of the krypton–xenon–chlorine gas mixture. All curves of the output radiation power versus the TRFD power monotonically increase. The output emission power also increased with the partial pressure of krypton in the interval from 80 to 400 Pa. At P(Kr) ≥ 400 Pa and $P(Cl_2) \geq 80$ Pa, the discharge could not be initiated. Increasing $P(Cl_2)$ above 40 Pa led to a decrease in the output radiation power. The optimum interval of $P(Cl_2)$ is from 20 to 40 Pa; more precise determination was limited by the possibilities of the gas admission and

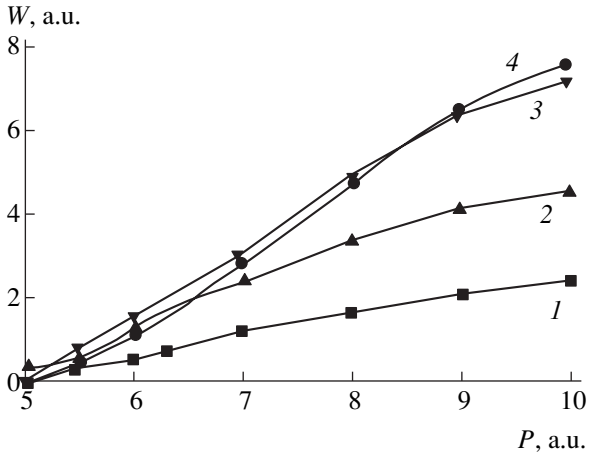

Fig. 1. Plots of the power of emission from TRFD plasma in a $Kr/Xe/Cl_2$ mixture versus the discharge power for P(Xe)/$P(Cl_2)$ = 80/40 Pa (*1*) and P(Kr)/P(Xe)/$P(Cl_2)$ = 80/80/40 (*2*), 200/80/40 (*3*), and 320/80/40 Pa (*4*).

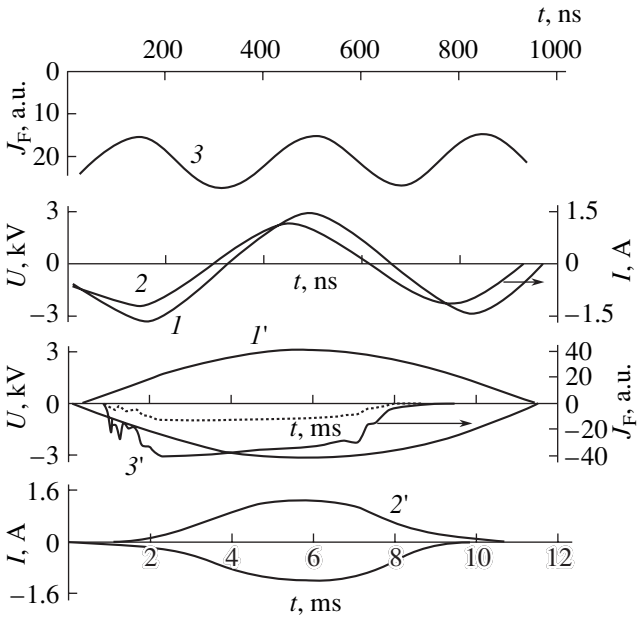

Fig. 2. Oscillograms of the (*1*, *1*') discharge voltage, (*2*, *2*') discharge current, and (*3*, *3*') emission intensity from the TRFD plasma in a $Kr/Xe/Cl_2$ mixture with P(Kr)/P(Xe)/$P(Cl_2)$ = 120/120/40. Curves *1*'–*3*' show the values averaged over the RF oscillation period.

evacuation system. For a TRFD in $Kr/Xe/Cl_2$ with a low chlorine content, the system exhibited an increase in the efficiency of emission at small; pumping powers ($W \leq$ 8 a.u., see curve *4* in Fig. 1).

Figure 2 shows oscillograms of the output radiation intensity from the TRFD plasma and the dynamics of the voltage and total emission averaged over the RF oscillation period. The emission was characterized by the constant and variable components. The frequency of the variable component was twice that of the RF

oscillations, and the pulse duration at the base reached 300 ns. An increase in the xenon pressure P(Xe) was accompanied by growth in the constant component in the total TRFD emission intensity (Fig. 2a). For a low-density plasma in mixtures of heavy inert gases with chlorine, the main channel of the excimer molecule formation is via the harpoon reaction [12], and the presence of a constant component may reflect the existence of a stationary channel of the formation of metastable krypton atoms in the TRFD plasma. An analysis of the behavior of the averaged radiation power revealed the appearance of a peak structure in the threshold region with respect to the supply voltage. The discharge in a low-pressure $Kr/Xe/Cl_2$ mixture is characterized by a single narrow peak; as the pressure is increased, the number of peaks increases to three, while the average breakdown voltage grows from 1.5 to 2.5 kV.

For a multicomponent plasma of electronegative gases under RF pumping conditions, it was theoretically predicted [13–15] that the density of electrons and the positive and negative ions must exhibit jumps at the boundaries between plasma regions with different parameters. For the TRFD, this is the plasma–RF discharge layer interface. Therefore, the appearance of a peak structure in the threshold region of the discharge initiation voltages can be related to the reactions of formation of excimer and Cl_2 molecules in the zones where the particle density exhibits jumps. More detailed explanation of the nature of the emission peaks requires numerical simulation of the TRFD in $Kr/Xe/Cl_2$ mixture under the conditions close to those used in our experiments.

Experimental evaluation of the total power of emission from the TRFD plasma within a solid angle of 4π showed that this value reaches up to 30–40 W.

Thus, we have established that heavy-current transverse RF discharge in a $Xe/Kr/Cl_2$ mixture offers a planar source of wideband shortwave radiation operating on the XeCl, KrCl, Cl_2(D'–A'), and Cl_2^{**} band system, with the predominant emission in the spectral interval of 180–330 nm. The optimum working gas mixture is $Kr/Xe/Cl_2$ with the partial pressures $P(Kr)/P(Xe)/P(Cl_2)$ = 150–200/150–200/20–40 Pa. The prototype source has two planar output apertures with a total area of about 100 cm^2. The average output radiation power reaches up to 30–40 W. In the threshold region with respect to the TRFD initiation, there are narrow peaks in the total plasma emission which are probably related to the jumps in the electron and ion density at the boundary between the plasma and the RF discharge layer.

REFERENCES

1. A. P. Golovitskiĭ and S. N. Kan, Opt. Spektrosk. **75**, 604 (1993) [Opt. Spectrosc. **75**, 357 (1993)].
2. A. K. Shuaibov, A. I. Dashchenko, and I. V. Shevera, Kvantovaya Élektron. (Moscow) **32**, 279 (2002).
3. M. I. Lomaev and V. F. Tarasenko, Proc. SPIE **4747**, 390 (2002).
4. E. A. Sosnin and V. F. Tarasenko, Zh. Tekh. Fiz. **67** (12), 43 (1997) [Tech. Phys. **42**, 1411 (1997)].
5. A. P. Golovitskiĭ, Pis'ma Zh. Tekh. Fiz. **24** (6), 63 (1998) [Tech. Phys. Lett. **24**, 233 (1998)].
6. Yu. P. Raĭzer and M. N. Shneider, Fiz. Plazmy **18**, 1176 (1992) [Sov. J. Plasma Phys. **18**, 762 (1992)].
7. A. K. Shuaibov, A. I. Dashchenko, and I. V. Shevera, Pis'ma Zh. Tekh. Fiz. **28** (6), 23 (2002) [Tech. Phys. Lett. **28**, 226 (2002)].
8. A. K. Shuaibov, A. I. Dashchenko, and I. V. Shevera, Ukr. Fiz. Zh. **47**, 346 (2002).
9. A. K. Shuaibov, L. L. Shimon, A. I. Daschenko, and I. V. Shevera, J. Phys. Stud. **5**, 131 (2001).
10. A. K. Shuaibov, A. I. Dashchenko, L. L. Shimon, and I. V. Shevera, Pis'ma Zh. Tekh. Fiz. **28** (16), 85 (2002) [Tech. Phys. Lett. **28**, 702 (2002)].
11. V. V. Datsyuk, I. A. Izmailov, and V. A. Kochelap, Usp. Fiz. Nauk **168**, 439 (1998) [Phys. Usp. **41**, 379 (1998)].
12. A. P. Golovitskiĭ and S. V. Lebedev, Opt. Spektrosk. **82**, 251 (1997) [Opt. Spectrosc. **82**, 227 (1997)].
13. V. A. Shveĭgert, Fiz. Plazmy **17**, 844 (1991) [Sov. J. Plasma Phys. **17**, 493 (1991)].
14. I. D. Kaganovich and L. D. Tsendin, Fiz. Plazmy **19**, 1229 (1993) [Plasma Phys. Rep. **19**, 645 (1993)].
15. I. D. Kaganovich, Fiz. Plazmy **21**, 434 (1995) [Plasma Phys. Rep. **21**, 410 (1995)].

Translated by P. Pozdeeev

Technical Physics Letters, Vol. 29, No. 8, 2003, pp. 627–628. Translated from Pis'ma v Zhurnal Tekhnicheskoĭ Fiziki, Vol. 29, No. 15, 2003, pp. 24–28.

Synthesis, Structure, and Some Physical Properties of Carbon and Chromium Deposits Possessing a Fractal Structure

Yu. V. Sokolov and V. S. Zheleznyĭ

Voronezh State Technical University, Voronezh, Russia

e-mail: www/falcon@mail.ru

Received March 19, 2003

Abstract—Experimental data obtained by scanning electron microscopy show that a carbon deposit formed during graphite spraying in an electric arc and chromium particles obtained by electrochemical deposition under certain conditions possess similar fractal structures. Data on some physical properties, the size of fractal aggregates, and the fractal dimensions of carbon and chromium deposits are presented. A possible mechanism of the fractal structure formation is discussed. © *2003 MAIK "Nauka/Interperiodica".*

In recent years, much attention has been given to objects possessing fractal structures. The interest in these structures is related to at least two circumstances [1]. First, fractal aggregates are frequently encountered in nature. Second, such aggregates are the main structure-forming elements in a number of macroscopic systems developed in the course of various physicochemical processes and phenomena. Application of the fractal geometry concept dates back to the basic investigations of Mandelbrot [2]. Our knowledge about the structure and properties of fractal objects are based mostly on the existing theoretical models.

We have studied a carbon deposit obtained by spraying graphite rods in an electric arc and chromium aggregates obtained by electrochemical deposition under certain conditions. Both objects possess a similar cloudlike fractal structure.

The carbon deposit was synthesized under the following conditions. The working chamber of a reactor was evacuated to 10^{-2} Torr and filled with argon to a pressure varied within 500–600 Torr. Then a graphite electrode, shaped as a rectangular rod with 5×3 mm cross section and 100 mm length, was sprayed in an electric arc at an applied voltage of 15–20 V and a current of 170–190 A. The time of carbon deposition on an immobile graphite electrode was varied from 10 to 180 s. The carbon deposit formed in the region of contact appeared as a silver-bright ring with a thickness of 1–3 mm, depending on the arc operation time.

The fractal aggregates of chromium were obtained by electrochemical deposition in a cell with nonconsumable lead electrode at $T = 44$–55°C in an electrolyte representing a mixture of CrO_3 (250 g/l) and H_2SO_4 (2.5 g/l) solutions. The dc current density was 0.3 A/cm^2 and the applied voltage was 9–10 V. The chromium deposit was obtained on the cathode at a rate of 13 μm/h during a deposition time of 18–20 h.

The fractal structures of carbon and chromium deposits were studied in a scanning electron microscope (SEM) operating in secondary electron mode. Figures 1a and 1b show the SEM images of a carbon deposit with a magnification of ×8700 (a) and ×310 (b). In the course of deposition, fractal aggregates with dimensions 0.7–1.1 μm (Fig. 1a) form macroscopic cloud-like formations with a size of 1–3 mm (Fig. 1b).

Carbon deposits were previously studied by other researchers [3, 4], but the samples did not possess a fractal structure. This is explained by the fact that the dc arc current density was within 169–372 A/cm^2, while our deposits were synthesized at $j = 1000$–1200 A/cm^2. It is this high current density, at which the arc temperature reaches 10^4 K, which ensures the formation of a carbon deposit with the fractal structure. The fractal particles form by the mechanism of cluster–cluster aggregation from small clusters (a few nanometers in size) nucleated within 10^{-4} s in the interelectrode carbon plasma [5].

For calculating the fractal dimension of the carbon structures studied, we used a model of the fractal aggregate composed of graphite clusters with radius r_0 and density ρ_0. For an aggregate radius of $R_0 \gg r_0$, the number of clusters entering into this formation is

$$N(r) = (R/r_0)^D, \quad (1)$$

where D is the fractal dimension. Formula (1) yields an expression for determining the density ρ of a substance (i.e., of the deposit) in a spherical particle of radius R:

$$\rho = \rho_0(r_0/R)^{3-D}. \quad (2)$$

For the carbon deposits studied, $\rho = 1.32$ g/cm^3, $\rho_0 = 2.23$ g/cm^3, $R = 4.5 \times 10^{-5}$ cm, $r_0 = 4 \times 10^{-7}$ cm, and $D = 2.89$. These results indicate that the carbon deposits represent compact volume fractals with the dimension approaching three.

1063-7850/03/2908-0627$24.00 © 2003 MAIK "Nauka/Interperiodica"

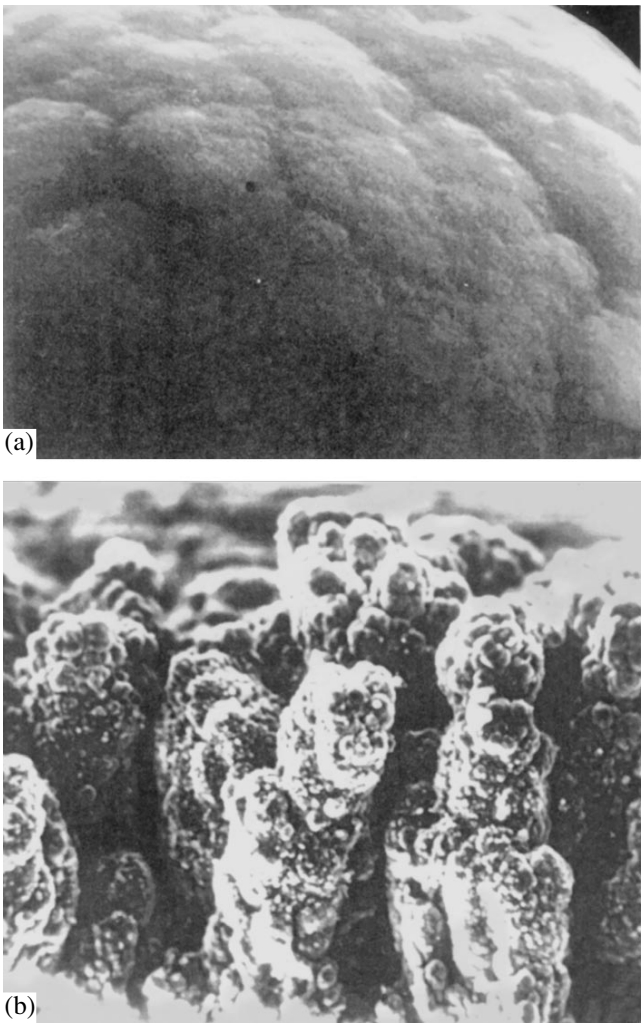

Fig. 1. SEM images of a carbon deposit with a magnification of (a) ×8700 and (b) ×310.

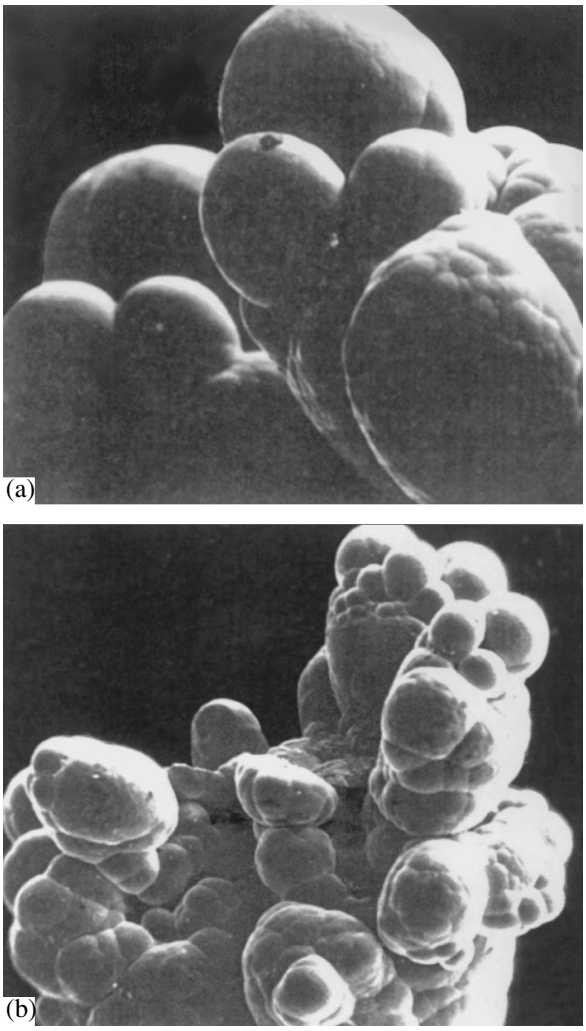

Fig. 2. SEM images of chromium fractals structures with a magnification of (a) ×220 and (b) ×77.

Figures 2a and 2b show the SEM micrographs of a chromium deposit with a magnification of ×220 (a) and ×77 (b). Figure 2a reveals the fractal aggregates with dimensions of 1.2–2 μm, which combine to form cloudlike formations with a size of up to 7–10 μm (Fig. 2b). For the chromium deposits studied, ρ = 6.2 g/cm^3, ρ_0 = 7.1 g/cm^3 (crystalline chromium), $R = 8 \times 10^{-5}$ cm, $r_0 = 4.5 \times 10^{-6}$ cm, and D = 2.95.

Thus, volume fractal structures composed of fractal aggregates and cloudlike formations can form from absolutely different materials in the course of various processes. The process of fractal formation requires a flow of substance. The fractal branches grow at the edges and on various macroscopic defects of a substrate. In our case, the fractals were formed under the conditions of a concentration gradient and the interaction between substance and electric field. The electric field strength is higher on various macroscopic structural defects of the growing fractal. This results in a higher deposition rate on the defects and edges of the fractal branches, which determines the branching and growth of the fractal structure.

Acknowledgments. The authors are grateful to V.P. Ievlev for his help in conducting measurements on the scanning electron microscope.

REFERENCES

1. E. F. Mikhailov and S. S. Vlasenko, Usp. Fiz. Nauk **165**, 263 (1995) [Phys. Usp. **38**, 253 (1995)].
2. B. B. Mandelbrot, *The Fractal Geometry of Nature* (Freeman, New York, 1983).
3. A. Yoshinori, Fullerene Sci. Technol. **2**, 173 (1994).
4. Yu. S. Grushko, V. M. Egorov, and I. N. Zimkin, Fiz. Tverd. Tela (St. Petersburg) **37**, 1838 (1995) [Phys. Solid State **37**, 1001 (1995)].
5. P. Meakin, Phys. Rev. Lett. **51**, 1119 (1983).

Translated by P. Pozdeev

Technical Physics Letters, Vol. 29, No. 8, 2003, pp. 629–631. Translated from Pis'ma v Zhurnal Tekhnicheskoĭ Fiziki, Vol. 29, No. 15, 2003, pp. 29–34.

Partial Synchronization in Inhomogeneous Autooscillatory Media

A. A. Akopov*, T. E. Vadivasova, V. V. Astakhov, and D. D. Matyushkin

Saratov State University, Saratov, Russia

** e-mail: artem@chaos.ssu.runnet.ru*

Received March 11, 2003

Abstract—Investigation of the phenomenon of partial synchronization in a continuous medium with natural frequency detuning depending on a spatial coordinate revealed frequency synchronization cluster formation previously known only in discrete models of distributed systems. The frequency cluster formation and the evolution of the cluster structures depending on the system parameters have been studied. © *2003 MAIK "Nauka/Interperiodica".*

In the chains and lattices of autooscillators, dependence of the natural frequency on the spatial coordinate leads (in the presence of a sufficiently strong coupling) to the formation of frequency synchronization clusters existing in a broad range of parameters and stable to the action of noise [1–4]. However, the effect of such partial (cluster) synchronization was never considered in inhomogeneous continuous media.

The aim of this work was to study the frequency synchronization clusters using the model of an autooscillatory medium with a continuous spatial coordinate. The model is described by a one-dimensional nonlinear equation in partial derivatives,

$$a_t = i\omega(x)a + r(1 - |a|^2)a + ga_{xx}, \quad (1)$$

where $i = \sqrt{-1}$, $a(x, t)$ is the complex oscillation amplitude depending on the time t and the spatial coordinate x, a_t is the first derivative with respect to time, and a_{xx} is the second derivative with respect to the spatial coordinate; the nonlinearity parameter r and the diffusion coefficient g are assumed to be real quantities independent of x; the function $\omega(x)$ characterizes detuning of the natural frequency as a function of the spatial coordinate. In particular, we will consider a linear frequency variation along the x axis, $\omega(x) = \frac{x\Delta_{\max}}{l}$, where l is the system length.

Equation (1) is a particular case of the Ginzburg–Landau equation, which is one of the main relationships in the theory of nonlinear nonequilibrium media. The chain of quasiharmonic autooscillators with differing natural frequencies studied in [1, 4] is an exact discrete analog of the medium described by Eq. (1). The chain equations lead to Eq. (1) upon the limiting transition to a continuous spatial coordinate.

We have studied a distributed system of finite length l obeying the boundary conditions of the second kind

$$a_x(x, t)\big|_{x = 0;\, l} \equiv 0. \quad (2)$$

The initial state of the medium was randomly selected in the vicinity of some homogeneous state. Equation (1) was numerically integrated according to an implicit scheme using the method of forward and reverse trials. The results of numerical integration were used to calculate the dependence of the average oscillation frequency on the spatial coordinate x:

$$\Omega(x) = \langle \phi_t(x, t) \rangle = \lim_{T \to \infty} \frac{\phi(x, t_0 + T) - \phi(x, t_0)}{T}. \quad (3)$$

Here, $\varphi(x, t)$ is the oscillations phase determined as

$$\phi(x, t) = \arg a(x, t) = \arctan\left(\frac{\mathrm{Im}\, a(x, t)}{\mathrm{Re}\, a(x, t)}\right) \pm \pi k, \quad k = 0, 1, 2, \ldots. \quad (4)$$

The quantity $\pm\pi k$ is added so as to ensure the continuity of the phase variation with time. The control parameters in this analysis were the system length l and the diffusion coefficient g. The critical parameter of nonlinearity was fixed at $r = 0.5$. The natural frequency detuning between boundary points of the medium was also constant and equal to $\Delta_{\max} = 0.2$.

The results of numerical experiments showed that distributed inhomogeneous system (1) exhibits, in a broad range of the parameters l and g, the formation of the frequency synchronization clusters, which is similar to the effect observed in a chain of autooscillators [1]. Depending on the control parameters, both ideal

1063-7850/03/2908-0629$24.00 © 2003 MAIK "Nauka/Interperiodica"

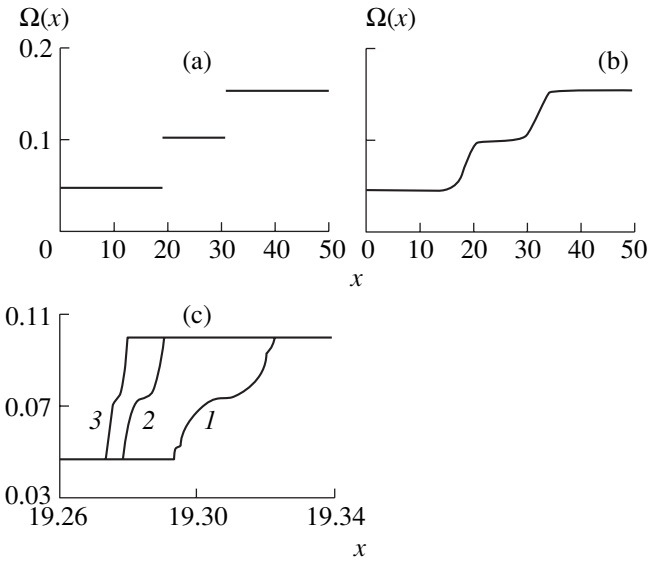

Fig. 1. Diagrams showing variation of the average oscillation frequency Ω along the coordinate x in a model medium with $\Delta_{max} = 0.2$, $l = 50$, and various values of the diffusion coefficient: (a) $g = 1.0$, ideal clusters (discretization steps $\Delta x = 0.05$, $\Delta t = 0.01$); (b) $g = 0.85$, nonideal clusters ($\Delta x = 0.05$, $\Delta t = 0.01$); (c) $g = 1.0$, the fragment of diagram (a) calculated for $\Delta x = 0.0005$ and various time steps $\Delta t = 0.05$ (*1*), 0.02 (*2*), 0.01 (*3*). All simulations performed over time $T = 30000$ for the set time $t_0 = 120000$.

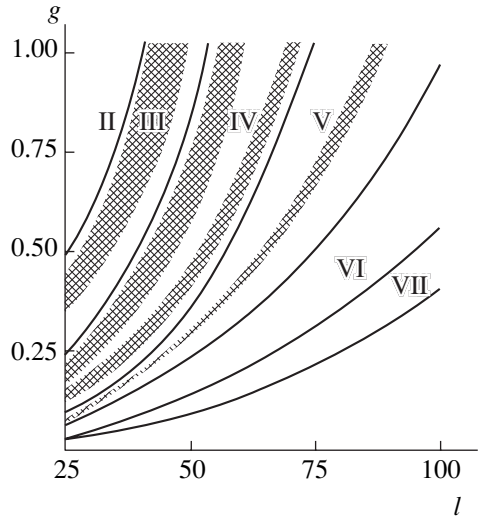

Fig. 2. A diagram of the synchronization cluster regimes in a continuous medium modeled by Eq. (1) on the plane of parameters g and l at a fixed frequency detuning $\Delta_{max} = 0.2$. Solid curves show the boundaries of regimes with various numbers (indicated by Rome numerals) of frequency clusters. Shaded areas indicate the broadest regions featuring ideal cluster structures.

(Fig. 1a) and nonideal (Fig. 1b) cluster structures can form in the system studied.

As is known for the discrete model medium [1], the frequencies of all autooscillators in the ideal cluster regime are strictly distributed between clusters. The boundaries between adjacent clusters correspond to a sharp change in the oscillation frequency Ω. The question naturally arises as to whether analogous frequency jumps can be observed in a continuous medium or the boundaries between ideal clusters will correspond to a continuous variation of $\Omega(x)$ (probably with a very large slope).

Investigation of the small-scale variations on the cluster boundaries requires more exact integration with small discretization intervals. Figure 1c shows the fragments of $\Omega(x)$ determined in the regime of ideal clusters (with $g = 1$) for equal steps Δx (one hundred times smaller than the case depicted in Fig. 1a) and different time steps Δt. For a rough discretization step in time, there are points not belonging to clusters and there appears a transition region corresponding to a continuous variation of the frequency $\Omega(x)$. As the integration step in time is decreased, the width of the transition region between clusters decreases as well. We may suggest that, for any arbitrarily small step Δx, the intercluster region will disappear in the limit $\Delta t \longrightarrow \infty$. This implies that $\Omega(x)$ in the continuous medium exhibits jumps at the boundaries of ideal clusters and possesses the same character as that established for a finite-length chain of autooscillators.

The form of the cluster structure in the system under consideration depends on the diffusion coefficient g and the detuning gradient $\delta = \Delta_{max}/l$. We have used numerical experiments to study evolution of the cluster structures in the course of variation of g and l values at a fixed detuning $\Delta_{max} = 0.2$. Figure 2 shows the regions of existence of the regimes with various numbers of clusters on the plane of parameters. The regions featuring eight or more clusters are rather narrow, and the boundaries between these regions are not depicted. The clusters in the indicated regions can be both ideal and nonideal (or intermediate). The broadest regions featuring ideal clusters are indicated by shadowing. As can be seen from Fig. 2, the structures with small numbers of clusters in systems with the diffusion coefficient g belonging to the indicated interval and the fixed detuning Δ_{max} can exist only for a limited length l. Note that the frequency detuning gradient δ decreases with increasing length l, which might seem to favor the synchronization effect. However, this is not observed, and the number of frequency clusters increases with the system length.

The boundaries between regions with different numbers of clusters, determined from numerical experiments, can be approximated by parabolas $g \sim \Delta_{max} l^2$. The same law describes the boundaries of the global synchronization region (i.e., of the region where all elements of the medium are synchronized at the same frequency). This region is not depicted in Fig. 2 because (for the Δ_{max} and l values considered) it corresponds to very large diffusion coefficients g. The analytical condition of the global synchronization, $g \geq \Delta_{max} l^2/12\pi$, agrees with the aforementioned general relationship

and coincides (to within the accuracy of calculations) with the numerical results. According to [1], the boundary of the global synchronization region in a discrete model with a fixed detuning Δ_{max} corresponds to $g \sim \Delta_{max}N$, where N is the length of the chain of autooscillators. Thus, the boundary of the global synchronization region differently depends on the system length in the case of a continuous medium and its discrete analogue.

The results of our numerical investigation of a continuous inhomogeneous autooscillatory medium with natural frequency detuning along a spatial coordinate show that the system exhibits the formation of frequency synchronization clusters. The cluster structures formed in a continuous medium are analogous to those observed in chains of autooscillators and can be both ideal and nonideal. Moreover, both chains and the continuous medium can feature jumplike changes in the average oscillation frequency Ω at the boundaries of ideal clusters. A numerical analysis of the system behavior in response to variation of the control parameters showed that bifurcation values of the diffusion coefficient corresponding to rearrangements of the cluster structures are proportional to the squared system length. The estimate of the boundary of the global synchronization region of the continuous system studied differs from the results obtained for a discrete chain of autooscillators.

Acknowledgments. The authors are grateful to I.A. Khovanov and A.V. Shabunin for valuable advice during the discussion of results.

This study was supported in part by the US Civilian Research and Development Foundation for the Independent States of the Former Soviet Union (CRDF) and by the Ministry of Education of the Russian Federation (Joint Award No. REC-006).

REFERENCES

1. G. V. Osipov and M. M. Sushchik, Phys. Rev. E **58**, 7198 (1998).
2. G. B. Ermentrout and N. Kopell, SIAM (Soc. Ind. Appl. Math.) J. Math. Anal. **15**, 215 (1984).
3. G. V. Osipov, A. S. Pikovsky, M. G. Rosenblum, and J. Kurths, Phys. Rev. E **55**, 2353 (1997).
4. T. E. Vadivasova, G. I. Strelkova, and V. S. Anishchenko, Phys. Rev. E **63**, 036225 (2001).

Translated by P. Pozdeev

Technical Physics Letters, Vol. 29, No. 8, 2003, pp. 632–633. Translated from Pis'ma v Zhurnal Tekhnicheskoĭ Fiziki, Vol. 29, No. 15, 2003, pp. 35–39.

A Decrease in the Mobility and Multiplication of Twinning Dislocations in Bismuth Crystals Exposed to Constant Magnetic Field

S. D. Shavrei and A. I. Pinchook*

Mozyr State Pedagogical University, Mozyr, Gomel oblast, Belarus

** e-mail: APinchook@yandex.ru*

Received February 11, 2003

Abstract—Simultaneous application of a constant magnetic field and a concentrated load partly suppresses twinning in bismuth crystals by decreasing the mobility and multiplication of twinning dislocations. This significantly decreases both the total twinned volume and the total area of the twin–matrix boundaries. © *2003 MAIK "Nauka/Interperiodica".*

In the last decade, extensive research has been devoted to the magnetoplastic effect (MPE) in solids. Despite considerable progress in the physics of this phenomenon, the effect of a magnetic field upon twinning, which is one of the most important types of plastic deformation in crystals, still remains practically unstudied. Recently [1, 2], we reported for the first time that the simultaneous action of a constant magnetic field and a concentrated load leads to a partial suppression of twinning in bismuth crystals. This is manifested by a drop in the mean length of wedge-shaped twins on the (111) cleavage plane of bismuth and a significant decrease in the total twinned volume and the total area of the twin–matrix boundaries.

Since the twinning and sliding are competitive forms of plastic deformation, we suggested that the magnetic field increases the intensity of sliding at the expense of suppressed twinning. In a crystal exposed to magnetic field, the evolution of a spin state in the perfect dislocation–paramagnetic center system leads to removal of the spin prohibitions and, hence, to breakage of the stopper. As a result, the magnetic field significantly increases the size of the dislocation rosette in bismuth crystals (under otherwise equal conditions). Apparently, the twinning dislocations are subject to the plasticizing effect of the magnetic field to a lower extent. This assumption is confirmed by the fact that the Burgers vector of partly twinning dislocations in bismuth crystals is as small as $a/12$, where a is the crystal lattice parameter [3]. For this reason, the cores of twinning dislocations contain smaller numbers of paramagnetic centers as compared to those of perfect dislocations.

This study was aimed at elucidating the main factors responsible for the partial suppression of twinning in the crystals exposed to a constant magnetic field. For this purpose, we have studied the growth of wedge-shaped twins in bismuth crystals under the action of a concentrated load with and without applied magnetic field.

The single crystals of bismuth were grown by the Bridgman technique using a high-purity initial material (99.97%, with lead impurity). The surface suited for investigation without special preparation was obtained by cleavage of the single crystal ingot along the (111) plane. Microindentation was performed on a special experimental setup representing an attachment to a commercial microhardness meter of the PMT-3 type (with all parts made of nonmagnetic materials). Wedge-shaped twins of the $\{110\}\langle 001\rangle$ system were produced by pressing with a standard diamond indenter on the (111) cleavage plane of the bismuth crystal sample. The sample was placed at the center of the gap of an electric magnet, where the magnetic induction was constant at $B = 0.2$ T.

The growth of wedge-shaped twins was induced by increasing the load P on the indenter rod for the same indentation time (both with and without magnetic field). The P value was varied from 0.09 to 0.29 N. In our experiments, the MPE in bismuth crystals was manifested during simultaneous action of the concentrated load and magnetic field. Upon unloading and switching off the magnetic field, we measured the wedge-shaped twin length L and mouth width h and counted the number of wedge-shaped twins n near the indenter marks. The values of L, h, and n were averaged over the results of measurements of the wedge-shaped twins formed around not less than 20 impressions. The relative experimental error did not exceed 3%.

The mean free pathlength λ of twinning dislocations was calculated by the formula $\lambda = \sum L_i/2n$. The number of twinning dislocations N localized at the twin–

1063-7850/03/2908-0632$24.00 © 2003 MAIK "Nauka/Interperiodica"

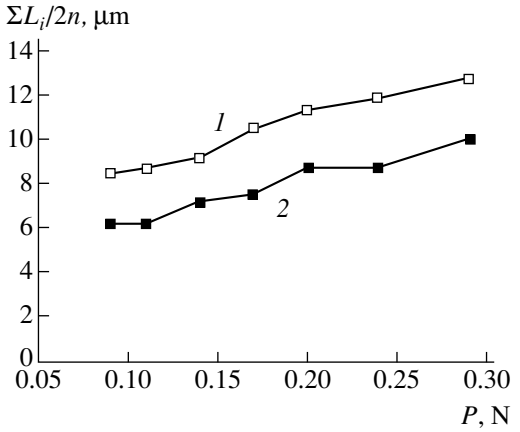

Fig. 1. Plots of the mean free pathlength λ of twinning dislocations versus indenter load P for a bismuth crystal indented (*1*) without and (*2*) with the applied constant magnetic field (B = 0.2 T).

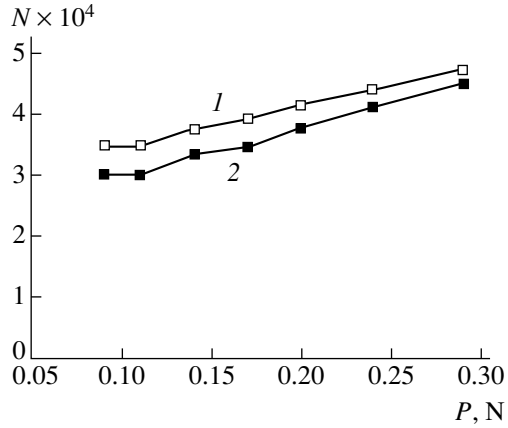

Fig. 2. Plots of the average number of twinning dislocations N localized at the twin–matrix boundary versus indenter load P for a bismuth crystal indented (*1*) without and (*2*) with the applied constant magnetic field (B = 0.2 T).

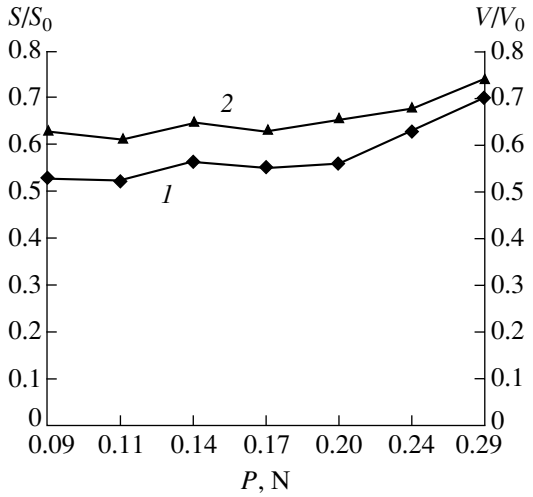

Fig. 3. Plots of the (*1*) S/S_0 and (*2*) V/V_0 ratio versus indenter load P.

matrix boundary was determined as $N = h/a$, where a is the crystal lattice parameter in the crystal direction perpendicular to the twinning plane [4].

As can be seen from the data presented in Fig. 1, an increase in the indenter load P leads to increase in the mean free pathlength λ of twinning dislocations in the sample both with and without the applied magnetic field. However, the value of λ in the presence of the field is significantly lower than that observed upon switching the field off. The observed decrease in the wedge-shaped twin lengths is explained by a partial magnetic-field-induced suppression of translation of the twinning dislocations along the twin–matrix boundaries.

Figure 2 shows plots of the average number of twinning dislocations N localized in the twinning plane versus indenter load P. As can be seen, N increases with the load. A comparison of curves *1* and *2* in Fig. 2 shows that the application of a constant magnetic field partly suppresses multiplication of the twinning dislocations.

Plastic deformation in the course of twinning can be quantitatively described in terms of the total twinned volume V and the total area S of the twin–matrix boundary [5]. As is known, the growth of wedge-shaped twins involves the nucleation of twinning dislocations at the twin opening and their translation along the twin–matrix boundary. Application of the magnetic field leads to partial suppression of the mobility and multiplication of the twinning dislocations, which results in a significant decrease in the total twinned volume V and the total area S.

Figure 3 shows the plots of V/V_0 and S/S_0 versus indenter load P, where V, S are the values measured on the samples exposed to magnetic field and V_0, S_0 are the values obtained with the field switched off. As can be seen, application of the magnetic field decreases the intensity of twinning at small loads almost by half. As the load is increased, the V/V_0 and S/S_0 ratios grow as well. This behavior suggests that the MPE probably has a surface character. However, final elucidation of the factors responsible for this phenomenon requires additional investigations.

REFERENCES

1. A. I. Pinchuk and S. D. Shavrei, Metallofiz. Noveishie Tekhnol. **22** (12), 43 (2000).
2. A. I. Pinchuk and S. D. Shavrei, Fiz. Tverd. Tela (St. Petersburg) **43**, 39 (2001) [Phys. Solid State **43**, 39 (2001)].
3. F. F. Lavrent'ev, Fiz. Met. Metalloved. **18**, 428 (1964).
4. A. M. Kosevich and V. S. Boiko, Usp. Fiz. Nauk **104**, 201 (1971) [Sov. Phys. Usp. **14**, 286 (1971)].
5. A. I. Pinchuk, Metallofiz. Noveishie Tekhnol. **22** (3), 88 (2000).

Translated by P. Pozdeev

Technical Physics Letters, Vol. 29, No. 8, 2003, pp. 634–635. Translated from Pis'ma v Zhurnal Tekhnicheskoĭ Fiziki, Vol. 29, No. 15, 2003, pp. 40–44.

The Effect of Ultrasonic Treatment on the Internal Friction in Silicon

A. P. Onanko, A. A. Podolyan, and I. V. Ostrovskii

Kiev National University, Kiev, Ukraine

e-mail: gogi@mail.univ.kiev.ua

Received February 18, 2003

Abstract—The temperature dependence of the internal friction in dislocation-free single crystal silicon after preliminary ultrasonic treatment exhibits a dominating peak at $T \approx 510$ K. This effect, reported for the first time, can be explained by the ultrasound-induced rearrangement of point defects related to interstitial silicon atoms.

Silicon is a semiconductor material most widely used in modern microelectronics. The increasing degree of integration in microchips make the problems of defect material structure more and more important. In the last decade, ultrasonic treatment has proved to be a promising method for controlling the defect structure of semiconductors [1–3]. However, the effects of ultrasonic treatment were studied predominantly in polycrystalline silicon [1, 2]. Recently [3], we demonstrated the possibility of ultrasound-stimulated impurity redistribution in single crystal silicon.

In this study, we have observed for the first time the appearance of a stable dominating peak in the temperature dependence of internal friction in dislocation-free single crystal silicon after preliminary ultrasonic treatment. This effect can be explained by the ultrasound-induced rearrangement of the complexes of point defects related to interstitial silicon atoms.

The measurements of internal friction offer a structure-sensitive method that reveals point defects due to related distortions developed in the crystal lattice. It was shown [4] that the temperature dependence of the internal friction in silicon samples measured after exposure to X-rays exhibit dominating peaks caused by the relaxation of point defects and their complexes.

We measured the internal friction and determined the resonance frequency by the method of composite piezoelectric oscillator operating at ~117 kHz with an alternating-sign deformation of amplitude $\varepsilon \approx 10^{-6}$ in a vacuum of $\sim 10^{-3}$ Pa [4].

The experiments were performed with Czochralski grown dislocation-free [111]-oriented *n*-type Si single crystals with a resistivity of $\rho \approx 500\ \Omega$ cm and a donor impurity concentration of $P \sim 10^{13}$ cm^{-3}. The crystal structure perfection was checked by the selective etching technique. Prior to the treatments, the sample surface was polished. After an ultrasonic treatment for ~4.5 h at a frequency of 500–1000 kHz (with an alternating-sign deformation of amplitude $\varepsilon \approx 10^{-5}$), a 500-μm-thick damaged surface layer was removed by etching in a standard etchant.

Here, it is expedient to point out some peculiarities related to the method of internal friction. The shape of the temperature dependence of the internal friction can be distorted by the annealing of structural defects, since the rate of this process varies with the temperature. The degree of this distortion depends on the relaxation parameters τ_0, $\tau_0 \exp(H/k_BT)$, and H, as well as on the degree of annealing of the structural defects and the rate of temperature variation $\partial T/\partial t$.

Figure 1 shows the temperature dependence of the internal friction for a silicon sample after preliminary ultrasonic treatment. Curves *1* and *2* show a narrow stable dominating peak at $T_{M3} \approx 510$ K. No such a peak (with comparable signal to background ratio) was

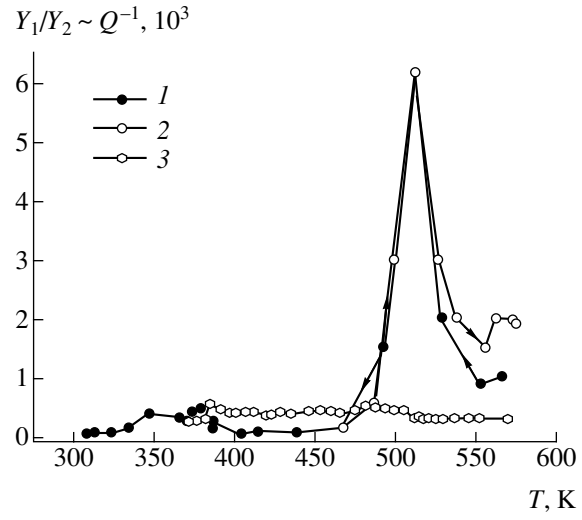

Fig. 1. The temperature dependences of the internal friction for a silicon sample after preliminary ultrasonic treatment: (*1*) cooling; (*2*) repeated heating; (*3*) initial crystal.

1063-7850/03/2908-0634$24.00 © 2003 MAIK "Nauka/Interperiodica"

observed for the initial sample (curve *3*). The character of curve *2* did not change upon repeated heating and the peak height remained the same. Some broadening of the smaller peaks at $T_{M1} \approx 346$ K and $T_{M2} \approx 380$ K probably reflects relaxation of the additional point defects of a new type appearing as a result of the ultrasonic treatment.

Figure 2 shows the temperature dependence of the elastic modulus of a silicon sample repeatedly measured in the same temperature interval. As can be seen, the second heating shows a ~0.1% increase in the absolute value of E, which is proportional to the squared resonance frequency f^2 (see Fig. 2, curve *2*). This change, falling outside the experimental uncertainty, is evidence of the strengthening of a silicon single crystal and the stabilization of structural defects.

Note a general property in common for all the relaxation peaks of internal friction. The temperature dependence of the elastic modulus exhibits a monotonic decrease (to within the experimental error of ~0.01%) when the temperature increases to a value corresponding to the internal friction peak, after which the slope $(\partial E/\partial T)$ of the curve significantly increases (Fig. 2).

The activation energy H of the relaxation process responsible for the internal friction peak was determined according to the Wert–Marx method with neglect of the entropy term [5],

$$H = k_B T_M \ln\left(\frac{k_B T_M}{\hbar \omega_M}\right),$$

where $T_M \approx 510$ is the temperature of the relaxation maximum, $f_M = 116870$ Hz is the resonance frequency of the sample, k_B is the Boltzmann constant, and $\hbar$ is the Planck constant. After substituting these values, we obtain $H = 0.8 \pm 0.1$ eV.

The activation energy was also determined by an independent method using the slope of the reconstructed plot of $\ln(Q^{-1} - Q_0^{-1})$ versus $1/T$ with subtracted background Q_0^{-1} of the internal friction peak. This method yields $H = 0.6 \pm 0.2$ eV.

Then we estimated the relaxation time constant τ using the condition that the relaxation peak due to the internal friction is observed for $\omega_M \tau = 2\pi f_M \tau_0 \exp(H/k_B T) = 1$. Upon substituting the activation energy $H \approx 0.8$ eV, we obtain $\tau_0 \approx 1.6 \times 10^{-12}$ s and the frequency factor $f_0 = \tau_0^{-1} \approx 6.3 \times 10^{11}$ Hz.

Note that the experimentally observed independence of the internal friction of the probing signal amplitude indicates that the observed resonance is not caused by a dislocation mechanism [5]. A necessary condition for observation of the internal friction peaks related to the point defects is the absence of sinks such as dislocations and stacking faults.

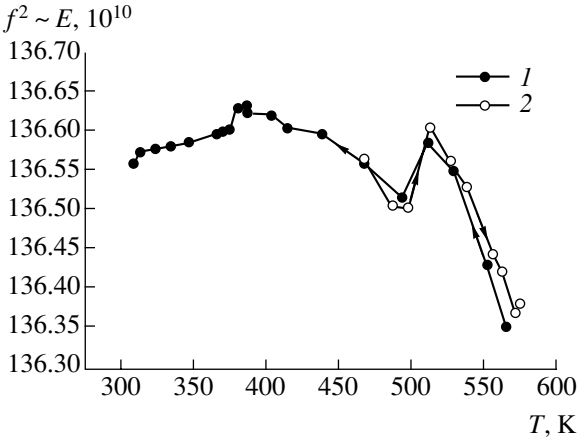

Fig. 2. The temperature dependence of the elastic modulus of a silicon sample after preliminary ultrasonic treatment: (*1*) cooling; (*2*) repeated heating.

The proximity of the activation energy of the relaxation process at $T_{M3} \approx 510$ K to the energy of migration ($H_0 = 0.85$ eV [6]) for the positively charged interstitial silicon ions Si_i^+ suggests a relaxation mechanism related to rearrangement of the interstitial neutral silicon atoms in the dumbbell configurations.

Thus, we have observed for the first time a dominating stable peak on the temperature dependence of the internal friction in Czochralski grown dislocation-free single crystal silicon. The appearance of this peak can be related to rearrangement of the complexes of point defects as a result of the ultrasonic treatment.

The results of calculations of the dynamic characteristics of interstitial silicon atoms Si_i and vacancy complexes can be used in optimization of the annealing regimes for the obtaining of silicon with controlled composition of structural defects.

REFERENCES

1. S. S. Ostapenko, L. Jastrzebski, J. Lagowski, and B. Sopori, Appl. Phys. Lett. **65**, 1555 (1994).
2. Y. Koshka, S. Ostapenko, T. Ruf, and J.-M. Zhang, Appl. Phys. Lett. **69**, 2537 (1996).
3. I. V. Ostrovskii, A. B. Nadtochii, and A. A. Podolyan, Fiz. Tekh. Poluprovodn. (St. Petersburg) **36**, 389 (2002) [Semiconductors **36**, 367 (2002)].
4. N. P. Kulish, P. A. Maksimyuk, N. A. Mel'nikova, *et al.*, Fiz. Tverd. Tela (St. Petersburg) **40**, 1257 (1998) [Phys. Solid State **40**, 1145 (1998)].
5. S. P. Nikanorov and B. K. Kardashev, *Elasticity and Dislocation Inelasticity of Crystals* (Nauka, Moscow, 1985).
6. L. S. Smirnov, *Physical Processes in Irradiated Semiconductors* (Nauka, Novosibirsk, 1977).

Translated by P. Pozdeev

Technical Physics Letters, Vol. 29, No. 8, 2003, pp. 636–637. Translated from Pis'ma v Zhurnal Tekhnicheskoĭ Fiziki, Vol. 29, No. 15, 2003, pp. 45–48.

Controlled Orientation of Fibers in a Glow Discharge Plasma

S. V. Bulychev, A. E. Dubinov, Yu. B. Kudasov, I. L. L'vov, K. E. Mikheev, S. A. Sadovoĭ, S. K. Saĭkov, and V. D. Selemir

Institute of Experimental Physics, Russian Federal Nuclear Center, Sarov, Russia

Received February 25, 2003

Abstract—We have experimentally studied the behavior of nylon fibers in a low-pressure glow discharge. The orientation of fibers deposited onto a substrate can be controlled by changing the direction of the transverse plasma density gradient. These experimental results can serve as a basis for the development of novel commercial technologies. © *2003 MAIK "Nauka/Interperiodica".*

The technology of synthetic flocked materials most frequently employs methods based on the electric charging of fibers in atmospheric-pressure corona discharge, followed by deposition of the charged fibers at a preset angle onto a sticky substrate in an external electric field [1, 2].

Recent experiments on the orientation of fibers in a plasma [3] showed that an alternative flocking technology can be developed using a low-pressure glow discharge. It was established that nylon fibers with a diameter of 7.5 and 15 μm and a length of 300 μm are readily oriented perpendicularly to the discharge axis at a pressure of 0.1 Torr. It should be noted that use of the glow discharge in the technology of flocked materials has good prospects, because this method significantly increases the production yield (due to the increase in the area processed at once) and markedly improves the flocked material quality (due to homogeneity of the discharge).

At the same time, the dimensions of fibers used in experiment [3] are significantly smaller than those encountered in commercial flocking technology. For this reason, our study was aimed at the experimental verification of the possibility of using glow discharge for the orientation of greater fibers and the development of methods for extracting the oriented fibers from the discharge region and for controlling the fiber orientation relative to the substrate plane.

The experiments were conducted in a specially developed chamber, schematically depicted in Fig. 1. The device comprises a dielectric tube of square cross section (10×10 cm) and a length of 70 cm. Square steel electrodes with dimensions fit to the chamber cross section are mounted on the tube edges. In our experiments, the tube was oriented horizontally. The upper wall of the chamber bears a high-precision needle injector of fibers, capable of injecting both single particles and bunches (of up to several thousand fibers) into the plasma. This injector, previously employed in the investigation of dusty plasmas, is described in detail elsewhere [4].

The sticky substrate was a transparent (one-sided) adhesive tape (Rusi Star Company) placed with the adhesive layer facing upward on a sample holder table arranged in the bottom part of the chamber under the fiber injector (Fig. 1). The substrate area was 10×10 cm. The fibers were prepared by cutting nylon threads with a diameter of 100 μm into 3-mm-long pieces. These particles were about 1000 times heavier than the fibers studied in [3]. In our experiments, the fibers were injected into the plasma one by one.

Fibers injected into a nonionized gas in the absence of discharge (at atmospheric pressure or in a vacuum of ~0.1 Torr) exhibit no orientation and drop onto a substrate with all their length in plane, making a random angle with the chamber axis.

When a homogeneous stationary glow discharge is generated in the chamber (Fig. 1a) at a discharge current of 250 mA, the fibers are incident strictly along a

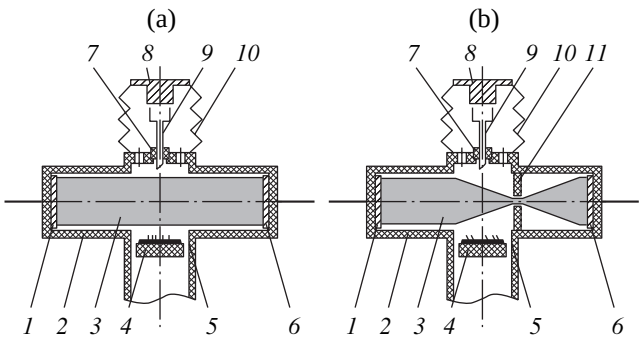

Fig. 1. A schematic diagram of the experimental setup operating in the (a) straight and (b) diaphragmed glow discharge regime: (*1*) anode; (*2*) chamber tube; (*3*) glow discharge plasma; (*4*) sample holder table; (*5*) pumping outlet; (*6*) cathode; (*7*) rubber plug; (*8*) plunger; (*9*) needle; (*10*) bellows; (*11*) diaphragm.

1063-7850/03/2908-0636$24.00 © 2003 MAIK "Nauka/Interperiodica"

vertical line, being oriented perpendicularly to the discharge as reported in [3]. Reaching the substrate, the fiber sticks with its end to the adhesive and stays in the vertical position for an arbitrarily long period of time. Figure 2a shows a magnified photograph of such a fiber fixed on the substrate.

The effect of fiber orientation across the discharge is readily explainable if we compare the longitudinal and transverse components of the electric field in the discharge chamber. As is known, the longitudinal component is small (amounting to 10–20 V/cm [5]), while the transverse component (related to the plasma density gradient at the dielectric walls) may reach up to several hundred volts per square centimeter.

This suggests a simple method for controlling the orientation of fibers incident onto the substrate: the fiber tilt can be controlled by changing the plasma density gradient at the substrate surface by means of a transverse diaphragm shown in Fig. 1b. We used a dielectric diaphragm with a round hole. By varying the hole diameter and the distance from the diaphragm to the plane of fiber injection, it is possible to control the angle of the plasma density gradient relative to the substrate surface. For a hole diameter of 40 mm and a distance of 80 mm from the diaphragm to the injection plane, the maximum angle between the plasma density gradient and the vertical is about 70°. In such a field, the injected fibers are incident inclined onto the substrate, stick with the end to the adhesive, and stay tilted at the same angle of about 70°, as illustrated in Fig. 2b.

Thus, we have experimentally demonstrated the possibility of applying fiber onto an adhesive substrate in a low-pressure glow discharge for the production of flocked materials with a controlled fiber tilt angle.

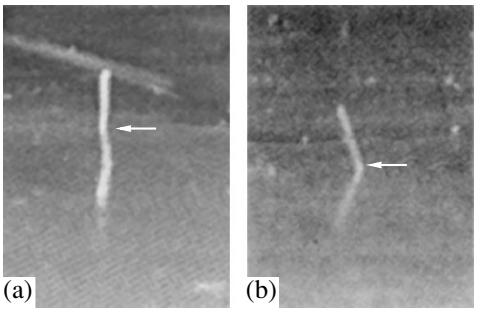

Fig. 2. Photographs of fibers stuck to a substrate in the (a) straight and (b) diaphragmed glow discharge regime.

These results can serve as the basis for the development of novel commercial technologies.

Acknowledgments. This study was supported by a research grant from NWO, no. 047-008-013.

REFERENCES

1. V. I. Popkov and M. I. Glazov, *Charge Kinetics and Dynamics of Fibers in Electric Field* (Nauka, Moscow, 1976).
2. E. N. Bershev, *Electrical Flocking (Flock Deposition in Electrical Fields)* (Legkaya Industriya, Moscow, 1977).
3. V. I. Molotkov, A. P. Nefedov, M. Yu. Pustyl'nik, *et al.*, Pis'ma Zh. Éksp. Teor. Fiz. **71**, 152 (2000) [JETP Lett. **71**, 102 (2000)].
4. S. V. Bulychev, A. E. Dubinov, V. S. Zhdanov, *et al.*, Prikl. Mekh. Tekh. Fiz. **42** (6), 19 (2001).
5. Yu. P. Raizer, *Gas Discharge Physics* (Nauka, Moscow, 1992, 2nd ed.; Springer-Verlag, Berlin, 1991).

Translated by P. Pozdeev

Technical Physics Letters, Vol. 29, No. 8, 2003, pp. 638–640. Translated from Pis'ma v Zhurnal Tekhnicheskoĭ Fiziki, Vol. 29, No. 15, 2003, pp. 49–54.

Infralow-Frequency Oscillations in Photoconductivity of Chromium-Doped Silicon

Kh. Kh. Dzhuliev, A. Yu. Leiderman, and A. T. Mamadalimov

Physicotechnical Institute, "Solar Physics" Research and Production Corporation, Academy of Sciences of the Republic of Uzbekistan, Tashkent, Uzbekistan

e-mail: lutp@uzsci.net

Received February 18, 2003

Abstract—The photoconductivity of chromium-doped silicon at $T = 4.2$ K under constant illumination in the fundamental absorption band exhibits infralow-frequency oscillations at 10^{-2} Hz, the amplitude of which sharply increase with the illumination intensity. No such oscillations are observed in samples of *n*- Si⟨Cr⟩ or in chromium-free *p*-Si and *n*-Si control samples. A model qualitatively explaining the appearance of such oscillations is proposed, which is based on the fact that chromium in silicon can occur in two states, one being electrically (and recombination) active, and the other, inactive. *© 2003 MAIK "Nauka/Interperiodica".*

Deep impurity levels in silicon have been studied for many years (see, e.g., [1–3]). However, the behavior of chromium as an impurity in silicon is still insufficiently studied, and only a few publications devoted to this system are available [4, 5].

This study was aimed at establishing the laws of photoconductivity in chromium-doped silicon under the conditions of illumination in the fundamental absorption band.

The experiments were performed with samples cut from single crystal silicon wafers of the KDB grade with an initial resistivity of $\rho = 20\ \Omega$ cm and a shallow dopant (boron) concentration of $N_a \approx 7 \times 10^{14}$ cm^{-3}. After thorough mechanical and chemical polishing of the silicon surface (see [4]), the sample plates with dimensions $10 \times 6 \times 1$ mm were coated with metal chromium of special purity grade and placed into thoroughly cleaned quartz tubes with a diameter of 20 mm, dull at one end. The chromium doping was performed by heating the samples to 1200 ± 20°C for 4 h in a high-temperature convection furnace, followed by rapid quenching in a vacuum oil (VM-1). In order to eliminate the influence of surface structure defects, 100- to 150-μm-thick layers were removed from the sample surface [6, 7]. Finally, ohmic contacts were created on the opposite edges by fusing 97% In–3% Ga eutectic. Upon chromium diffusion, the sample resistivity was 100–200 Ω cm (for $N = 1.39 \times 10^{14}$–6.95×10^{13} cm^{-3}).

The photoconductivity of silicon samples was measured at 4.2 K using an IKS-21 spectrophotometer equipped with a special cryostat with leucosapphire windows. Figure 1 shows the photoconductivity spectrum of a *p*-Si⟨Cr⟩ samples in comparison to that of the chromium-free *p*-Si control. The chromium-doped samples not subjected to preliminary illumination exhibit virtually no impurity conductivity. The exposure to a light in the fundamental absorption band ($h\nu \geq E_g$) gives rise to a rather complicated conductivity spectrum (curve *1*) showing a nonmonotonic character. A comparison of these results to the photoconductivity of a control *p*-Si sample (curve *2*) suggests that the photoconductivity buildup at $h\nu = 0.23$ and 0.4 eV is probably related to the defects produced by thermal treatment, while the peak at $h\nu = 0.31$ eV is directly related to the chromium impurity level [4]. The presence of Cr atoms in *p*-Si was confirmed by the EPR

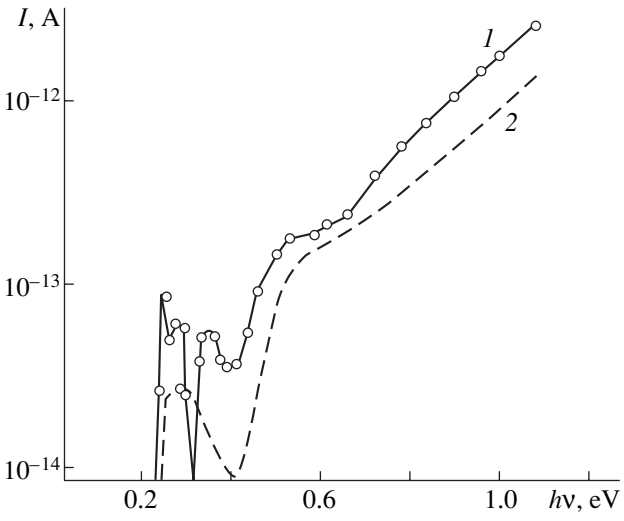

Fig. 1. The photoconductivity spectra of (*1*) *p*-Si⟨Cr⟩ and (*2*) initial *p*-Si measured at $T = 4.2$ K, $V = 6$ V ($I_1 \sim p_{s1}$, $I_2 \sim p_{s2}$).

1063-7850/03/2908-0638$24.00 © 2003 MAIK "Nauka/Interperiodica"

spectra of doped samples, which were fully identical to those reported in [8].

The samples of p-Si⟨Cr⟩ measured at $T = 4.2$ K and a constant illumination in the fundamental absorption band exhibited infralow spontaneous current oscillations at a frequency of $\approx 10^{-2}$ Hz. The amplitude of these oscillations increased with the illumination intensity (Fig. 2). No such oscillations were observed in n-Si⟨Cr⟩ or in chromium-free n-Si and p-Si control samples.

As is known, chromium in silicon behaves as a donor and can occur in two states, one being electrically active, and the other, inactive. The latter state is typical of chromium atoms accumulated at various defects. The concentration of electrically active chromium significantly exceeds that of thermally activated donors [4, 5]. At liquid helium temperatures, shallow dopants occur in a frozen state but are readily ionized under illumination in the fundamental absorption band to give the main contribution to the photoconductivity. In addition, these impurities can interact with the electrically active chromium atoms to form acceptor–donor pairs playing the role of recombination centers [1, 8].

In the region of very low temperatures under study, other important processes are the formation and annihilation of excitons, predominantly those localized on impurities and possessing a lifetime on the order of 10^{-8}–10^{-9} s [9]. Each annihilation event is accompanied by energy evolution, and these portions of energy almost continuously act upon the silicon crystal lattice (which was already weakened by the introduction of chromium). It would be natural to suggest that, under the action of both photoexcitation and the exciton processes, chromium atoms can somewhat change their spatial positions and energies, thus becoming electrically active for a certain time.

The kinetics of changes in the nonequilibrium hole density p (and in the photoconductivity) is described by the usual equation

$$dp/dt = G - U, \tag{1}$$

where G and U are the rates of the hole production and recombination, respectively. Under usual assumptions, $U = p/\tau$ and $\tau = 1/c_p N_{R0}$, Eq. (1) leads to the well-known expression for a steady-state density of free holes: $p_{s1} \equiv \tau G = c_p N_{R0} G$ (τ is the hole lifetime, c_p is the coefficient of hole trapping on the recombination centers, and N_{R0} is the concentration of these centers).

Now let us allow a part of the electrically inactive defects to become activated (N_{ad}) in the course of excitation. Then, the number of effectively operating recombination centers N_R will increase to $N_R = N_{R0} + N_{ad}$. The free hole lifetime changes accordingly and the terms in Eq. (1) appear as $\tau = 1/[c_p(N_{R0} + N_{ad})]$ and $U = (N_{R0} + N_{ad})c_p(p_{s1} + \langle p \rangle)$, where $\langle p \rangle$ is a change in the hole density upon reaching the first steady-state level p_{s1}.

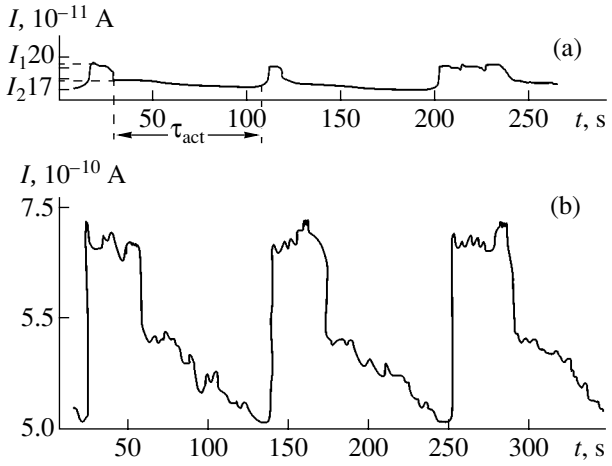

Fig. 2. Infralow-frequency oscillations observed in the photoconductivity of p-Si⟨Cr⟩ measured at $T = 4.2$ K, $V = 10$ V for the samples illuminated at $h\nu \geq E_g$ with $\Phi = 50$ lx (a) and 500 lx (b).

The second steady-state hole density level determined by standard methods is

$$p_{s2} = p_{s1}\{1 - N_{ad}/(N_{ad} + N_{R0})[1 - \exp(-\tau_{act}/\tau)]\}, \tag{2}$$

where τ_{act} is the period of time during which the electrically inactive chromium atoms occur in the active state (Fig. 2).

There is quite a simple qualitative physical explanation of the observed oscillations. Under the action of both photoexcitation and the exciton processes, a part of the electrically inactive chromium atoms pass to the active state, the number of effectively operating recombination centers increases, and the recombination rate U grows. This leads to a decrease in the free hole density and to the establishment of another, metastable steady state with p_{s2}, in which the system occurs during a time period of τ_{act}. Subsequently, these atoms turn back into the electrically inactive state, the number of effectively operating recombination centers decreases, and the recombination rate U drops. This makes it principally possible that the system would convert into an autooscillatory medium [10] with the internal source of oscillations represented by chromium atoms capable of passing from inactive to active state and back. The proposed model is consistent with the fact that the observed oscillations increase in amplitude with the illumination intensity. Indeed, this leads to a growth in the intensity of the formation of excitons localized on deep centers and, hence, to a more intense conversion of chromium atoms from inactive to active.

Acknowledgments. This study was supported by the Foundation for Basic Research of the Academy of Sciences of the Republic of Uzbekistan.

REFERENCES

1. A. G. Milnes, *Deep Impurities in Semiconductors* (Wiley, New York, 1973; Mir, Moscow, 1977).
2. K. V. Ravi, *Imperfections and Impurities in Semiconducting Silicon* (Wiley, New York, 1981; Mir, Moscow, 1984).
3. A. T. Mamadalimov, A. A. Lebedev, and E. V. Astrova, *Spectroscopy of Deep Centers in Semiconductors* (Tashkent. Gos. Univ., Tashkent, 1999).
4. R. A. Muminov, Kh. Kh. Dzhuliev, Sh. Makhkamov, and A. T. Mamadalimov, Fiz. Tekh. Poluprovodn. (Leningrad) **16**, 582 (1980) [Sov. Phys. Semicond. **16**, 376 (1980)].
5. R. A. Muminov, Kh. Kh. Dzhuliev, Kh. Igamberdiev, and A. T. Mamadalimov, Izv. Akad. Nauk SSSR, Neorg. Mater., No. 6, 1040 (1985).
6. V. I. Fistul', *Physics and Chemistry of Semiconductors* (Metallurgiya, Moscow, 1995).
7. A. A. Lebedev, A. T. Mamadalimov, and P. K. Khabibullaev, in *Collection of Scientific Works* (Tashkent. Gos. Univ., Tashkent, 1981), pp. 59–69.
8. H. H. Woodbury and G. W. Ludwig, Phys. Rev. **117**, 102 (1960).
9. G. Kh. Gurgineshvili and E. I. Rashba, Fiz. Tverd. Tela (Leningrad) **4**, 1229 (1962) [Sov. Phys. Solid State **4**, 759 (1962)].
10. P. M. Karageorgy-Alkalaev and A. Yu. Leiderman, Phys. Status Solidi A **100**, 221 (1987).

Translated by P. Pozdeev

Technical Physics Letters, Vol. 29, No. 8, 2003, pp. 641–642. Translated from Pis'ma v Zhurnal Tekhnicheskoĭ Fiziki, Vol. 29, No. 15, 2003, pp. 55–60.

Thin-Film Nickel Coatings on Fiber Materials

L. M. Lyn'kov, V. A. Bogush, E. A. Senkovets, and S. M. Zavadskii

Belarussian State University of Informatics and Radioelectronics, Minsk, Belarus

e-mail: aleks@gw.bsuir.unibel.by

Received December 2, 2002

Abstract—Vacuum deposition of thin films onto fiber materials is a promising method of obtaining electromagnetic screens. We have studied the structure and the electromagnetic properties of machine-knitted fabric coated with nickel by means of magnetron sputtering. When the fabric is irradiated from the metal-coated side, the reflection coefficient is higher by a factor of 1.4 as compared to the case when the same source of electromagnetic radiation is situated on the opposite side (facing the uncoated surface), while the absorption coefficient in both cases is the same. © *2003 MAIK "Nauka/Interperiodica".*

Electromagnetic radiation is widely used in all fields of human activity, but elevated levels of the electromagnetic field intensity negatively affect various biological objects, including the human organism, complicate the functioning of low-power high-precision measuring equipment, and pose problems related to electromagnetic compatibility and protection of the equipment and information.

In connection with this, an important problem is the development of effective and readily applicable screening and absorbing materials and coatings. Of special interest is the creation of elastic materials capable of absorbing radio waves, based on the use of commercial equipment for the production of fabrics, ensuring low cost and reduced consumption of raw materials [1]. A promising method of obtaining electromagnetic screens is offered by vacuum deposition of thin metal films onto fiber materials.

Sample preparation. Using ion-beam and ion-stimulated magnetron sputter technologies, it is possible to obtain films of various materials, which are characterized by high adhesion to various substrates at relatively low thermal loads [2]. For studying the screening properties of such metal coatings, we prepared samples of machine-knitted fabric bearing on one side a metal (nickel) coating deposited by magnetron sputtering.

The metal films were deposited in a vacuum system of the VUP-2M type equipped with double-beam ion sources. Prior to deposition, the working chamber was evacuated to a residual pressure of 2×10^{-3} Pa and the substrate (knitted fabric) was cleaned by ion bombardment. The metal film was deposited by sputtering a nickel target with an ion beam from a source operating at a discharge voltage of $U_d = 5$ kV, a current of $I_d = 200$ mA, and a working gas pressure of $P = 2 \times 10^{-2}$ Pa. The substrate was a knitted fabric made on a loop-knit high-pile machine ensuring the formation of a material possessing a flocky volume structure.

The thickness of a metal deposit was determined by measuring the sputter process duration and using a calibration curve of the nickel film thickness on a glass substrate versus deposition time. The nickel film had a surface resistance of 32 Ω/□. In our experiments, the fabric base (polyacrylonitrile, PAN) was coated on one side with a 0.1-μm-thick nickel film. The deposit possessed good adhesion to the substrate, showed stable electrical properties, and exhibited no degradation with time.

Experimental methods. The structure of the synthesized material was studied by X-ray diffraction. The measurements performed on a DRON-30 diffractometer using CuK_α radiation (λ = 1.5417737 Å) provided data on the general phase composition and the average size of crystalline particles. The diffraction pattern was recorded in intensity (I) versus angle (2θ) coordinates at a rate of 2000 cps in a range of angles from 10° to 80°. The data were processed so as to determine the relative intensity of the diffraction lines (in terms of area under the peak) expressed as a percentage of the maximum line intensity.

The noise on the diffractograms and the increase in the intensity of X-ray scattering at small diffraction angles is explained by the influence of the organic fiber component [3]. The metal phases were identified by comparing the observed diffraction patterns with the ASTM data file. The nickel-coated samples were studied from both the front (metal-bearing) and the rear (metal-free) sides.

The screening properties of the metal-coated material were studied using a set of the vector chain analyzer equipment capable of measuring the S-characteristics of four-terminal circuits in the microwave range (1.5–18 and 18–37 GHz intervals) [4]. Prior to measurements, the equipment was calibrated so that the amplitude–frequency characteristic of the signal transmission path was considered as the zero level, the sample characteristics being measured relative to this level.

1063-7850/03/2908-0641$24.00 © 2003 MAIK "Nauka/Interperiodica"

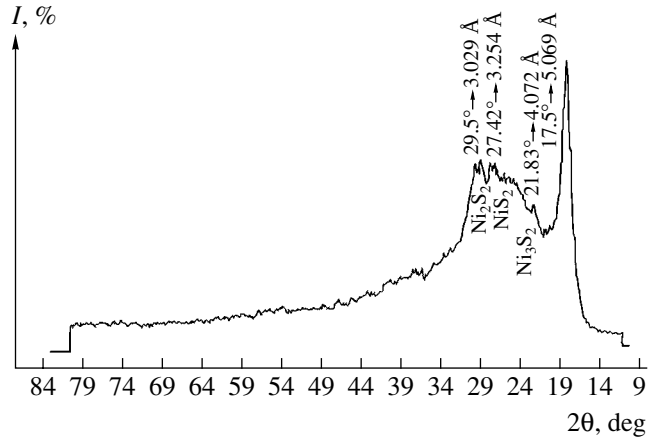

Fig. 1. X-ray diffractogram of a nickel-coated PAN fabric measured from the metal-free side of a sample.

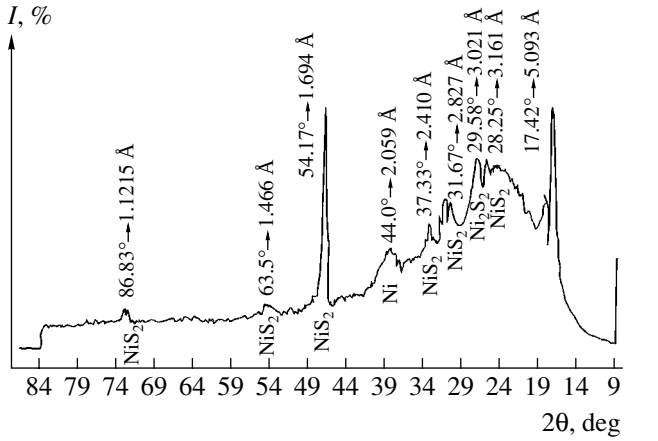

Fig. 2. X-ray diffractogram of a nickel-coated PAN fabric measured from the metal-bearing side of a sample.

Each sample, representing a square (15 × 15 cm) piece of fabric, was placed between radiator and receiver (representing horn systems or waveguide flanges). The measured quantities were the reflection (S_{11}) and transmission (S_{21}) coefficients. The sample was uniformly stretched (so as to avoid distortions in the knitted structure) and oriented perpendicularly to the wave propagation direction. The measurements were performed with the radiation source facing either the front or the rear side of the samples.

Results and discussion. The screening properties of knitted fabrics with a metal film deposited on the front side were characterized by the transmission (S_{21}) and reflection (S_{11}) coefficients measured from both sides in the frequency range 1.5–37.7 GHz. It was established that the reflection coefficient is somewhat greater (–8… –10 dB) at lower frequencies and decreases at higher frequencies (–4… –6 dB), while the transmission coefficient varies in the opposite manner (increasing from –2 to –10 dB).

The reflection coefficient is smaller when the electromagnetic radiation is incident from the uncoated side of the fabric. The metal screen reflects on the average 1.4 times more energy than the uncoated side of the sample. At the same time, the transmission coefficient of the uncoated side is not higher than that of the metal-coated side. This result indicates that the electromagnetic wave incident on the uncoated side is attenuated as a result of absorption to a greater extent than the same wave incident onto the metal-coated side.

We have also studied the screening characteristics of corrugated pseudopyramidal structures made of a flat metal-coated material, with a corrugation height of 5, 7, and 12 mm. The measurements were performed at a fixed frequency of 9.5 GHz. Both the transmission and the reflection coefficients grow by 2–3 dB, the screening properties increasing with the corrugation height.

It was found that the X-ray diffraction pattern of the synthesized material measured from the uncoated side of the fabric contains, besides the peak due to the substrate (modified PAN with an interplanar spacing of 5.069 Å), reflections corresponding to NiS_2, Ni_2S_2, and Ni_3S_2 phases (Fig. 1). The diffractograms obtained from the metal-coated side contains an additional reflection indicative of the presence of a cubic modification of metal nickel in the deposit (Fig. 2).

In our opinion, it is the presence of crystalline nickel on the metal-coated side that accounts for an increase in the reflection coefficient of this surface. The PAN–nickel interface is geometrically more inhomogeneous, which accounts for the increased absorption of the incident radiation.

The results of our investigation show that knitted fabrics with sputter-deposited nickel coatings exhibit different absorption properties with respect to microwave radiation, depending on the working conditions. The proposed fabrics were used as the external layers in multilayer screening materials, which allowed us to obtain elastic multilayer screens with SWR ~ 1.5 at an attenuation coefficient of 20–23 dB in the frequency range from 1.5 to 115 GHz. The established features of the interaction of elastic structures with electromagnetic radiation should be taken into account in the development of highly effective wideband absorbing coatings.

REFERENCES

1. L. M. Lyn'kov, V. A. Bogush, V. P. Glybin, *et al.*, in *Flexible Structures of Electromagnetic Radiation Screens*, Ed. by L. M. Lyn'kov (Belarus. Gos. Univ. Inform. Radioélectron., Minsk, 2000).
2. V. A. Bogush, S. M. Zavadskii, L. M. Lyn'kov, *et al.*, Izv. Belarus. Inzh. Akad., No. 1(7)/2, 171 (1999).
3. S. S. Golerik, L. N. Rastorguev, and Yu. A. Skakov, *X-Ray and Electron-Optical Analysis* (Metallurgiya, Moscow, 1970).
4. A. S. Elizarov, A. M. Kostrikin, A. V. Gusinskii, *et al.*, Radiotekh. Élektron. (Moscow) **41**, 602 (1996).

Translated by P. Pozdeev

Technical Physics Letters, Vol. 29, No. 8, 2003, pp. 643–645. Translated from Pis'ma v Zhurnal Tekhnicheskoĭ Fiziki, Vol. 29, No. 15, 2003, pp. 61–66.

Circular Vortex Formation in a Pulsed Jet Penetrating Through a Filter Layer

V. P. Samsonov

Surgut State University, Surgut, Russia

e-mail: svp@iff.surgu.ru

Received February 27, 2003

Abstract—A method for the formation of a laminar circular vortex is proposed that excludes the interaction of a pulsed jet with the nozzle edge. Another method is suggested for visualization of the gas flow and measurement of the gas velocity distribution in a jet penetrating through a filter layer. Critical conditions for the formation of a circular vortex are established, determining the jet power as a function of the thickness of a flat filter layer formed by granulated silica gel. It is shown that a mechanism of the laminar circular vortex formation is controlled only by the gas flow acceleration in the jet. *© 2003 MAIK "Nauka/Interperiodica".*

Elucidation of the physical mechanisms responsible for the formation of circular vortices in pulsed flows is an important problem from the standpoint of both basic science and technical applications [1, 2]. According to the Prandtl hypothesis, a circular vortex is formed as a result of the interaction between the flow and the edge of a nozzle through which the pulsed gas jet is pushed out. However, Petrov [3] has argued against this concept and suggested an alternative mechanism based on the jet front drag and expansion. In either case, the process has to obey the first Raily criterion concerning the bending point in the velocity profile [4]. In order to check that the proposed mechanisms are not contradictory, it was necessary to perform experiments in which the role of edge effects was minimized. Such experimental conditions were provided [5, 6] by exposing a flat PMMA target surface to a pulsed laser radiation. In this system, no edges of confining surfaces are present. However, the change in the flow velocity at the boundary of the jet of pyrolysis products (thermal spot on the surface) was rather significant. The experiments [5, 6] revealed limiting values of the energy and time of the laser action determining the vortex ring formation.

Here, we describe a new method for the investigation of flows in a pulsed jet scattered from a flat filter obstacle. The proposed method also excludes the interaction of a jet with edges of confining surfaces, being similar in this respect to the approach used in [5, 6]. By changing the filter layer thickness, it is possible to decrease to zero the velocity gradient at the boundary between the jet and ambient air, because the scattering modifies the velocity profile from parabolic at the entrance to Gaussian at the exit. In addition, the proposed method allows the flow acceleration on passage through the filter layer to be measured at a high precision.

Figure 1 shows a schematic diagram of the experimental setup, which comprises chamber *1* having the shape of a rectangular parallelepiped containing a horizontal layer of granulated silica gel or glass beads. The particle size was varied from 3×10^{-3} to 15×10^{-3} m, and the filter layer thickness, from 0.02 to 0.4 m. The square (0.5×0.5 m) chamber bottom and top bases are closed with a steel grid made of a 1-mm-thick wire. The side walls of the chamber (0.45 m high) are made of a transparent organic glass.

The flow velocity profile inside the filter layer is visualized using a special measuring insert cassette representing a thin rectangular parallelepiped with dimensions $0.5 \times 0.45 \times 0.02$ m. The 0.5×0.45 m cassette side walls are also made of a 1-mm-thick transparent organic glass. The cassette is placed at the center of the filter layer and filled with silica gel granules. The input

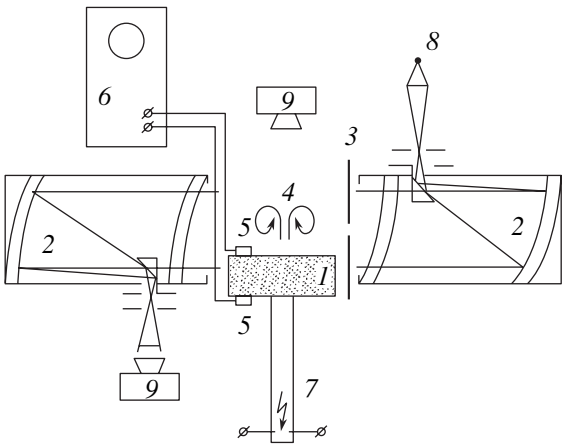

Fig. 1. A schematic diagram of the experimental setup: (*1*) chamber with a filter layer; (*2*) collimator of an IAB-451 shadow device; (*3*) slit diaphragm; (*4*) circular vortex; (*5*) piezoceramic pressure sensors; (*6*) doubly-beam oscillograph; (*7*) combustion tube (open at the upper end); (*8*) mercury lamp (DRSh-1); (*9*) video cameras.

1063-7850/03/2908-0643$24.00 © 2003 MAIK "Nauka/Interperiodica"

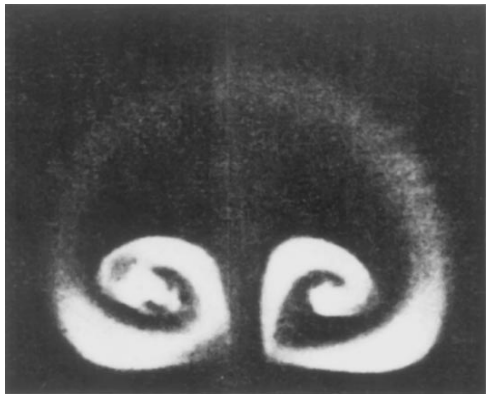

Fig. 2. A typical photograph of a circular vortex formed in a pulsed jet of combustion products after passage through a filter layer.

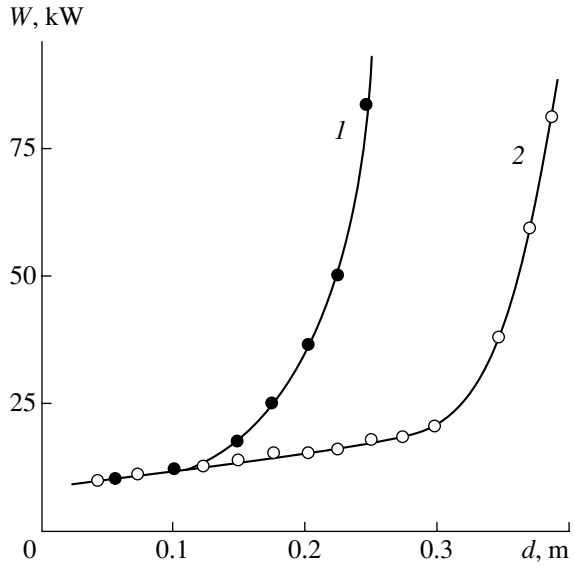

Fig. 3. Plots of the minimum pulsed jet exhaust power versus filter layer thickness showing the (*1*) upper and (*2*) lower boundaries of the region featuring the formation of a laminar circular vortex.

end cross section is closed with a grid, while the output end is open. In order to fix the positions of granules after the pulsed jet passage, the experiments are performed for a vertical position of the filter layer. Since the layer of granules in the cassette in this case is horizontal, the particle displacements are retained after the jet passage. There were two variants of filling the cassette. In the first variant, we used silica gel granules painted in different colors, and layers of differently colored granules were alternating. In the second variant, the parallel layers of granules were alternating with parallel layers of powdered magnesium oxide. The first variant was used to measure the velocity distribution for the jets possessing large momenta, while the second variant was used in the case of low gas velocities in the filter layer.

The transfer of magnesium oxide particles and the displacement of granules in the filter layer relative to the initial positions are determined by the energy (i.e., squared velocity) of the jet at each point. The shift of boundaries between the layers of differently colored granules or magnesium oxide particles after the jet passage can be observed through the transparent side walls of the cassette, thus visualizing the gas velocity profile in the jet. This allows us to measure the transverse jet dimensions and determine the velocity profile in the filter layer. Magnesium oxide particles carried away from the filter layer also visualize the gas flow in a circular vortex.

The gas flow in the jet at the upper end of the filter layer is visualized using the method of a light knife. The narrow light beam is created by collimator *2* of an IAB-451 shadow device and by diaphragm *3* having the shape of a flat vertical slit. Figure 1 shows the top view of the optical system and the side view of a circular vortex *4* and the filter layer. The time required for the pulsed jet front to travel through the filter layer is determined using two piezoceramic pressure sensors *5* situated on the bottom and top surfaces of the layer. The signals from pressure sensors are monitored by a double-beam oscillograph *6*.

The bottom surface of the filter layer is in contact with the open end of a cylindrical tube *7*, the other end of which is closed. The tube has an inner diameter of 0.05 m and a length of 1.00 m and is filled with a propane–air or propane–oxygen mixture. The gas mixture burns when ignited with a high-voltage electric spark. The power of the jet of exhaust products at the entrance of the filter layer can be controlled by the duration of the gas mixture burning, which depends on the ignition point coordinate along the tube axis. The exhaust time is determined by measuring the duration of the signal from a pressure sensor situated at the closed end of the tube. The amount of thermal energy liberated during combustion was calculated using the caloric value and the volume of a given gas mixture. The combustible mixtures were prepared in a gas displacement chamber, with an error of the gas volume fraction not exceeding 0.1%.

Figure 2 shows a typical photograph of a laminar circular vortex formed in the jet above the filter layer. The axis of the vortex ring coincides with the jet direction at the exit of the filter layer. The upper boundary of the circular vortex imaged on the photograph corresponds to the jet front. It was found that the vortex ring formation at the exit of the filter layer takes place at any thickness of this layer and depends only on the initial jet power (exhaust power). This is illustrated by the plot of a minimum jet power versus layer thickness (Fig. 3), determining the conditions of the vortex ring formation. Curves *1* and *2* in Fig. 3 correspond to the upper and lower boundaries of the region of a laminar circular vortex formation. Increase in the exhaust power above the upper boundary leads to turbulization of the jet,

whereas a decrease in this power below the threshold corresponding to curve *2* leads to the formation of a laminar stream or a jet decay inside the filter. An increase in the minimum jet energy at a constant filter layer thickness leads to a decrease in the time of jet passage through the layer. This result agrees with the data reported in [5]. In our experiments, this time varied from 0.01 to 1 s. The acceleration at the jet front was about 20 m/s^2 and remained approximately constant. This result is quite natural from the standpoint of kinematics, since the vortex motion is the only form of laminar accelerated motion of a continuous medium [4, 7].

REFERENCES

1. M. A. Lavrent'ev and B. V. Shabat, *Problems of Fluid Dynamics and Their Mathematical Models* (Nauka, Moscow, 1973).
2. V. V. Kozlov, G. R. Grek, L. L. Lefdal', and V. G. Chernoraĭ, Prikl. Mekh. Tekh. Fiz. **43** (2), 62 (2002).
3. P. A. Petrov, Izv. Akad. Nauk SSSR, Mekh. Zhidk. Gaza, No. 2, 19 (1973).
4. H. Schlichting, *Boundary Layer Theory* (McGraw-Hill, New York, 1968; Nauka, Moscow, 1974).
5. A. E. Averson, M. V. Alekseev, and V. P. Borisov, Prikl. Mekh. Tekh. Fiz., No. 5, 64 (1984).
6. M. V. Alekseev and I. G. Fateev, Fiz. Goreniya Vzryva **32** (5), 30 (1996).
7. L. D. Landau and E. M. Lifshitz, *Course of Theoretical Physics*, Vol. 6: *Fluid Mechanics* (Nauka, Moscow, 1988; Pergamon, New York, 1987).

Translated by P. Pozdeev

Technical Physics Letters, Vol. 29, No. 8, 2003, pp. 646–648. Translated from Pis'ma v Zhurnal Tekhnicheskoĭ Fiziki, Vol. 29, No. 15, 2003, pp. 67–72.

On the Causes of Low-Frequency Hysteresis and Current Dispersion in AlGaN/GaN HFETs

P. A. Ivanov and M. E. Levinshteĭn

Ioffe Physicotechnical Institute, Russian Academy of Sciences, St. Petersburg, 194021 Russia

Received February 6, 2003

Abstract—AlGaN/GaN based HFETs with two-dimensional electron gas exhibit a transition hysteresis and sink current dispersion in the regime of a large-amplitude ramp gate signal at a frequency of 10^{-2}–10^{-1} Hz. This instability is explained by the fact that a space charge region (expanding upon the transistor blocking) in the *n*-GaN layer is controlled by the floating potential of this layer (not coupled galvanically to the grounded source). As a result, the relaxation time of a charge induced in the space charge region is sufficiently large, and this discharge lags behind the gate potential variations. © *2003 MAIK "Nauka/Interperiodica".*

At present, AlGaN/GaN heterostructures are used for fabricating field effect transistors (HFETs) with a two-dimensional electron gas (2DEG), which are characterized by record output power in the microwave range [1]. The 2DEG conductivity in HFETs is higher than that in devices based on the AlGaAs/GaAs heterostructure. In particular, the maximum layer carrier density in the 2DEG of AlGaN/GaN HFETs is about 2×10^{13} cm^{-2} [2] and the room-temperature electron mobility reaches up to 2100 cm^2/(V s)[3].

However, there are still some problems to be solved for AlGaN/GaN HFETs, in particular, those related to a frequency dispersion of the sink current in a large-signal operation mode (see, e.g., [4–7]), whereby a decrease in the output current amplitude is observed in a very broad frequency range (from 10^{-3} Hz up to 10 GHz). The dispersion effects are usually related to recharge of the deep traps localized at the AlGaN/GaN interface, in the AlGaN barrier layer, or on the AlGaN surface [5–8]. As was noted in [5], the dispersion can lead, under certain conditions, to a total "collapse" of the current. Therefore, this effect cannot be related entirely to the deep traps.

Here, we discuss an alternative mechanism of instability in AlGaN/GaN HFETs, which is related to the floating potential of the substrate.

We have studied the epitaxial AlGaN/GaN structures grown by metalorganic chemical vapor deposition (MOCVD) technique on semi-insulating 4H-SiC substrates (see the inset in Fig. 1) [8]. The base structure comprises a 50-nm-thick AlN buffer layer, a 0.4-μm-thick *n*-GaN layer with a high resistivity, and a 10-nm-thick $Al_{0.2}Ga_{0.8}N$ barrier layer doped with silicon to 2×10^{18} cm^{-3}. Prior to the gate layer deposition, the structure was coated with a 10-nm-thick SiO_2 layer in order to reduce the gate leak currents. The gate was formed by depositing Pt/Au contacts. Ohmic contacts on the sink and source were formed by depositing a Ti/Al/Ti/Au scheme.

Figure 1 shows typical curves of the HFET channel conductivity versus control ramp voltage with an amplitude not exceeding the threshold value $V_T = -5.5$ V (the applied voltage changed from –10 V to zero and back at a frequency of 10^{-2} Hz (curve *1*) or 10^{-1} Hz (curve *2*). As can be seen, the transition characteristics measured in this way reveal a characteristic hysteresis. An increase in the control signal frequency leads to an increase in hysteresis width, on the one hand, and to a current dispersion (i.e., to a decrease in the magnitude of conductivity oscillations), on the other hand. The observed hysteresis in the transition characteristics is probably related to the fact that the gate potential vari-

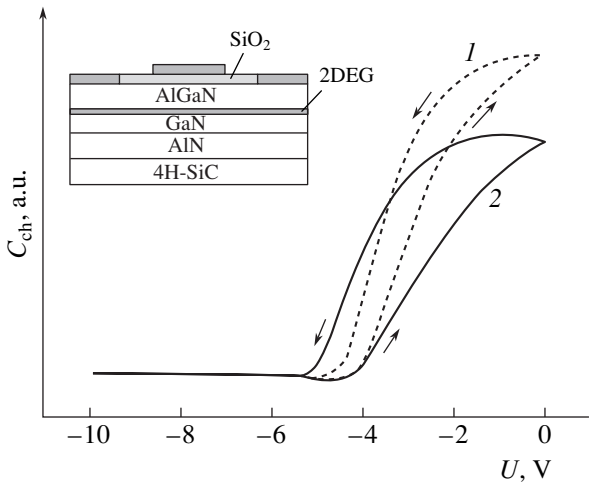

Fig. 1. Typical curves of the AlGaN/GaN HFET channel conductivity versus control ramp voltage varied from –10 V to zero and back at a frequency of (*1*) 10^{-2} Hz and (*2*) 10^{-1} Hz. The inset shows the HFET structure.

ations result in the accumulation of a certain charge in the structure, the relaxation time of which is comparable (in the order of magnitude) with the period of the gate potential variation.

From the shape of the hysteresis loop, it is possible to make certain indirect conclusions about the region of the HFET structure in which the aforementioned charge can be localized and about the probable relaxation mechanism. Indeed, let us assume that the charge is induced between the metal gate and the two-dimensional *n*-channel in the wide-bandgap AlGaN layer, for example, due to recharging of traps at the AlGaN/GaN interface or at the SiO_2/AlGaN interface. For a positively biased gate, the traps will charge negatively by capturing free electrons. If this charging cannot exactly follow the gate potential variations, it will lead to nonequilibrium depletion of the high-ohmic *n*-GaN layer, thus decreasing the conductivity of the two-dimensional *n*-channel as compared to the quasi-equilibrium level. For a negative bias of the gate, the traps will acquire a positive charge, thus increasing the conductivity of the two-dimensional *n*-channel against the quasi-equilibrium level.

Thus, on measuring the characteristic of the transition from open to blocked transistor state, the conductivity of the two-dimensional *n*-channel will be smaller than that during the reverse passage. Apparently, the opposite sign of the hysteresis must be observed if the charge is accumulated behind the two-dimensional *n*-channel (i.e., in the GaN layer). In this case, the conductivity of the two-dimensional *n*-channel will be greater on the transition from open to closed state than during the reverse passage. As can be seen from Fig. 2, the HFETs studied in our experiments feature the second situation, from which we conclude that the induced charge is localized behind the two-dimensional *n*-channel, in the high-ohmic *n*-GaN layer.

The mechanism responsible for the accumulation and relaxation of the induced charge in the *n*-GaN layer can be two-fold. When the transistor is blocked, the space charge region representing a positive charge of ionized donors in the *n*-GaN layer is expanded. Then, a slowly relaxing induced charge can be that appearing upon the recharge of deep traps (donors) in the GaN layer. However, in this case the concentration of such deep traps has to be comparable in the order of magnitude with the concentration of shallow donors.

We consider as more probable an alterative explanation. Note that, in the HFET structure under consideration, the substrate is not coupled galvanically to the grounded source, and, hence, the space charge region thickness in the *n*-GaN layer is determined by the floating potential of the substrate. In this case, a slowly relaxing induced charge will be that of shallow donors in the space charge region. Indeed, a charge equilibrium following the gate potential variations under conditions of the floating potential of the substrate can be established only due to generation–recombination processes. However, the corresponding room-temperature relaxation time in a wide-bandgap GaN can be very large, and the charge of the space charge region will follow changes in the control voltage with a certain delay.

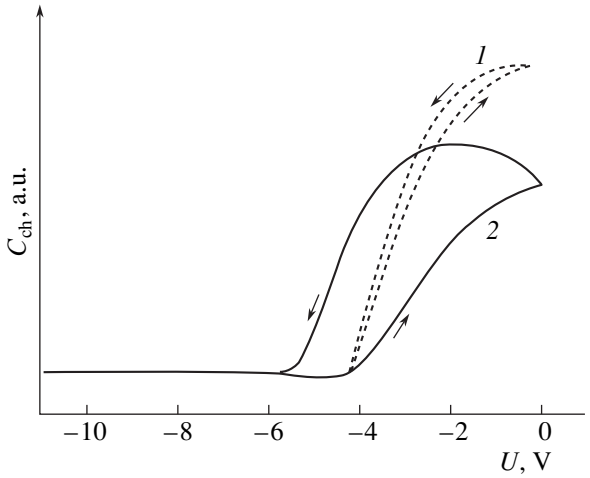

Fig. 2. Curves of the AlGaN/GaN HFET channel conductivity versus control ramp voltage varied from (*1*) –4 V to zero and back and (*2*) from –20 V to zero and back at a frequency of 10^{-2} Hz.

The proposed mechanism of the accumulation and relaxation of the induced charge is indirectly confirmed by the fact that the hysteresis observed in the transition characteristics was rather small when the magnitude of the control voltage variations did not exceed I_T (see Fig. 2, curve *1* recorded for V_{GS} = 4 V). This result is quite natural, since the gate potential variations do not influence the space charge region thickness and virtually all the induced charge is concentrated in the two-dimensional *n*-channel. In contrast, as the gate potential variations exceed 10 V, the hysteresis was additionally increased due to a large charge induced in the space charge region (Fig. 2, curve *2* recorded for V_{GS} = 20 V).

In the case of a large magnitude of the gate voltage variations, we observed an unusual phenomenon whereby the channel conductivity continues to increase for some time even after passage through the turning point (V_{GS} = 0) on the transition characteristic, despite the fact that the gate potential already changes toward blocking the transistor. This behavior of the channel conductivity can be explained only assuming that the floating opening potential of the substrate also keeps increasing at a rate exceeding that of the blocking gate potential.

To eliminate the instability described in this paper, it is necessary to provide for an electrical lead from the substrate or to shorten the substrate and source as in silicon inversion-channel MOS transistors [10].

Acknowledgments. This study was supported by the Russian Foundation for Basic Research, project no. 02-02-17619.

REFERENCES

1. G. Simin, X. Hu, N. Il'inskaya, *et al.*, Electron. Lett. **36**, 2043 (2000).
2. R. Gaska, J. Yang, A. Osinsky, *et al.*, in *Technical Digest of the IEEE International Electron Devices Meeting (IEDM-97), Washington, 1997*, p. 565.
3. R. Gaska, M. S. Shur, A. D. Bykhovski, *et al.*, Appl. Phys. Lett. **74**, 287 (1999).
4. M. Asif Khan, M. S. Shur, Q. Chen, *et al.*, Electron. Lett. **30**, 2175 (1994).
5. D. Daumiller, D. Theron, C. Caguiere, *et al.*, IEEE Electron Device Lett. **22**, 62 (2001).
6. R. Vetury, N. Q. Zhang, S. Keller, *et al.*, IEEE Trans. Electron Devices **48**, 560 (2001).
7. P. B. Klein, S. C. Binari, K. Ikossi-Anastasiou, *et al.*, Electron. Lett. **37**, 662 (2001).
8. A. Tarakji, G. Simin, N. Il'inskaya, *et al.*, Appl. Phys. Lett. **78**, 2169 (2001).
9. M. Asif Khan, X. Hu, G. Simin, *et al.*, Appl. Phys. Lett. **77**, 1339 (2000).
10. S. Sze, *Physics of Semiconductor Devices* (Wiley, New York, 1981; Mir, Moscow, 1984).

Translated by P. Pozdeev

Technical Physics Letters, Vol. 29, No. 8, 2003, pp. 649–651. Translated from Pis'ma v Zhurnal Tekhnicheskoĭ Fiziki, Vol. 29, No. 15, 2003, pp. 73–79.

Fine Structure of Carbon Films Deposited from a Microwave Low-Pressure Gas Discharge

A. A. Alekhin, S. Yu. Suzdal'tsev, and R. K. Yafarov

Saratov Branch, Institute of Radio Engineering and Electronics, Russian Academy of Sciences, Saratov, Russia

e-mail: pirpc@renet.ru

Received February 7, 2003

Abstract—We have studied the conditions of synthesis and the fine structure of carbon films of various structural modifications possessing preset electrical properties. The phase diagram of polymorphous transformations is constructed for carbon films grown from the plasma of microwave discharge in low-pressure ethanol vapor. Technological factors influencing the efficiency of extracting diamondlike microcrystals from a hydrocarbon matrix have been studied. Depending on the extraction regime and initial layer thickness, the size of extracted microcrystals can vary from 10–12 to 100–120 nm, while their surface concentration may reach 1.4×10^7 cm^{-2}.

The process of synthesis in low-pressure gas discharge plasma offers a promising technology of obtaining carbon materials necessary for the development of electronic devices capable of operating under extremal conditions [1]. This is related to the fact that, owing to its physicochemical nature, carbon can form materials with different types of chemical bonds, depending on the synthesis conditions. These materials are composed of carbon in various allotropic modifications, including graphite, diamond, fullerenes, carbin, etc. [2]. Diamond is the most attractive form of carbon for use in the cathodes of secondary electron emission devices. The advantages of diamond cathodes are their extremely high stability with respect to ion bombardment, high chemical resistance and thermal conductivity, and low electron work function for the crystal faces with certain crystallographic orientations [1, 3].

This study was aimed at determining the optimum technological conditions for the synthesis of carbon films of various allotropic modifications and for the obtaining of heterophase film structures with controlled content of diamondlike microcrystals for use as cold emission cathodes.

Carbon films were deposited onto glass substrates from the plasma of a microwave discharge in low-pressure ethanol vapor. We studied the influence of the substrate temperature and ethanol vapor pressure on the deposition rate, phase composition, electrical properties, and surface microtopography of carbon deposits. The microtopography of the surface of samples was studied with a scanning atomic force microscope (AFM).

Previously [4, 5], the X-ray diffraction investigation of carbon films showed that the formation of various allotropic modifications of carbon is determined to a considerable extent by the temperature of condensation and by the energies of ions and active particles in the working medium. At an accelerating potential of −300 V applied to the substrate holder, an increase in the condensation temperature is accompanied by the sequential formation of polymeric, diamond, and graphite films (Fig. 1).

The region of pressures below 0.05 Pa and temperatures above 300°C features the predominant formation of a graphite phase. Here, it should be noted that, for a

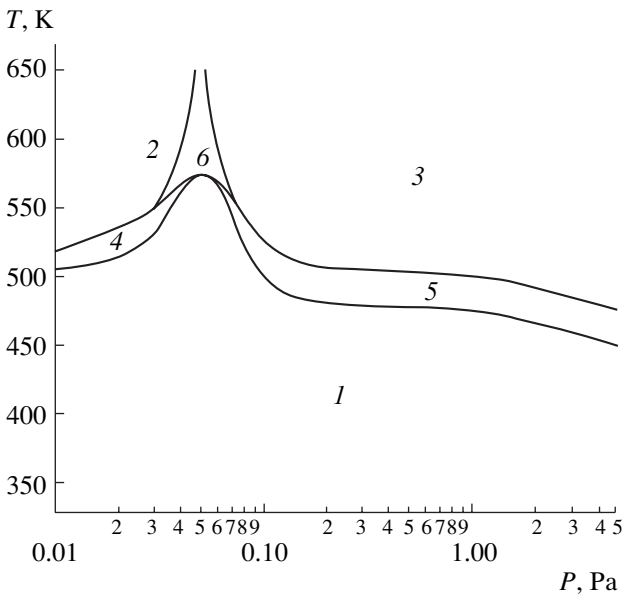

Fig. 1. The phase diagram of polymorphous transformations in carbon films deposited from the plasma of microwave discharge in low-pressure ethanol vapor: (*1*) hydrocarbon polymer; (*2*) graphite; (*3*) diamondlike phase; (*4*) polymer–graphite phase; (*5*) polymer–diamondlike phase; (*6*) graphite–diamondlike phase.

1063-7850/03/2908-0649$24.00 © 2003 MAIK "Nauka/Interperiodica"

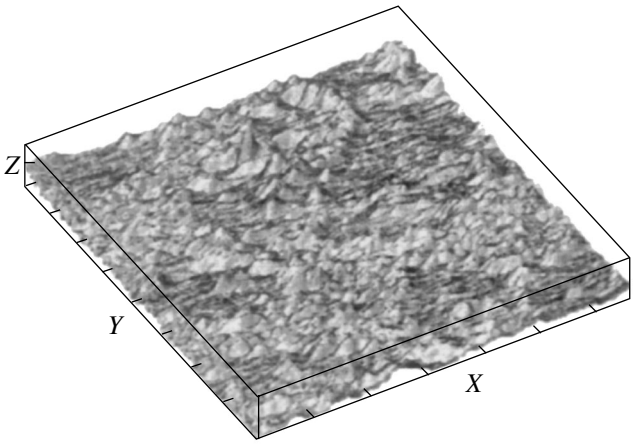

SCALE *X*: 1000 nm *Y*: 1000 nm *Z*: 10 nm

Fig. 2. Typical AFM image of the initial surface of a polymer matrix with dispersed diamondlike nanocrystals deposited at $T = 50°C$, $P = 1$ Pa, $U = -300$ V.

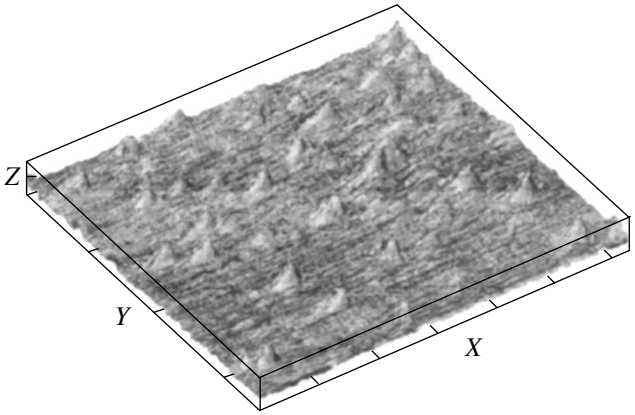

SCALE *X*: 1000 nm *Y*: 1000 nm *Z*: 100 nm

Fig. 3. Typical AFM image of the surface of a polymer matrix with dispersed diamondlike nanocrystals after thermal annealing in vacuum.

microwave plasma formed under the electron cyclotron resonance (ECR) conditions, these pressures are characterized by the maximum degree of plasma ionization (up to 5–7%). The minimum temperatures for which a graphite phase formation is observed are 50–70 K above those for the appearance of diamondlike phases. This is evidence that the energy requirements for the nucleation of a graphite phase are higher than for the diamondlike phase. The diamondlike films can be obtained at a temperature not lower than 250–300°C and an ethanol vapor pressure not lower than 0.08–0.1 Pa. Below 200°C, the deposits represent hydrocarbon polymer films.

One of the main factors determining the diagram of polymorphous transformations in carbon films, besides the degree of ionization, substrate temperature, and ion energy is the initial composition of a carbon-containing plasma. This is evidenced by the results of experiments on the deposition of carbon films from the plasma of discharge in acetylene. In this medium, no diagrams of the type depicted in Fig. 1 could be constructed in the entire range of the process parameters studied.

Investigation of the surface microtopography of hydrocarbon polymer films corresponding to region *5* in Fig. 1 by atomic force microscopy showed that these deposits usually represent a heterophase system comprising pyramidal microcrystals with a base diameter of 0.05–0.1 μm and a height of 0.02–0.15 μm dispersed in an amorphous matrix. The size and the surface concentration of microcrystals depend on the film deposition conditions. In particular, an increase in the substrate temperature was accompanied by a drop in the concentration of microcrystals and a growth in their dimensions [6].

We have performed a series of experiments on the extraction of diamondlike microcrystals from a hydrocarbon polymer matrix. This was achieved through removal of the hydrocarbon component by methods of thermal annealing in vacuum, sputtering in an argon plasma, and etching in a microwave ECR plasma in dry residual air. The extraction efficiency was evaluated by determining the thickness of the removed polymer layer and by analyzing the resulting structure with an AFM (P4-SPM-MDT). This analysis provided data on the dimensions and surface concentration of diamondlike microprotrusions in the remaining polymeric matrix.

Figures 2 and 3 show typical AFM images illustrating the microtopography of the hydrocarbon polymer films with the initial thicknesses of 1.2 and 0.4 μm upon thermal annealing for 1 h at 400°C in a residual vacuum of 5 Pa. After this treatment, the dimensions of microprotrusions increased from 10–12 to 100–150 nm and above. This growth was achieved at the expense of the film thickness decreasing to the same extent. The annealing also led to certain changes in the polymer film structure, as manifested by a decrease in the transparency and electric resistance of the sample.

The sputtering using argon ions with an energy of up to 300 eV did not provide for an acceptable etching rate of the diamond–polymer carbon films. This is evidence of the high resistance of these films with respect to physical sputtering. Nevertheless, the argon ion bombardment made the surface relief more pronounced.

The most effective extraction of diamondlike microcrystals was provided by vacuum-plasma treatment in a dry residual air atmosphere. In this case, the height of extracted microprotrusions was usually lower than the thickness of removed polymer matrix layer. For example, etching in the air plasma at a pressure of 0.05 Pa and an accelerating voltage of –300 V removed a 0.4-μm-thick layer, leaving microcrystals with an average size of 40 nm.

Figure 4 shows a plot of the height of extracted microcrystals versus removed hydrocarbon layer thickness for the films with initial thicknesses of 1.2 and 0.4 μm etched at an air pressure of $P = 0.05$ and 1 Pa and a substrate holder potential of +300 or –300 V. As can be seen, the maximum height of microcrystals extracted at $P = 0.05$ Pa from thin films reaches 120 nm and is 1.5 times greater than the maximum value for the initially thick films. As the pressure is increased to 1 Pa, the maximum height of the extracted microcrystals decreases and the polarity of the applied voltage becomes insignificant. As is known, this is related to a decrease in the degree of plasma ionization with increasing gas pressure. As a result, a change in the voltage polarity at $P = 1$ Pa has almost no influence on the type of charged particles involved in the etching process. Thus, a decrease in the ion component (i.e., in the amount of oxygen ions) involved in the plasma action upon the diamond–polymer layer leads to a decrease in the selectivity of etching of these phases and, hence, to a decrease in the dimensions of the extracted microcrystals. A difference between the dimensions of extracted microcrystals and the thickness of removed matrix layer indicates that microcrystals are randomly nucleated in the matrix in the course of deposition, grow until reaching certain dimensions, and remain buried in the matrix, rather than keep growing through the whole matrix layer.

The surface concentration of extracted microcrystals and a change in this value also depend on the regime of extraction and the initial layer thickness. In thin films, the maximum of this concentration is more pronounced and can reach up to 1.4×10^7 cm^{-2}, while in thick films the concentration of microcrystals only slightly varies with the removed layer thickness.

Thus, the results of our investigation revealed the main technological factors influencing the selectivity of etching of the diamondlike microcrystals–hydrocarbon polymer matrix system. The most effective method for the extraction of diamondlike microcrystals was provided by vacuum-plasma treatment in a dry residual air atmosphere, which ensures removal of the matrix material at a significant rate leaving diamondlike microcrystals of maximum size.

The dimensions of the diamondlike microcrystals are maximum in the near-surface layers and decrease in depth of the polymer film. The size (varying from 10–12 to 100–120 nm) and the surface concentration of microcrystals (reaching up to 1.4×10^7 cm^{-2}) that can be extracted depend on the plasma etching regime and the initial layer thickness.

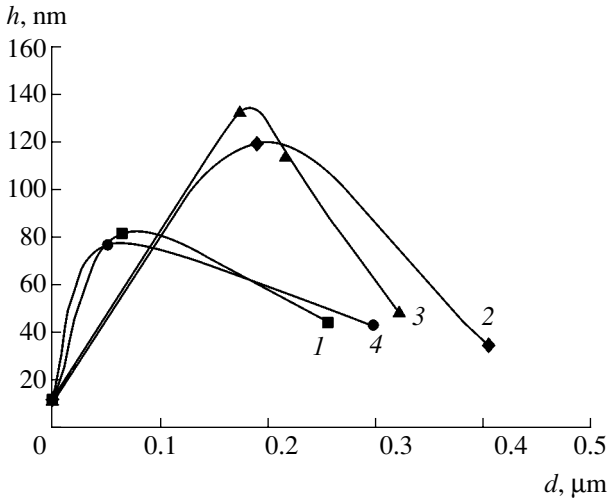

Fig. 4. A plot of the height of extracted microcrystals versus removed hydrocarbon layer thickness for various etching regimes (U, P) and initial film thicknesses (h): (*1*) h = 1.2 μm, U = –300 V, P = 0.05 Pa; (*2*) h = 0.4 μm, U = –300 V, P = 0.05 Pa; (*3*) h = 0.4 μm, U = +300 V, P = 0.05 Pa; (*4*) h = 0.4 μm, U = +300 V, P = 1 Pa.

REFERENCES

1. *Diamonds in Electronic Engineering*, Ed. by V. B. Kvaskov (Énergoatomizdat, Moscow, 1990).
2. B. V. Deryagin and D. V. Fedoseev, *Growth of Diamond and Graphite from Vapor Phase* (Nauka, Moscow, 1977).
3. A. N. Obraztsov, I. Yu. Pavlovskii, and A. P. Volkov, Zh. Tekh. Fiz. **71** (11), 89 (2001) [Tech. Phys. **46**, 1437 (2001)].
4. N. N. Bylinkina, S. P. Mushtakova, S. Yu. Suzdal'tsev, and R. K. Yafarov, Pis'ma Zh. Tekh. Fiz. **22** (21), 89 (1996) [Tech. Phys. Lett. **22**, 902 (1996)].
5. S. Yu. Suzdal'tsev, S. V. Sysuev, and R. K. Yafarov, Pis'ma Zh. Tekh. Fiz. **24** (4), 25 (1998) [Tech. Phys. Lett. **24**, 135 (1998)].
6. S. Yu. Suzdal'tsev and R. K. Yafarov, Pis'ma Zh. Tekh. Fiz. **27** (15), 77 (2001) [Tech. Phys. Lett. **27**, 656 (2001)].

Translated by P. Pozdeev

Technical Physics Letters, Vol. 29, No. 8, 2003, pp. 652–654. Translated from Pis'ma v Zhurnal Tekhnicheskoĭ Fiziki, Vol. 29, No. 15, 2003, pp. 80–86.

Anomalous Behavior of the Crystallographic and Electron States in $Mn_xZn_yFe_zO_4$ Ferrites

Z. A. Samoĭlenko, V. S. Abramov, and N. N. Ivakhnenko

Donetsk Physicotechnical Institute, National Academy of Sciences of Ukraine, Donetsk, Ukraine

Received March 3, 2003

Abstract—The process of structural self-organization in manganese zinc ferrites with arbitrarily varying cationic sublattice composition has been theoretically analyzed and experimentally studied by methods of X-ray diffraction and *K*-emission spectroscopy. It is shown that there are strong relations between various experimentally determined parameters. These relations possess an extremal character, which is manifested by "grooves" and "ridges" on the (E, ρ, I) surfaces. This behavior is explained based on the notions about the electron population of states stabilized due to spontaneous deformation of the crystal structure, which gives rise to a strong coupling effect. © *2003 MAIK "Nauka/Interperiodica".*

Previous investigations [1, 2] of single crystal $Mn_xZn_yFe_zO_4$ ferrites showed that important factors in this ferrite matrix are concentrational and structural inhomogeneities leading to tetragonal and rhombohedral distortions of the cubic structure and the cluster formation [3]. The tetragonal and orthorhombic distortions of the ferrite lattice (manifested by splitting of the lines of X-ray diffraction from the families of high-index planes) give rise to concentrational and structural inhomogeneities in the form of nanodimensional phase clusters (γ-Mn_2O_3, γ-Mn_3O_4, α-Fe_2O_3) [4] coherently linked to the main lattice.

An analysis of regions in the diffraction pattern, reflecting the most significant changes in the crystal structure, suggests that the aforementioned distortions are accompanied by changes in the population of crystallographic states. At the same time, an analysis of the fine structure of the X-ray emission spectra of manganese (MnK_β) measured in the ferrite samples revealed a change in population of the electron energy levels near the Fermi level [5].

Therefore, a question naturally arises concerning the relationship between changes in populations of the crystallographic and electron states, as well as the structural self-organization in $Mn_xZn_yFe_zO_4$ ferrites. Our Letter addresses both of these problems.

We have studied a series of manganese zinc ferrite spinels differing by the relative content of elements [6, 7], which was accompanied by changes in the X-ray density ρ:

Sample	Crystallochemical formula	X-ray density ρ, g/cm^3
SM-5	$(Mn^{2+}_{0.38}Zn^{2+}_{0.32}Fe^{3+}_{0.24}V^{(k)}_{0.06})[Mn^{3+}_{0.06}Fe^{2+}_{0.06}Fe^{3+}_{1.88}]O^{2-}_{3.99}V^{(a)}_{0.01}$	5.030
SM-6	$(Mn^{2+}_{0.52}Zn^{2+}_{0.32}Fe^{3+}_{0.02}V^{(k)}_{0.14})[Mn^{3+}_{0.03}Fe^{2+}_{0.03}Fe^{3+}_{1.94}]O^{2-}_{3.96}V^{(a)}_{0.04}$	5.062
SM-1	$(Mn^{2+}_{0.25}Zn^{2+}_{0.47}Fe^{3+}_{0.19}V^{(k)}_{0.09})[Fe^{3+}_{2.00}]O^{2-}_{3.99}V^{(a)}_{0.01}$	5.097
SM-7	$(Mn^{2+}_{0.55}Zn^{2+}_{0.40}V^{(k)}_{0.05})[Mn^{3+}_{0.04}Fe^{2+}_{0.04}Fe^{3+}_{1.92}]O^{2-}_{3.93}V^{(a)}_{0.07}$	5.125
SM-3	$(Mn^{2+}_{0.45}Zn^{2+}_{0.48}V^{(k)}_{0.07})[Mn^{3+}_{0.14}Fe^{2+}_{0.14}Fe^{3+}_{1.72}]O^{2-}_{3.96}V^{(a)}_{0.04}$	5.140

Figure 1 shows the X-ray diffraction patterns with background variations, measured for these $Mn_xZn_yFe_zO_4$ ferrite samples in the angular interval of 68°–72° using CrK_α radiation. The character of redistribution of the intensity of coherent X-ray scattering from the families of (444) and (700) planes with close values of interplanar distances allows this structure to be analyzed as a single object. Separate planes are considered as objects formed by the matrix lattice sites deviating from their equilibrium positions. This representation is equivalent to the presence of static spontaneous deformations (or a condensate of the local

phonon modes). Therefore, we can speak about the populations of particular planes and estimate these populations using intensities of the diffraction lines from the corresponding planes.

The densities n_1 and n_2 of active scattering lattice sites in the (444) and (700) planes, respectively, determined from the maximum scattering intensities for these planes are presented in the table below (in arbitrary units) together with the difference, calculated as $\Delta n = n_1(I) - n_2(I)$. The samples are arranged in order of increasing X-ray density (from SM-5 to SM-3).

	SM-5	SM-6	SM-1	SM-7	SM-3
$n_1(I)$, a.u.	96.0	100.0	92.6	98.0	75.6
$n_2(I)$, a.u.	94.2	94.8	92.6	103.0	75.8
Δn, a.u.	1.8	5.2	0	–5.0	–0.2

As can be seen from these data, the density of scattering centers in the (444) planes of samples SM-5 and SM-6 is greater than that in the (700) planes and, hence, the difference Δn is positive. In SM-1 sample, the two planes are equiprobably occupied by the scattering centers and $\Delta n = 0$. In SM-7 and SM-3 samples, the number of scattering sites is smaller in the (444) planes than in the (700) ones and Δn is negative. Thus, as the X-ray density monotonically increases, the difference of populations of the (444) and (700) planes in the ferrite lattice exhibits an anomalous behavior.

From the crystallographic standpoint, the above result implies that an increase in the X-ray density of ferrites leads initially to predominant occupation of the diagonal planes and then of the side planes, so that the population of crystallographic states exhibits a redistribution. On the other hand, the angular positions [8] of the diffraction maxima according to $2d\sin\theta = n\lambda$ indicate that the population is redistributed from "stretched" ($d > d_m$) to contracted ($d < d_m$) structural elements (d and d_m are the interplanar distances, d_m = 1.03 Å). This result indicates that a continuous increase in the density of $Mn_xZn_yFe_zO_4$ ferrites leads to periodic alternation of the stretched and contracted structural elements, which can be interpreted as the appearance of an internal elastic wave caused by a correlated variation of populations in the (444) and (700) planes.

Now let us elucidate the possible relationship between the previously reported behavior of populations of the electron states [5] and the above-described variation of populations of the crystallographic states. For this purpose, we have constructed a surface in the (E, ρ, I) space (Fig. 2) using the calculated discrete values of the energy E (determined from the fine structure of MnK_β spectra [5]), X-ray density ρ, and experimental data on relative intensities in the MnK_β emission spectra.

As can be seen, the (E, ρ, I) surface exhibits a groove along the *b*–*c*–*a* curve, the bottom of which is parallel to the ρ axis (at a fixed energy E_3 = 6495.05 eV) and has a wavy profile. Another characteristic feature on this surface is of the ridge type, with a monotonically increasing profile along the *m*–*l*–*k* curve and the vertex also parallel to the ρ axis at E_5 = 6496.83 eV. Let us compare the behavior of the two states on the passage along the groove bottom and the ridge vertex in the direction of increasing density. For the initial points *b* and *m* (ρ = 5.03 g/cm^3), the population of the energy state at E_3 ($I \approx 1$ a.u.) is greater than that of the E_5 state (I = 0.749 a.u.). At the final points *a* and *k* (ρ = 5.14 g/cm^3), the situation is the inverse: the population of the energy state at E_3 (I = 0.779 a.u.) is smaller than that of the E_5 state ($I \approx 1$ a.u.).

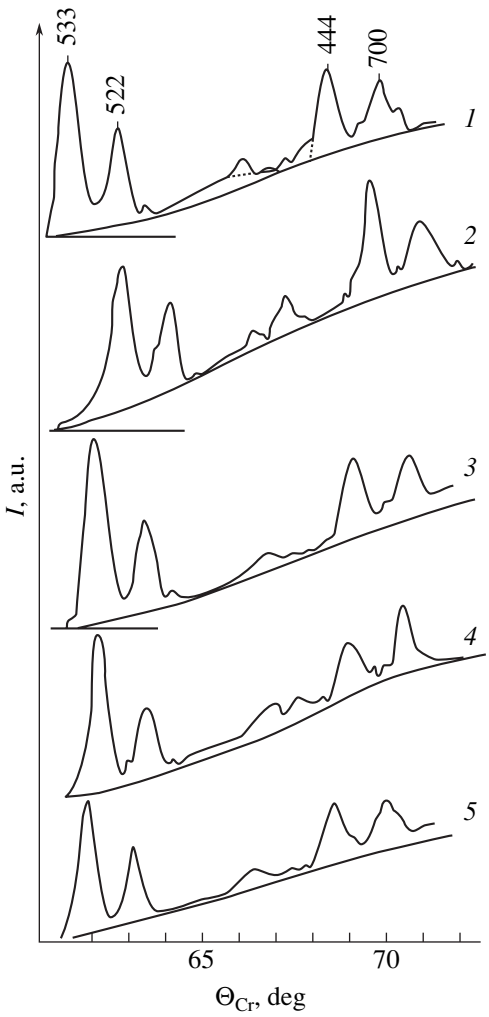

Fig. 1. Anomalous variation of the intensity I of the coherent X-ray scattering from (444) and (700) planes (showing a redistribution of populations of the corresponding crystallographic states) in $Mn_xZn_yFe_zO_4$ ferrites with increasing density: (*1*) SM-5; (*2*) SM-6; (*3*) SM-1; (*4*) SM-7; (*5*) SM-3.

These relief variations of the groove and ridge type reflect the mechanism of population redistribution between the electron states. Such a representation, taking into account simultaneous variation of the parame-

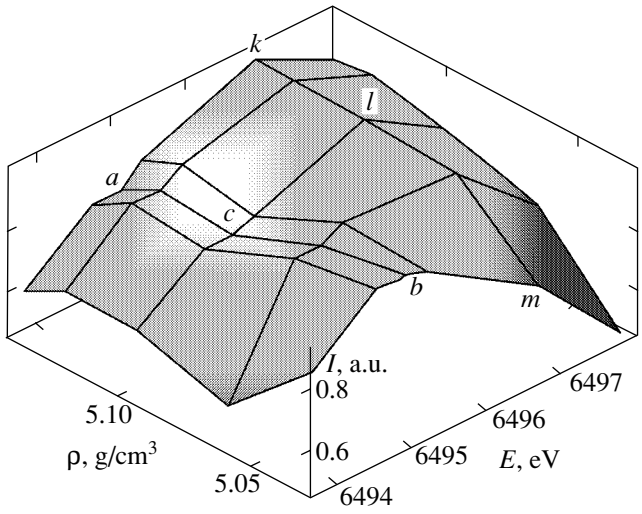

Fig. 2. Anomalous variation of the MnK_β emission intensity I as a function of the energy E of electron states and the density ρ of $Mn_xZn_yFe_zO_4$ ferrites.

ters ρ and E provides rich information concerning other possible mechanisms of population redistribution between the electron states and increases the value of the results obtained in [4, 5]. Geometrically, the analysis reduces to selecting an optimum pathway on the (E, ρ, I) surface.

Thus, an analysis of the behavior of crystallographic and electron states shows that, as the density ρ increases, the populations of these states exhibit redistribution. An arbitrary trajectory on the surface depicted in Fig. 2 corresponds to the relationship between ρ and E, which corresponds to a correlation between the crystallographic and electron states. The correlated variation of the electron and mass density in the ferrite structure may lead to an elastic-electron interaction, which can be responsible for a possible phase transition of the dielectric–metal type or the spontaneous electrostriction effect.

REFERENCES

1. V. I. Arkharov, V. P. Pashchenko, and N. V. Suntsov, Dokl. Akad. Nauk SSSR **268**, 84 (1983) [Sov. Phys. Dokl. **28**, 48 (1983)].
2. M. T. Varshavskii, V. P. Pashchenko, A. M. Men', *et al.*, *Defect Structure and Physicochemical Properties of Ferrite Spinels* (Nauka, Moscow, 1988).
3. Z. A. Samoĭlenko, V. S. Abramov, V. P. Pashchenko, *et al.*, Fiz. Tverd. Tela (St. Petersburg) **43**, 1496 (2001) [Phys. Solid State **43**, 1556 (2001)].
4. Z. A. Samoĭlenko, V. S. Abramov, V. P. Pashchenko, *et al.*, Fiz. Tekh. Vys. Davleniĭ **12**, 14 (2002).
5. Z. A. Samoĭlenko, V. S. Abramov, and N. N. Ivakhnenko, Pis'ma Zh. Éksp. Teor. Fiz. **72**, 679 (2000) [JETP Lett. **72**, 472 (2000)].
6. V. P. Pashchenko, A. M. Nesterov, Ya. G. Drigibka, *et al.*, Poroshk. Metall., No. 5/6, 89 (1994).
7. V. I. Arkharov, Z. A. Samoĭlenko, and V. P. Pashchenko, Neorg. Mater. **29**, 827 (1993).
8. L. I. Kitaĭgorodskiĭ, *X-ray Diffraction Analysis of Fine-Crystalline and Amorphous Solids* (GITTL, Moscow, 1952).

Translated by P. Pozdeev

Technical Physics Letters, Vol. 29, No. 8, 2003, pp. 655–657. Translated from Pis'ma v Zhurnal Tekhnicheskoĭ Fiziki, Vol. 29, No. 15, 2003, pp. 87–94.

Defect Formation in Epitaxial Layers of Cadmium Mercury Telluride Solid Solutions Highly Doped with Indium

K. D. Mynbaev* and V. I. Ivanov-Omskiĭ

Ioffe Physicotechnical Institute, Russian Academy of Sciences, St. Petersburg, 194021 Russia

** e-mail: mynkad@mail.ioffe.ru*

Received March 25, 2003

Abstract—We have studied the effect of strong (up to 5×10^{21} cm^{-3}) indium doping on the behavior of components in cadmium mercury telluride solid solutions. At an indium concentration in a modified subsurface layer on the order of 10^{21} cm^{-3}, these layers are depleted of mercury and cadmium; simultaneously, cadmium is segregated in the region immediately below the indium-doped surface layer. The strong doping with indium leads to the formation of extended defects, which is manifested by characteristic patterns in electron micrographs observed after chemical etching. The observed redistribution of the solid solution components upon doping is explained by peculiarities of the defect formation in cadmium mercury tellurides. © *2003 MAIK "Nauka/Interperiodica".*

Solid solutions of the cadmium mercury telluride $Cd_xHg_{1-x}Te$ (CMT) system possess unique physical properties and are still the base materials for infrared optoelectronics. The most widely used donor impurity for CMT is indium [1–3]. Advantages of this donor are the high electrical activity of In atoms in CMT matrix at usual working doping levels (up to 10^{18} cm^{-3}), well-known segregation coefficients for the growth doping process, and some others. At the same time, the solubility and diffusion mechanisms of In in CMT are still incompletely studied. It is believed that In does not affect the concentration of intrinsic defects in CMT at the dopant concentrations $<10^{17}$ cm^{-3} [4, 5]. On the other hand, it is known that In can dissolve in CMT up to concentrations above 10^{21} cm^{-3} [4, 6, 7], but the effects of In present in such amounts on the properties of the CMT matrix were never studied.

Here, we report on the results of investigation of the behavior of components in CMT solid solutions doped with indium in a range of concentrations C_{In} in the surface layer from 5×10^{19} up to 5×10^{21} cm^{-3}. The initial samples were the epitaxial layers of CMT with x = 0.20–0.52 grown on CdTe and CdZnTe substrates by liquid-phase epitaxy (LPE) from Te-rich solutions. After growth, the samples were equilibrated by thermal annealing in saturated mercury vapor for 100 h at T = 633 K. Then the samples were doped with indium by diffusion from a gas or solid phase. In the former case, the samples with CMT epilayers were placed into quartz ampules containing certain amounts of Hg and In, while in the latter case a ~1-μm-thick In layer was deposited on the CMT surface in vacuum. The diffusion treatment was performed in saturated mercury vapor at T = 633 K over a time period varied from 20 to 100 h. After diffusion, the doped samples were quenched down to room temperature.

The depth–concentration profiles of In and the solid solution components in the samples upon diffusion were obtained by methods of electron probe microanalysis (EPMA) and secondary ion mass spectrometry (SIMS). The former method was used for the depth profiling of most strongly doped samples, where the use of SIMS (effective for the analysis of small impurity concentrations) was difficult [8]. Using EPMA, it was also possible to study the distribution of elements in cleaved samples at a large step (~0.5 μm), which was important in the case of CMT epilayers with a variband structure. SIMS was used for determining C_{In} and the depth profiling of samples with $C_{In} < 10^{20}$ cm^{-3}.

We have determined the dopant concentration C_{In} in 30 diffusion doped CMT samples. The obtained C_{In} values ranged from ~5×10^{19} up to ~5×10^{21} cm^{-3}. It should be noted that our experiments with diffusion from the gas phase revealed no correlations between C_{In} and the experimental conditions such as the In weight in the ampule, mutual arrangement of the CMT sample and In, etc. Similar behavior was observed in [7] and is still not explained. The samples doped from the solid phase had $C_{In} \sim 1.5 \times 10^{21}$ cm^{-3}.

Figure 1 shows typical depth profiles of In and the solid solution components in CMT epilayers with x = 0.22 doped with indium from the gas phase. The measurements were performed on a cleaved sample by EPMA at a step of 0.5 μm. As can be seen, the initial CMT epilayer had a constant composition to a depth of

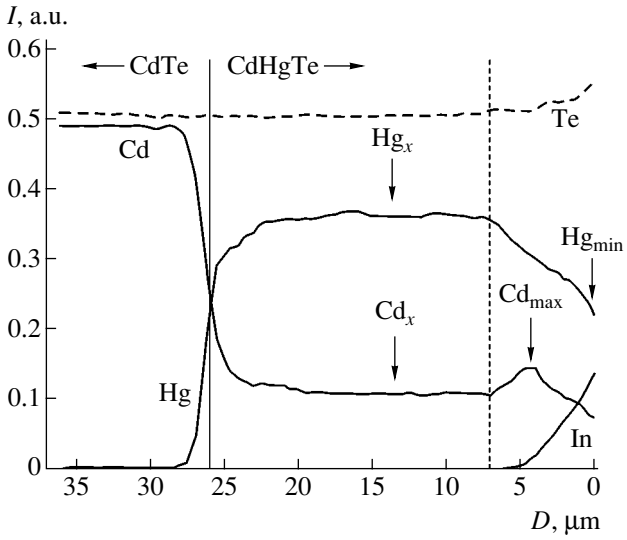

Fig. 1. Depth profiles of In, Cd, and Hg on the cleavage of CMT epilayers doped with indium from the gas phase (D is the distance from the sample surface). Vertical solid line indicates the substrate–epilayer interface; dashed line indicates the effective boundary of a layer featuring redistribution of the solid solution components. Arrows indicate the points at which the bulk element concentrations were determined for the ratios plotted in Fig. 2.

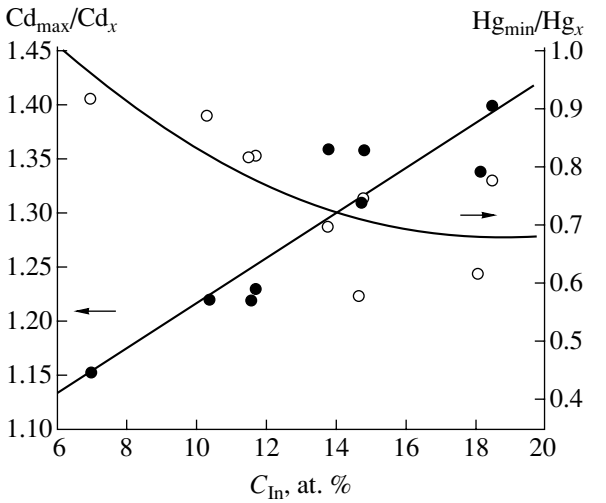

Fig. 2. Plot of the ratios Cd_{max}/Cd_x and Hg_{min}/Hg_x versus the indium concentration C_{In} for CMT epilayers with $x = 0.24$. The diffusion time for all samples was 40 h. See the text for explanations.

25 μm. The diffusion treatment resulted in a strong doping of the surface layer with indium. Simultaneously, this surface layer exhibits a strong depletion of mercury, a less pronounced depletion of cadmium, and a segregation of Cd in a layer immediately below the layer with the maximum indium concentration. All these changes are localized in a subsurface layer with the indium concentration above $\sim 5 \times 10^{19}$ cm^{-3} (a near-surface region with a thickness of ~7 μm). The content of Te in the solid solution was not measured directly and was determined by a difference method [9]. However, since the results of SIMS analyses revealed no impurities on the CMT surface at an amount in excess of 1 at. %, we can ascertain that an increase in the concentration of Te in the near-surface region of CMT in fact indicates that this region is enriched with tellurium. The pattern of redistribution of the solid solution components in the indium-doped CMT depicted in Fig. 1 was observed in all CMT epilayers with $C_{In} > 10^{21}$ cm^{-3} irrespective of the dopant source. In the samples with lower values of C_{In}, the depth profiles of Hg, Cd, and Te coincided with those in the initial (undoped) material.

Figure 2 shows a plot of the ratio of the maximum cadmium concentration (Cd_{max}) in the Cd-rich layer to that (Cd_x) in the region of a constant composition in the undoped CMT epilayers versus the indium concentration C_{In} (in at. %); an analogous plot is presented for the ratio of the mercury concentration on the surface (Hg_{min}) to that (Hg_x) in the region of a constant CMT composition in the epilayer. Together with the Hg and Cd profiles in Fig. 1, the behavior of Cd_{max}/Cd_x and Hg_{min}/Hg_x qualitatively reflects changes in the content of these elements in CMT as a result of indium doping. As can be seen, the increase in C_{In} is accompanied by a linear increase in Cd_{max}/Cd_x and by a monotonic decrease in Hg_{min}/Hg_x. These trends were observed in the epilayers of all CMT compositions studied, which implies that Cd_{max}/Cd_x and Hg_{min}/Hg_x depend only on C_{In}, while being independent of x.

An analysis of the In dopant distribution in the samples with large and small C_{In} values showed that both cases are characterized by a diffusion profile described by the erfc function in the near-surface region, with the subsequent sharp decay in the In concentration with depth. A similar shape of the In diffusion profile in CMT epilayers was described in [7]. The effective diffusion coefficient of indium amounts to $\sim 6 \times 10^{-13}$ cm^2/s, which is close to the values reported previously for the diffusion of In into CMT epilayers under moderate doping conditions [10].

Figure 3 shows an electron micrograph of the surface of CMT with $x = 0.22$ doped with indium from the gas phase to $C_{In} = 2.2 \times 10^{21}$ cm^{-3}. Immediately after diffusion, the surface of the epilayer was mirror smooth and showed no visible distinctions from the surface of initial samples. However, etching in a 10% $Br_2 : C_4H_9OH$ solution (which is a polishing medium for CMT) revealed a defect pattern observed in the upper part of the micrograph in Fig. 3. As can be seen, the defects represent a network of crystallographically oriented lines. An analogous defect pattern was revealed in all CMT epilayers strongly doped with indium. Apparently, the chemical polishing in the above medium was accompanied by selective etching along the extended defects formed in the presence of indium.

The above data on the change in the defect structure of CMT as a result of strong doping with indium can be

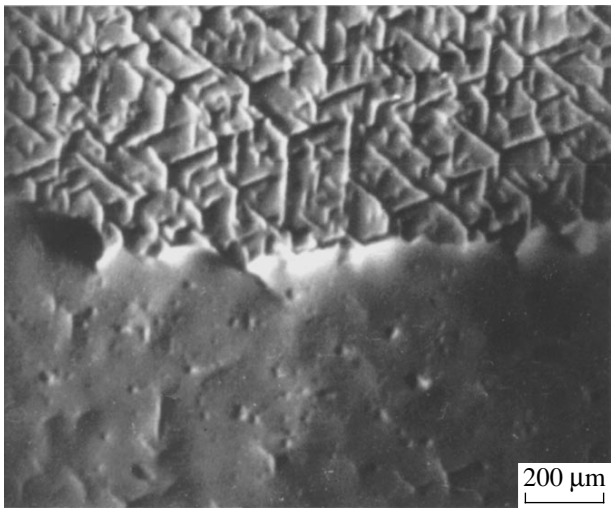

Fig. 3. An electron micrograph of the surface of CMT epilayer doped with indium from the gas phase to $C_{In} = 2.2 \times 10^{21}$ cm^{-3}. The upper part of the sample was chemically etched to remove a 1-μm-thick surface layer; the lower part was etched to a depth of 5 μm.

explained as follows. As is known, In atoms in CMT occupy lattice sites in the cation sublattice [2, 4, 6] and it is commonly accepted that these are predominantly the mercury sites. For $C_{In} > 10^{20}$ cm^{-3}, the incorporation of two In atoms in the lattice leads to the formation of one Hg vacancy. The interstitial mercury atoms (Hg_i) are highly mobile and eventually leave the crystal, which explains mercury depletion of the sample layer. The results of the present study show that In also occupies the Cd sites in CMT. Since extrapolation of the Cd_{max}/Cd_x versus C_{In} plot in Fig. 2 to $C_{In} = 0$ yields $Cd_{max}/Cd_x = 1$, it can be concluded that In begins to occupy the Cd sites even at low dopant concentrations. Since the density of Cd vacancies in the initial CMT epilayers is small, this process must be accompanied by the displacement of Cd from its lattice sites, which is evidence of the instability of these atoms in the CMT lattice.

The above conclusion agrees with the hypothesis of [7] and [11] that In diffuses in CMT at $T > 573$ both by a dissociative mechanism and by the interstitial mechanism through cadmium displacement. This explains the fact that the pattern of redistribution of the solid solution components observed at 633 K is different from that characteristic of the mutual diffusion in the In–CMT system at 300 K, according to which the surface is depleted of mercury and tellurium at a constant content of cadmium [12]. In our case, In is also active in the cadmium sublattice, while Cd atoms displaced into interstitials cannot diffuse to the surface because of a high concentration of In_i and Hg_i. As a result, cadmium atoms migrate inward into the crystal to form a Cd-rich layer at the boundary of the In distribution. The incorporation of In in so large amounts into the Hg and Cd sublattices gives rise to internal mechanical stresses. These stresses relax by forming extended defects revealed by the chemical etching as described above.

It should be noted that In-doped CMT epilayers exhibited *n*-type conductivity with the electron density on the level of ~10^{18} cm^{-3}. Taking this fact into account, we cannot speak of the formation of indium telluride in the epilayers studied [4, 13], which according to [14] is confirmed by the fact that the CMT surface was enriched with tellurium. However, CMT doped with indium to such a high level (~10^{21} cm^{-3}) is obviously inapplicable in practice. The maximum admissible level of the effective CMT doping with indium is $(1–3) \times 10^{18}$ cm^{-3}, when virtually all the introduced dopant atoms are electrically active [4, 5, 7] while still not affecting the solid solution matrix to any significant extent.

REFERENCES

1. H. R. Vydyanath, F. Aqariden, P. S. Wijewarnasuriya, *et al.*, J. Electron. Mater. **27**, 504 (1998).
2. M. A. Berding, J. Electron. Mater. **29**, 664 (2000).
3. H. G. Robinson, M. A. Berding, and W. J. Hamilton, J. Electron. Mater. **29**, 657 (2000).
4. H. R. Vydyanath, J. Electrochem. Soc. **128**, 2619 (1981).
5. V. I. Ivanov-Omskiĭ, K. E. Mironov, K. D. Mynbaev, *et al.*, Fiz. Tekh. Poluprovodn. (Leningrad) **25**, 1423 (1991) [Sov. Phys. Semicond. **25**, 857 (1991)].
6. D. Shaw, Phys. Status Solidi A **89** (1), 173 (1985).
7. G. Weck and K. Wandel, J. Vac. Sci. Technol. A **12**, 3023 (1994).
8. V. T. Cherepin, *Ion Microprobe Analysis* (Naukova Dumka, Kiev, 1992).
9. S. G. Konnikov and A. F. Sidorov, *Electron-Probe Analysis of Semiconductors* (Moscow, 1978).
10. K. E. Mironov, K. D. Mynbaev, and V. I. Ivanov-Omskiĭ, Fiz. Tekh. Poluprovodn. (Leningrad) **24**, 582 (1990) [Sov. Phys. Semicond. **24**, 368 (1990)].
11. F. A. Zaitov, F. K. Isaev, and A. V. Gorshkov, *Defect Formation and Diffusion Processes in Some Semiconductor Solid Solutions* (Azerbaidzhan Gos. Izd., Baku, 1984).
12. I. S. Virt, V. I. Kempnik, and D. I. Tsyutsyura, Izv. Akad. Nauk SSSR, Neorg. Mater. **22**, 1402 (1986).
13. G. N. Pain and T. McAllister, Semicond. Sci. Technol. **7**, 231 (1992).
14. P. F. Vengel' and V. N. Tomashik, Izv. Akad. Nauk SSSR, Neorg. Mater. **26**, 278 (1990).

Translated by P. Pozdeev

Technical Physics Letters, Vol. 29, No. 8, 2003, pp. 658–660. Translated from Pis'ma v Zhurnal Tekhnicheskoĭ Fiziki, Vol. 29, No. 16, 2003, pp. 1–5.

The Effect of Dissipation on the Instability of a Superthreshold Electron Beam

S. A. Babayan, E. V. Rostomyan*, and Yu. G. Sanoyan

Institute of Radiophysics and Electronics, National Academy of Sciences of Armenia, Yerevan, Armenia

** e-mail: evrostom@freenet.am; evrostom@irphe.am*

Received March 11, 2003

Abstract—We have studied the effect of dissipation on the development of instability in a superthreshold electron beam. The instability is related to an aperiodic modulation of the beam current density in a medium with negative dielectric permittivity. It is shown that the dissipative instability increment in a superthreshold electron beam depends on the dissipation level stronger than in a subthreshold beam. *© 2003 MAIK "Nauka/Interperiodica".*

One of the main trends in modern relativistic microwave electronics is the passage to still higher frequencies, which leads to decreasing skin layer thicknesses on the cavity walls [1] and, in turn, to increasing energy losses. The energy dissipation can become a decisive factor limiting the spatial and temporal increase in the field strength. This phenomenon can also significantly influence the spectrum of excited waves and reduce the increments. At the same time, dissipation will never fully suppress the instability. A strong dissipation can change the character of the beam instability, converting it into a different type, called dissipative. This type of instability can appear in systems with electron beams featuring a beam wave of negative energy. Here, dissipation is essentially a channel providing the energy necessary for exciting a beam wave with negative energy. Instabilities of this type differ from the usual beam instability by possessing a small increment and a relatively low level of excited oscillations [2, 3].

Another tendency in microwave electronics is to increase the beam current in order to provide for a greater output radiation power. Independently of the strong dissipation, this factor also leads eventually to a change in the character of beam instability. As is known, a beam current that can be transmitted via a given electrodynamic system is limited by the beam space charge. Then, instability of a superthreshold electron beam is caused either by an aperiodic modulation of the beam current density in a medium with negative dielectric permittivity or by the excitation of a beam wave with negative energy, rather than by the induced emission of waves by electrons of the beam [4–6]. This change in the physical character of the beam instability is also related to the beam space charge.

This Letter addresses the effect of dissipation on the development of instability in a superthreshold electron beam as a result of an aperiodic modulation of the beam current density in a medium with negative dielectric permittivity. This type of instability is developed in a superthreshold electron beam transmitted via a magnetized beam–plasma waveguide with homogeneous cross section. As expected, the increment of the dissipative instability in the superthreshold electron beam depends on the effective collision frequency in the plasma to a greater extent than in a subthreshold beam.

Consider a cylindrical waveguide filled with a homogeneous cold plasma and penetrated with a monoenergetic relativistic electron beam. The external magnetic field is assumed to be sufficiently strong to freeze the transverse motion of electrons in the beam and plasma. A symmetric E mode with nonzero field components E_r, E_z, and B_φ related to this beam is described by the dispersion equation

$$k_\perp^2 + \left(k^2 - \frac{\omega^2}{c^2}\right)\left(1 - \frac{\omega_p^2}{\omega(\omega + i\nu)} - \frac{\omega_b^2}{\gamma^3(\omega - ku)}\right) = 0, \quad (1)$$

where ω and k are the frequency and longitudinal wave vector; $k_\perp = \mu_{0s}/R$; R is the waveguide radius; μ_{0s} are the roots of the Bessel function J_0; $\omega_{b,p}$ are the Langmuir frequencies of the beam and plasma, respectively; $\gamma = (1 - u^2/c^2)^{-1/2}$; ν is the effective frequency of collisions in the plasma; u is the electron velocity in the beam; and c is the speed of light.

The character of the beam–plasma interaction and the development of instability, as well as the effect of dissipation on these processes, change depending on the beam current. These changes are manifested in the structure of solutions of Eq. (1). Let us seek solutions

1063-7850/03/2908-0658$24.00 © 2003 MAIK "Nauka/Interperiodica"

in the form $k = \frac{\omega}{u} + q$, where $|q| \ll \omega/u$. The dispersion equation acquires the form

$$x^3 - i\frac{1}{2\gamma^2}\frac{\nu}{\omega_0}\frac{\omega_p^2}{\omega_\perp^2}x^2 + x\frac{\alpha}{\gamma^2} = -\frac{\alpha}{2\gamma^4}, \qquad (2)$$

where $x = qu/\omega$, $\alpha = \omega_b^2/k_\perp^2 u^2\gamma^3$, $\omega_\perp^2 = k_\perp^2 u^2\gamma^2$, and $\omega_0^2 = \omega_p^2 - \omega_\perp^2$ is the resonance frequency of the plasma waveguide. It was demonstrated [5] that the resonance frequency of the plasma waveguide remains constant when the beam current is on the order of a threshold current in vacuum or slightly exceeds this threshold. Our consideration is restricted to this very case. Otherwise, the dynamics of instability development becomes extremely complicated [7].

The solutions to Eq. (2) significantly depend on the parameter α. This parameter essentially determines the beam current and the character of the beam–plasma interaction. As can be seen, this parameter is proportional (with a factor on the order of γ^{-2}) to the ratio of the beam current I_b to the vacuum threshold current I_0: $\alpha = (I_b/I_0)\gamma^{-2}$. Then, the case of $\alpha \ll \gamma^{-2}$ corresponds to subthreshold currents $I_b \ll I_0$ and the instability caused by the induced emission of waves by electrons of the beam. In this case, the spatial increments of both usual and dissipative beam instabilities (i.e., without dissipation and with strong dissipation, respectively) in the plasma waveguide can be readily found by solving Eq. (2):

$$q_{sbl} = \frac{\sqrt{3}}{2}\frac{\omega}{u}\left(\frac{\omega_b^2}{2k_\perp^2 u^2\gamma^7}\right)^{1/3}; \quad q_{sbl}^{(\nu)} = \frac{1}{2}\frac{\omega_b}{\sqrt{\nu}}\frac{\omega_0^{3/2}}{\gamma^{3/2}u\omega_p}. \quad (3)$$

The difference between the expression for $q_{sbl}^{(\nu)}$ and analogous expressions obtained previously is related to the system geometry, the model considered here being closer to real systems.

Now let us compare the increments (3) to the results corresponding to a superthreshold electron beam. As noted above, large beam currents also influence the physical nature of the instability. As the beam current increases so as to obey the condition $\gamma^{-2} \ll \alpha \ll 1$, the space charge effects alter the nature of the instability, which becomes like that in a medium with negative dielectric permittivity. Here, the increment reaches maximum exactly at the Cherenkov resonance. The solutions to Eq. (2) in the cases without dissipation and with strong dissipation are, respectively, as follows:

$$q_{ovl} = \frac{\omega}{u}\left(\frac{\omega_b^2}{k_\perp^2 u^2\gamma^5}\right)^{1/2}, \quad q_{ovl}^{(\nu)} = 2\frac{\omega_b^2}{\nu}\frac{\omega_0^2}{u\gamma\omega_p^2}. \qquad (4)$$

The first expression (4) corresponds to the time increment of instability of a superthreshold beam, $\delta_0 = \omega_b(u/c)/\gamma^{1/2}(1 + \omega_\perp^2\gamma^2/\omega_0^2)$ [5], which depends on the electron density n_b in the beam as $\delta_0 \sim \sqrt{n_b}$. The second expression (4) shows that the nature of the instability in a superthreshold beam with a small thermal scatter changes with increasing dissipation level. The instability becomes dissipative, which is manifested by a stronger dependence on the parameter describing the dissipation: $\nu^{-1/2} \longrightarrow \nu^{-1}$. As the beam current (i.e., electron density) increases, the natural electron oscillations are more effectively manifested and excite a beam wave with negative energy, which provides a channel for effective energy removal.

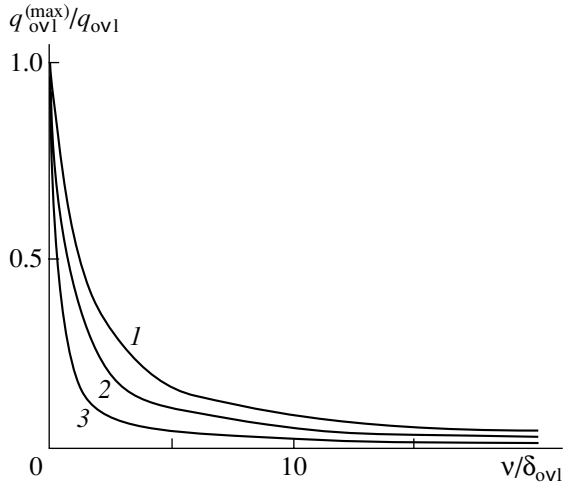

Plots of the maximum increment on the level of dissipation calculated for $y = 1.44$ (*1*), 4 (*2*), and 25 (*3*).

In order to study the transformation of the instability in a superthreshold beam into the dissipative type and find the increment for an arbitrary value of the parameter $\lambda \equiv \nu/\delta$, note that the right-hand part of Eq. (2) is not as significant for superthreshold beams. Then, Eq. (2) can be transformed to the equation

$$x^2 - 2i\nu(\omega_p^2/\gamma^2\omega_0\omega_\perp^2)x + uq_{ovl}/\omega_0 = 0, \qquad (5)$$

which has the solution

$$q_{ovl}^{(max)}(\lambda) = q_{ovl}\{\sqrt{1 + \lambda^2 y} - \lambda\sqrt{y}\}, \qquad (6)$$

where $y = 1 + \omega_0^2/\omega_\perp^2\gamma^2$. In the limit of $\lambda \gg 1$, this yields $q_{ovl}^{(max)} \longrightarrow q_{ovl}^{(\nu)}$. Plots of the maximum increment on the level of dissipation in the system studied are presented in the figure. As can be seen, the first increment (4) gradually converts into the second increment (4) and the instability acquires a dissipative character.

Acknowledgments. This study was supported by the Armenian National Science and Education Foundation (ANSEF).

REFERENCES

1. *Relativistic Microwave Electronics: Collection of Scientific Works*, Ed. by A. V. Gaponov-Grekhov (Gor'kiĭ, 1981).
2. H. Bohmer, J. Chang, and M. Raether, Phys. Fluids **14**, 150 (1971).
3. V. U. Abramovich and V. I. Shevchenko, Zh. Éksp. Teor. Fiz. **62**, 1386 (1972) [Sov. Phys. JETP **35**, 730 (1972)].
4. M. V. Kuzelev and A. A. Rukhadze, *Electrodynamics of Dense Electron Beams in a Plasma* (Nauka, Moscow, 1990).
5. N. I. Aĭzatskiĭ, Fiz. Plazmy **6**, 597 (1980) [Sov. J. Plasma Phys. **6**, 327 (1980)].
6. E. V. Rostomyan, Eur. Phys. J.: Appl. Phys. **14**, 177 (2001).
7. E. V. Rostomyan, Zh. Tekh. Fiz. **62** (7), 167 (1992) [Sov. Phys. Tech. Phys. **37**, 702 (1992)].

Translated by P. Pozdeev

Technical Physics Letters, Vol. 29, No. 8, 2003, pp. 661–662. Translated from Pis'ma v Zhurnal Tekhnicheskoĭ Fiziki, Vol. 29, No. 16, 2003, pp. 6–10.

A Mechanism of the Divacancy Complex Migration in a Two-Dimensional Ni_3Al Crystal

M. D. Starostenkov, E. A. Dudnik, and V. G. Dudnik

Altai State Technical University, Barnaul, Russia

e-mail: genphys@agtu.secna.ru

Received March 12, 2003

Abstract—A mechanism of the transformation of divacancies into complexes comprising an interstitial atom and three vacancies and peculiarities of the migration of such complexes in a two-dimensional Ni_3Al crystal have been studied by the method of molecular dynamics. *© 2003 MAIK "Nauka/Interperiodica".*

It is now reliably established that atomic diffusion in metal systems proceeds according to the vacancy mechanism [1]. However, it was suggested that, under certain conditions, a divacancy mechanism can be competitive to the vacancy diffusion [2]. The results of our computer simulation reported here are indicative of the possibility of impurity diffusion by a divacancy mechanism in a two-dimensional (2D) structure of the intermetallic compound Ni_3Al.

The 2D structure of the intermetallic compound Ni_3Al was characterized by a hexagonal close packing corresponding to the {111} plane of the $L1_2$ superstructure. The interactions in various atomic pairs were described by the pairwise central Morse potentials with the parameters taken from [3]. The calculation cell in the numerical experiment consisted of 3000 atoms, the 2D package outside the cell being determined by periodic boundary conditions. Diffusion processes in the system were simulated by the method of molecular dynamics. The distribution of the atomic oscillation rates as a function of the temperature was set in terms of the Boltzmann factor [4]. The vacancy pairs in the initial configurations were spaced by distances from the first to fifth coordination spheres. The structure rearrangement in the vicinity of the divacancy complexes was studied assuming rapid cooling of the crystal upon thermal activation.

It was found that, as the spacing between the pairs of vacancies increases, the activation temperature of the structure rearrangement changes accordingly. The minimum temperature at which a divacancy complex is reconstructed corresponds to the pair of closest vacancies formed in the neighboring Al and Ni lattice sites. As a result of the thermoactivated relaxation at $T \approx 100$ K, the boundary of the final arrangement is represented by a deformed truncated triangle with the sides formed by two and three neighboring atoms. The triangle is centered at an interstitial Ni atom. The voids inside the triangle show three vacancy positions: two at the Ni lattice sites and one at the Al site (Fig. 1). As the temperature increases to $T = 300$ K, the truncated triangle formed by the nearest neighbors of the interstitial atom shifts by a distance equal to one spacing between the atomic rows. This is accompanied by the following transformation: the interstitial position at the center is occupied by an Al atom and one of the positions in the truncated triangle is occupied by a point defect of substitution at the Al lattice site. As a result, the internal energy of the system decreases by $\Delta E \approx 0.2$ eV.

The structural rearrangement at the pair of vacancies formed in the two neighboring Ni lattice sites takes place at $T = 200$ K. As a result, an analogous truncated triangle is formed by the nearest neighbors of an interstitial Al atom, with voids corresponding to two vacancies in the Ni lattice sites and one in the Al site. Relaxation does not change the internal energy of the initial and final states. As the temperature increases to $T = 300$ K, the truncated triangle formed by the nearest neighbors of the interstitial atom shifts by a distance equal to one spacing between the atomic rows. In this case, no point substitution defect is formed.

At higher temperatures, similar rearrangements are observed at the pairs of vacancies occurring in the second to fourth coordination spheres. However, these reconstructions involve the formation of additional point substitution defects. As the temperature grows and the duration of the thermoactivated process increases, a divacancy complex transformed into the complex of interstitial atom and three vacancies migrates over the crystal structure. This is accompanied by an increase in the concentration of point substitution defects created by the moving system of an interstitial atom and three vacancies (Fig. 2). Upon rapid cooling, disordered regions appear in the superstructure and the internal energy of the system increases.

As for the mobility of divacancy complexes, these systems are more active as compared to single vacancies and separate point substitution defects. The results of our computer simulation showed that single vacancies are activated at 450–500 K. Their migration veloc-

1063-7850/03/2908-0661$24.00

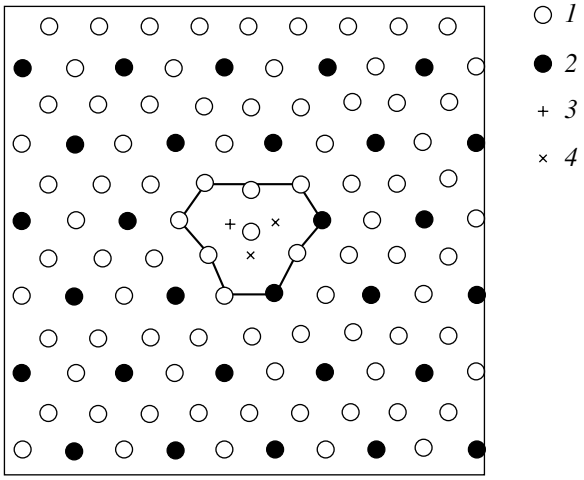

Fig. 1. A schematic diagram illustrating transformation of a divacancy into a complex comprising one interstitial atom and three vacancies in a 2D crystal lattice of Ni_3Al: (*1*, *2*) lattice sites of Ni and Al, respectively; (*3*, *4*) Al and Ni vacancies, respectively. Solid lines indicate a truncated triangle formed by the nearest neighbors of the interstitial Ni atom.

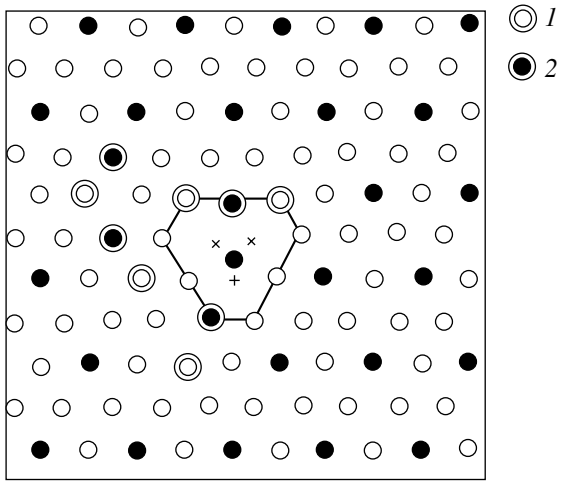

Fig. 2. A schematic diagram showing the elements of disorder generated by a divacancy at $T = 900$ K for the process duration of 15 ps: (*1*, *2*) point substitution defects at Ni and Al lattice sites, respectively.

ities are lower and the contribution to the process of superstructure disordering with increasing temperature is not as pronounced. The experiment with a crystal containing a single point substitution defect showed that the position of this defect remained unchanged as the temperature increases up to 1100–1200 K.

When a single point substitution defect and a single vacancy are present in the initial Ni_3Al crystal and the pair is spaced by a distance at which no interaction takes place, the situation remains unchanged in a temperature interval from 450 to 1100 K. However, a closely spaced pair of a single point substitution defect and a single vacancy features structural rearrangement that may lead to annihilation of the point substitution defect, after which the process continues by the vacancy mechanism.

The results of our computer simulations lead to the following conclusions. The mobility of divacancy complexes is determined by that of the interstitial atom and by a greater number of degrees of freedom (smaller number of bonds) as compared to the case of a single vacancy or a point substitution defect. An atom moving to occupy a single vacancy has to travel a distance equal to the interatomic spacing in the crystal; unlike this, the motion of the aforementioned divacancy complex involves two atoms, each traveling half such a distance (one atom passes from interstitial position to vacancy, and the other, from a lattice site into the interstitial position).

Acknowledgments. This study was supported by the Russian Foundation for Basic Research, project no. 02-02-17875.

REFERENCES

1. J. W. Christian, *The Theory of Transformations in Metals and Alloys* (Pergamon, Oxford, 1975; Mir, Moscow, 1978).
2. A. N. Orlov, *Introduction to the Theory of Crystal Defects* (Vysshaya Shkola, Moscow, 1983).
3. N. V. Gorlov, Candidate's Dissertation (Tomsk, 1987).
4. M. D. Starostenkov, G. M. Poletayev, and D. M. Starostenkov, J. Mater. Sci. Technol. **17** (1), 59 (2001).

Translated by P. Pozdeev

Technical Physics Letters, Vol. 29, No. 8, 2003, pp. 663–665. Translated from Pis'ma v Zhurnal Tekhnicheskoĭ Fiziki, Vol. 29, No. 16, 2003, pp. 11–15.

The Transition from 2D to 3D Nanoclusters of Silicon Carbide on Silicon

Yu. V. Trushin[a,*], K. L. Safonov[a], O. Ambacher[b], and J. Pezoldt[b]

[a] *Ioffe Physicotechnical Institute, Russian Academy of Sciences, St. Petersburg, 194021 Russia*

[b] *Zentrum Für Mikro- und Nanotechnologien, TU Ilmenau, Postfach 100565, 98684 Ilmenau, BR Deutschland*

** e-mail: trushin@theory.ioffe.rssi.ru*

Received April 9, 2003

Abstract—We have evaluated the critical average distance between the nanoclusters of silicon carbide grown by molecular beam epitaxy on silicon and estimated the time of the transition from two- to three-dimensional growth. © *2003 MAIK "Nauka/Interperiodica".*

Previously, we started with experimental investigations of the growth of SiC nanoclusters on silicon [1, 2] and provided a theoretical description of this process [3–5]. However, the question as to what physical factors account for the transition from 2D to 3D growth of nanoclusters in the SiC/Si heteroepitaxial system still remains unanswered. In this Letter, we propose a qualitative analysis of this problem as related to the current experiments.

Based on the experimental data [1], let us assume that the molecular beam epitaxy (MBE) at 660°C has led to the formation of 2D (monolayer) nanoclusters of SiC on Si. The clusters have an average radius of R_* and are spaced by an average distance of L, which corresponds to an average surface density of the clusters $C_c \approx 1/L^2$ (Fig. 1). In a thermodynamic equilibrium, let the densities of the interstitial silicon atoms be C_i^{eA}(Si) in the regions between nanoclusters (regions A in Fig. 1) and C_i^{eI} (Si) inside the nanoclusters (regions I).

In regions A, the interstitials are characterized by a relaxation volume of $\Delta\Omega_i^A \approx \Omega_{\mathrm{Si}}$(Si) that is approximately equal to the volume of a silicon atom in the silicon matrix. Since the average atomic parameters of silicon carbide (a_{SiC} = 4.35 Å) and silicon (a_{Si} = 5.43 Å) are such that $a_{\mathrm{Si}} > a_{\mathrm{SiC}}$, one can assume that a silicon atom is less confined in the SiC structure (i.e., in a cluster representing region I) than in region A, so that the corresponding relaxation volume is

$$\Delta\Omega_i^I \approx (a_{\mathrm{SiC}})^3 < \Delta\Omega_i^A. \quad (1)$$

Let us qualitatively consider the possibility that a 3D nanocluster begins to grow as a result of the jumps of Si atoms from region A to region I (nanoclusters), that is, from more to less confined state. According to [6–8], the expressions for the equilibrium densities of interstitial Si atoms in various regions ($F = A$ or I) are as follows:

$$C_i^{eF} = \chi_i^F \rho_n^{\mathrm{Si}}(F) \exp\{-\varepsilon_i^f(F)/kT\},$$

where

$$\chi_i^F = \exp\{-E_i^F/kT\}, \quad (2)$$

E_i^F is the energy of interaction between an interstitial Si atom in region F and a nanocluster creating stress σ^F in the regions between nanoclusters (regions A) and in the clusters proper (regions I),

$$E_i^F = \Delta\Omega_i^F \mathrm{Sp}\sigma^F, \quad (3)$$

ρ_n^{Si} is the density of silicon nuclei in region F; $\varepsilon_i^f(F)$ is the energy required for the formation of an interstitial Si atom in region F; k is the Boltzmann constant; and T is the absolute temperature.

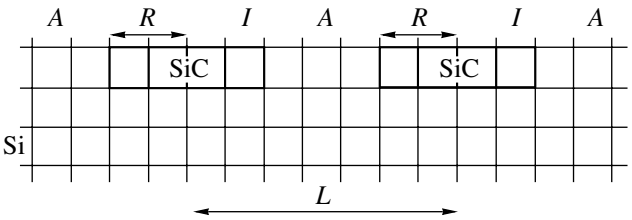

Fig. 1. A schematic diagram showing two-dimensional SiC nanoclusters of radius R (regions I) with an average spacing L on silicon substrate (regions A).

1063-7850/03/2908-0663$24.00 © 2003 MAIK "Nauka/Interperiodica"

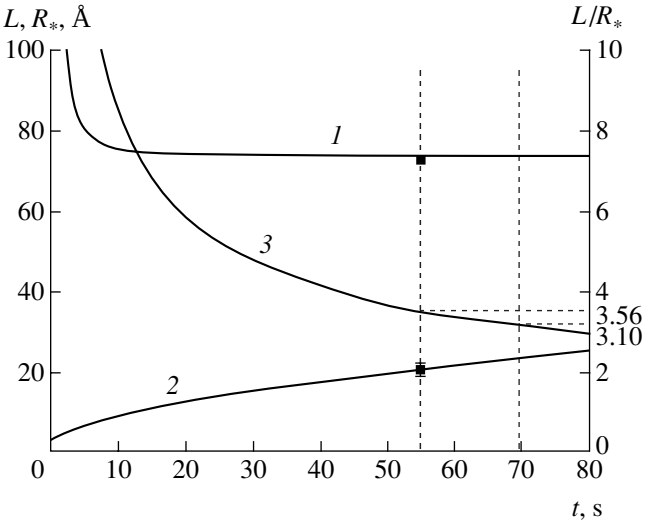

Fig. 2. Calculated plots of (*1*) the average spacing L between monolayer nanoclusters, (*2*) their average radius R_*, and (*3*) the L/R_* ratio versus MBE time. Black squares represent the experimental values of $L^e = 72.7$ Å and $R_*^e = 20.4$ Å determined for $t = 55$ s.

For $\mathrm{Sp}\sigma^F$, we have [6–9]

$$\mathrm{Sp}\sigma^A = -\frac{2E}{1-\nu}\eta_C(\varepsilon_A - \varepsilon_I),$$

$$\mathrm{Sp}\sigma^I = \frac{2E}{1-\nu}(1-\eta_C)(\varepsilon_A - \varepsilon_I),$$

where E is the Young modulus, ν is the Poisson ratio, ε_A and ε_I are the relative deformation inside and outside a nanocluster, respectively, and η_C is the surface fraction of nanoclusters (regions *I*).

Since regions *A* (between nanoclusters) are more confining for interstitial Si atoms than nanoclusters (regions *I*), we have

$$\left|E_i^A\right| / \left|E_i^I\right| > 1. \tag{4}$$

Formula (3) yields

$$E_i^A = \frac{2E}{1-\nu}(\varepsilon_1 + \varepsilon')\Delta\Omega_i^A\eta_C,$$
$$E_i^I = -\frac{2E}{1-\nu}(\varepsilon_I + \varepsilon')\Delta\Omega_i^I(1-\eta_C). \tag{5}$$

Substituting expressions (5) into (4) and taking into account relation (1), we obtain

$$\frac{\Delta\Omega_i^A\eta_C}{\Delta\Omega_i^I(1-\eta_C)} > 1. \tag{6}$$

Introducing the notation $\Delta\Omega_i^A/\Delta\Omega_i^I \equiv \alpha$, relation (6) can be rewritten as

$$\eta_C > 1/(1+\alpha).$$

For $\eta_C \approx \pi R_*^2/L^2$, a condition for the onset of silicon jumping from confined regions *A* ("first floor" between nanoclusters) to the "second floor" of monolayer nanoclusters is obtained in the following form:

$$L < \{\pi(1 + \Delta\Omega_i^A/\Delta\Omega_i^I)\}^{1/2}R_* = L_C. \tag{7}$$

Let us estimate the critical distance L between nanoclusters according to relation (7), below which Si atoms will be driven out from regions *A* to the second layer of regions *I*. Using the values $\Delta\Omega_i^F$ of the relaxation volume presented above, we obtain $\alpha \approx 2$ and $L_C \approx 3.1R_*$. Thus, a 3D growth of nanoclusters begins when the average spacing between 2D nanoclusters reaches a critical value on the order of $L_C \approx 3.1R_*$.

Processing of the electron micrographs of nanoclusters formed during the MBE of SiC on Si [2, 3] gave a distribution function $f(R)$ of the dimensions of monolayer nanoclusters R formed by the time of $t = 55$ s [3, 4]. By solving a system of equations for the $f(R)$ function, the concentration of carbon atoms, the density of diatomic SiC clusters, and the cluster size $R(t)$ as a function of the time, we obtained the $f(R)$ curve presented in [3, 4]. A good coincidence of the experimental distribution function and the calculated curve showed that quite realistic kinetic parameters were selected for the model calculation.

Thus, we can use an estimate of $L/R_* = 3.56$ obtained for $t = 55$ s, which must correspond to the state of monolayer clusters. This state is confirmed in experiment. Experimental values of the average nanocluster radius (20.4 Å) and the average spacing between such nanoclusters (72.7 Å) also agree quite well with the theoretical estimates $R_* = 20.9$ Å and $L = 73.7$ Å (see Fig. 2, curves *1* and *2*). Based on this coincidence, we can predict that the critical ratio $L_C/R_* \approx 3.1$ will be reached for an MBE process duration on the order of 70 s (Fig. 2, curve *3*).

Acknowledgments. The authors are grateful to A.A. Shmidt, V.S. Kharlamov, and E.E. Zhurkin for fruitful discussions.

This study was supported by the Russian Foundation for Basic Research (project no. 02-02-17605), by the Federal Program for Support of Leading Scientific Schools, and by the DAAD Program "Internationale Qualitätsnetzwerke (IQN): Ilmenauer Koordinationszentrum."

REFERENCES

1. W. Attenberger, J. Lindner, V. Cimalla, and J. Pezoldt, Mater. Sci. Eng., B **61**/**62**, 544 (1999).
2. F. Scharmann, J. Lindner, J. Pezoldt, *et al.*, Thin Solid Films **380**, 92 (2000).
3. D. V. Kulikov, K. L. Safonov, Yu. V. Trushin, and J. Pezoldt, in *Proceedings of the 4th Moscow International School of Physics "Modern Condensed Matter Physics: Experimental Methods and Devices, Related Topics,"* Ed. by A. L. Suvorov, Yu. G. Abov, and V. G. Firsov (Akademprint, Moscow, 2001), pp. 299–303.
4. K. L. Safonov, D. V. Kulikov, Yu. V. Trushin, and J. Pezoldt, Proc. SPIE **4627**, 165 (2002).
5. K. L. Safonov, D. V. Kulikov, Yu. V. Trushin, and J. Pezoldt, in *Proceeding of the 6th International Workshop on New Approaches to High-Tech: Nondestructive Testing and Computer Simulations in Science and Engineering, St. Petersburg, 2002*, Vol. 6, p. D4.
6. Yu. V. Trushin, Zh. Tekh. Fiz. **57**, 226 (1987) [Sov. Phys. Tech. Phys. **32**, 136 (1987)].
7. Yu. V. Trushin, *Theory of Radiation Processes in Metal Solid Solutions* (Nova Science, New York, 1986).
8. Yu. V. Trushin, *Radiation Processes in Multicomponent Materials: Theory and Computer Simulation* (Fiz.-Tekh. Inst. im. A. F. Ioffe, St. Petersburg, 2002).
9. C. Teodosiu, *Elastic Models of Crystal Defects* (Springer-Verlag, Berlin, 1982; Mir, Moscow, 1985).

Translated by P. Pozdeev

Technical Physics Letters, Vol. 29, No. 8, 2003, pp. 666–668. Translated from Pis'ma v Zhurnal Tekhnicheskoĭ Fiziki, Vol. 29, No. 16, 2003, pp. 16–22.

The Current of an Annular Electron Beam with Virtual Cathode in a Drift Tube

S. Ya. Belomyttsev, A. A. Grishkov, S. D. Korovin, and V. V. Ryzhov*

Institute of High-Current Electronics, Siberian Division, Russian Academy of Sciences, Tomsk, Russia

** e-mail: ryzhov@to.hcei.tsc.ru*

Received March 11, 2003

Abstract—An analysis based on the laws of conservation of energy and the z components of the field and particle momentum shows that a thin magnetized annular electron beam in a homogeneous drift tube behind a virtual cathode under stationary conditions occurs in a "squeezed" state corresponding to a slow left-hand branch of the current characteristic with a relativistic factor in the interval $1 \le \gamma \le \Gamma^{1/3}$. The beam current I_1 behind the virtual cathode in a homogeneous drift tube can vary from zero up to a limiting value $I_{\lim}$, while the injection currents (I_2) and the current of electrons reflected from the virtual cathode (I_3) for every stationary state are single-valued functions of I_1 and fall within the intervals $I_F/2 \le I_2 \le I_{\lim}$ and $0 \le I_3 \le I_F/2$, respectively, where I_F is the Fedosov current. © *2003 MAIK "Nauka/Interperiodica".*

An analysis of the properties of a virtual cathode (VC) is important in solving problems related to the generation of microwave radiation in vircators [1]. In the context of a discussion concerning the current behind the VC [2, 3], it will be shown by a simple example that, in the stationary case, this current can vary within a range from zero up to a limiting value ($I_{\lim}$). The possible stationary states will be determined without an analysis of their stability and the ways of realization.

Consider a homogeneous transport tube with a thin annular electron beam (Fig. 1) injected from the left. The tube occurs at an electrostatic potential of the anode and is exposed to a strong magnetic field with the strength vector **H** parallel to the system axis.

First, it will be shown that this system, apart from the trivial case of a homogeneous beam transport via the tube, admits the states with the VC. Assuming that an azimuth-symmetric VC is formed in a certain plane B (z = const), let us determine the current behind the VC in a stationary state of the beam. Let us select a volume (with the boundary depicted by dashed line in Fig. 1) such that the field and beam parameters on the left and right boundaries can be considered as independent of the coordinate z. The law of energy conservation readily yields expressions relating the beam current to the electrostatic potential φ_b of the right and left boundaries of the volume under consideration:

$$I_1 = \frac{I_0}{2\ln(R_a/R_b)}\frac{(\Gamma-\gamma_1)\sqrt{\gamma_1^2-1}}{\gamma_1}, \qquad (1)$$

$$I_2 + I_3 = \frac{I_0}{2\ln(R_a/R_b)}\frac{(\Gamma-\gamma_2)\sqrt{\gamma_2^2-1}}{\gamma_2}, \qquad (2)$$

where $I_0 = mc^3/e$, $\Gamma = 1 + eU/mc^2$; $\gamma = 1 + e\varphi_b/mc^2$, U is the electrostatic (anode) potential of the tube, m is the electron mass, e is the electron charge, and c is the speed of light in vacuum.

Denoting the coefficient of beam reflection from the VC by $\alpha = I_3/I_2$ and taking into account that $I_1 = I_2 - I_3$, we conclude that $0 \le \alpha \le 1$ and obtain the relation

$$I_2 + I_3 = I_1\frac{(1+\alpha)}{(1-\alpha)}. \qquad (3)$$

Finally, Eqs. (1)–(3) yield

$$\frac{(1-\alpha)}{(1+\alpha)}\frac{(\Gamma-\gamma_2)\sqrt{\gamma_2^2-1}}{\gamma_2} = \frac{(\Gamma-\gamma_1)\sqrt{\gamma_1^2-1}}{\gamma_1}. \qquad (4)$$

In order to obtain an additional relation between γ_1 and γ_2, let us use the law of conservation of the z components of the field and particle momenta in the volume selected. Since we consider the stationary states, the z components of the field and particle momentum in this volume are constant and, hence, the total flux of these z components through the boundaries is zero. Quite simple calculations using the Maxwell stress tensor [4] lead to the relation

$$(\Gamma-\gamma_1)^2 + \frac{2(\Gamma-\gamma_1)(\gamma_1^2-1)}{\gamma_1} = (\Gamma-\gamma_2)^2 + \frac{2(\Gamma-\gamma_2)(\gamma_2^2-1)}{\gamma_2}, \qquad (5)$$

which follows from the law of conservation of the z component of momentum in the system under study.

1063-7850/03/2908-0666$24.00 © 2003 MAIK "Nauka/Interperiodica"

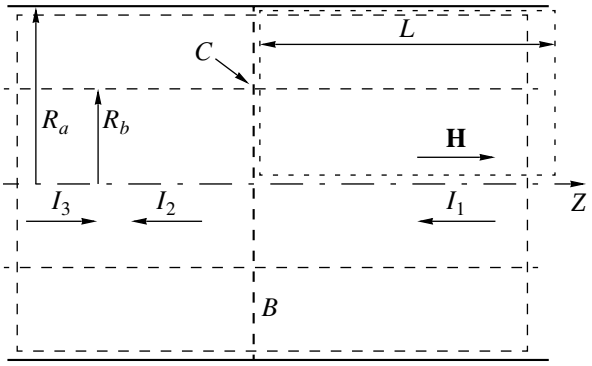

Fig. 1. The geometry of a homogeneous transport tube with a thin annular electron beam: R_a, the tube radius; R_b, the beam radius; I_1, I_2, I_3, the transmitted current, the injection current, and the current of electrons reflected from the VC, respectively. Dashed contour shows the calculation region. Point C indicates the position of an fictitious cathode in plane B.

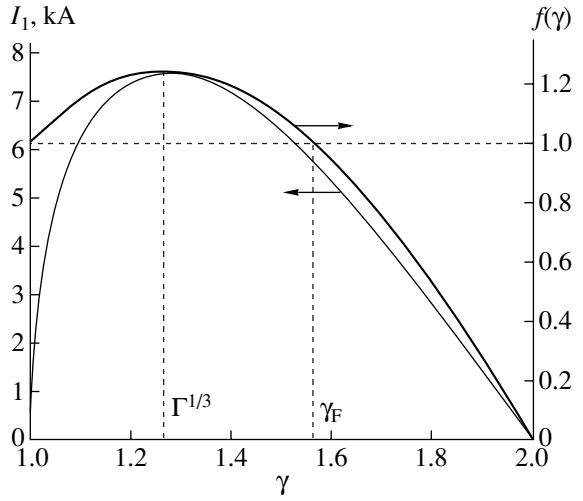

Fig. 2. Plots of the transmitted current I_1 and the function f versus the relativistic factor γ (for $\Gamma = 2$ and $2\ln(R_a/R_b) = 1$).

Introducing the function

$$f(\gamma) = (\Gamma - \gamma)^2 + \frac{2(\Gamma - \gamma)(\gamma^2 - 1)}{\gamma}, \qquad (6)$$

we can rewrite relation (5) as

$$f(\gamma_1) = f(\gamma_2). \qquad (7)$$

Besides the trivial solution $\gamma_1 = \gamma_2$, this equation has solutions such that $\gamma_1 \neq \gamma_2$. Indeed, the function f has a maximum at $\gamma = \Gamma^{1/3}$ (Fig. 2) where $f_{max} = (\Gamma^{2/3} - 1)^2(\Gamma^{2/3} + 2)$, while in the interval of $(\Gamma - 1)^2 \le f < f_{max}$, the relativistic factor γ has two real values. In particular, for $f = (\Gamma - 1)^2$, $\gamma_1 = 1$ and $\gamma_2 = \gamma_F = -0.5 + \sqrt{2\Gamma + 0.25}$, where γ_F is the relativistic factor for a beam with the so-called Fedosov current I_F obtained for a thin electron beam in a coaxial diode with magnetic insulation [5].

Current (1) reaches a maximum (I_{lim}) at $\gamma_1 = \Gamma^{1/3}$, as can be seen from the plot in Fig. 2. For equation (4) to be satisfied, it is necessary that γ_1 corresponds to the left branch of the current characteristic of a thin annular electron beam in a tube (Fig. 2). This implies $0 \le \alpha \le 1$, which corresponds to the physical meaning of the reflection coefficient. Such states correspond to a "squeezed" state of the beam considered in [6].

Figure 3 shows a plot of $I_1\ln(R_a/R_b)$ versus α for $\Gamma = 2$, from which it is seen that the beam current behind the VC in a homogeneous drift tube can take values in the interval from zero up to I_{lim}. Since the current I_1 is a single-valued function of the reflection coefficient α, the forward (I_2) and reflected (I_3) currents are also uniquely determined for each I_1. Thus, the beam current behind the VC uniquely determines the state of the system under consideration.

For $\alpha = 0$, all the injected current passes through the VC without reflection ($I_3 = 0$) and acquires the limiting value

$$I_1 = I_2 = I_{lim} = \frac{I_0}{2\ln(R_a/R_b)}(\Gamma^{2/3} - 1)^{3/2}. \qquad (8)$$

Thus, no current jump takes place when the VC is formed in a homogeneous drift tube. For $\alpha = 1$, all current is reflected from the VC so that $I_2 = I_3$:

$$I_2 = I_3 = \frac{I_F}{2} = \frac{I_0}{4\ln(R_a/R_b)}\frac{(\Gamma - \gamma_F)\sqrt{\gamma_F^2 - 1}}{\gamma_F}. \qquad (9)$$

A solution to the problem of determining currents in a coaxial diode with magnetic insulation, obtained using the condition of conservation of the z component of momentum [5], gave the relativistic factor $\gamma = \gamma_F$ (under

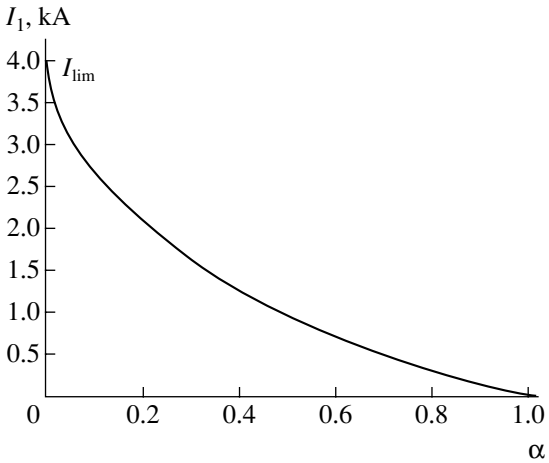

Fig. 3. A plot of the transmitted current I_1 versus the reflection coefficient α (for $\Gamma = 2$ and $2\ln(R_a/R_b) = 1$).

the natural assumption that the electron flux is unidirectional and $I = I_F$). In the general case, the current in the system with a given γ_F can take any value in the interval $-I_F \le I \le +I_F$, since the flux of the z component of momentum for both the field and particles is independent of the velocity sign. If all electrons are reflected from the VC ($\alpha = 1$), the current passing through the tube is zero ($I_1 = 0$). This implies that the beam in the right-hand part has a stationary charge density equal to that at the cathode of a coaxial diode with magnetic insulation, while the beam in the left-hand part comprises two opposite components (propagating to the right and left) carrying equal currents $I_F/2$.

In order to verify the above theoretical results, we have simulated the electron beam transport in a drift tube under specially selected boundary conditions at an fictitious cathode by means of the electromagnetic code KARAT [7]. Since it is impossible to obtain a VC by calculating the electron beam transport in a smooth drift tube, the numerical calculation was performed for a system with an fictitious cathode C placed at the minimum of the beam potential (Fig. 1, plane B). The conditions set on this cathode (i.e., the potential φ_C and its derivative $\partial\varphi/\partial\mathbf{n}$ along the normal) were equivalent to those at the point on minimum potential of the beam. The geometry of the calculation region is presented in Fig. 1.

The electron beam was emitted from the fictitious cathode C having the shape of a semitoroid (a semicircle in Fig. 1) with a large radius of $R = R_b$ and a small radius of $R_k = 0.0025$ cm, placed inside a transport tube with the radius $R_a = 1$ cm. The electrostatic potential of the anode tube was $U = 511$ kV. The calculation region occurred in a homogeneous guiding magnetic field with a strength of $H = 500$ kOe. The electrostatic potential of the cathode φ_C was varied from zero to a maximum value of $\varphi_{lim} \approx 133$ kV (which corresponded to the potential of a homogeneous beam with the limiting current I_{lim} in the same transport tube). The length of the beam transport region was $L = 5$ cm. The energy of electrons emitted from cathode C corresponded to the cathode potential, so that the electron velocity was determined as $V_C = c(\gamma_C^2 - 1)^{1/2}/\gamma_C$. This corresponds to the zero velocity of electrons on the real cathode situated far to the left from plane B.

Conditions on the left, right, and bottom boundaries of the calculation region were set as the Neumann boundary condition of the second kind: $\partial\varphi/\partial\mathbf{n} = 0$. This is related to the fact that the bottom boundary coincides with the symmetry axis and the right boundary occurs in the regular transport region, where the potential is independent of the coordinate z. On the left boundary, the condition $\partial\varphi/\partial\mathbf{n} = 0$ reflects a symmetric state of the beam relative to plane B: for $\varphi_C = 0$, the fictitious cathode models the VC with $\alpha = 0$ and for $\varphi_C \neq 0$, it corresponds to the potential minimum. Since the longitudinal electric field component at the potential minimum is $E_z = 0$, cathode C has unlimited emissivity. In our calculations, the emission current was increased until the electric field strength on the cathode became zero.

The model calculations were performed for $\varphi_C = 0$, 30, 60, and 133 kV. In all cases, the current acquired the limiting value $I_{lim} \approx 5.6$ kA. These results confirm that a beam with I_{lim} can occur in a stationary state with the VC ($\alpha = 0$) in plane B. In addition, it was demonstrated that a beam with I_{lim} can exist for any potential sag (from 0 to φ corresponding to $\gamma = \Gamma^{1/3}$) in plane B.

As was noted above, the case of $\alpha = 1$ corresponds to the solution for a coaxial diode with magnetic insulation [5] that was also verified by numerical calculations. Since the existence of the VC in the limiting cases ($\alpha = 0$ and 1) is confirmed by the numerical results, it is obvious that intermediate states with the VC for $0 < \alpha < 1$ exist as well.

Thus, it is established for the simple system considered above that the beam current behind the VC, the injection current, and the current of electrons reflected from the VC in any stationary state are uniquely related to each other, taking values within the intervals $0 \le I_1 \le I_{lim}$, $I_F/2 \le I_2 \le I_{lim}$, and $0 \le I_3 \le I_F/2$, respectively, where I_F is the Fedosov current.

REFERENCES

1. S. A. Kitsanov, A. I. Klimov, S. D. Korovin, *et al.*, IEEE Trans. Plasma Sci. **30**, 274 (2002).
2. A. E. Dubinov and I. E. Efimova, Zh. Tekh. Fiz. **71** (6), 80 (2001) [Tech. Phys. **46**, 723 (2001)].
3. N. F. Kovalev, Zh. Tekh. Fiz. **72** (7), 113 (2002) [Tech. Phys. **47**, 906 (2002)].
4. L. D. Landau and E. M. Lifshitz, *Course of Theoretical Physics*, Vol. 2: *The Classical Theory of Fields* (Nauka, Moscow, 1988; Pergamon, Oxford, 1975).
5. A. I. Fedosov, E. A. Litvinov, S. Ya. Belomyttsev, and S. P. Bugaev, Izv. Vyssh. Uchebn. Zaved. Fiz., No. 10, 134 (1977).
6. A. M. Ignatov and V. P. Tarakanov, Phys. Plasmas **1**, 741 (1994).
7. V. P. Tarakanov, *User's Manual for Code Karat* (BRA, Springfield, 1992).

Translated by P. Pozdeev

Technical Physics Letters, Vol. 29, No. 8, 2003, pp. 669–671. Translated from Pis'ma v Zhurnal Tekhnicheskoĭ Fiziki, Vol. 29, No. 16, 2003, pp. 23–28.

PETN Detonation Initiated by a High-Power Electron Beam

V. I. Korepanov*, V. M. Lisitsyn, V. I. Oleshko, and V. P. Tsypilev

Tomsk Polytechnical Institute, Tomsk, Russia

** e-mail: korepan@ephd.tpu.ru*

Received February 25, 2003

Abstract—We have studied for the first time the physicochemical processes developed in pentaerythritol tetranitrate (PETN) under the action of a pulsed electron beam in a broad range of the beam power densities. Data on the pulsed cathodoluminescence spectrum and kinetics, explosive optical emission kinetics, and thresholds of the mechanical fracture and explosive decomposition of PETN are presented. © *2003 MAIK "Nauka/Interperiodica".*

Pulsed high-current electron beams of nanosecond duration in combination with time-resolved optical pulse spectrometry are widely used for studying processes in solids and monitoring the properties of various solids including explosives [1, 2]. At present, a large volume of experimental data has been gained about the physical processes in initiating explosives developed under the action of pulsed electron beams. To our knowledge, no such investigations were reported for the secondary explosives including pentaerythritol tetranitrate (PETN).

As is known, laser pulses do not produce detonation of PETN even at the maximum possible pulse intensities, because the chemical reaction development is hindered by the evaporation and expansion of the laser-sputtered substance from the excitation zone [3]. The knowledge about kinetic processes is important in elucidating the mechanism of initiation of secondary explosives. In this context, investigations of the possibility and conditions of using high-current electron beams for the initiation of such explosives can also provide a valuable information.

Here we report the results of an original investigation of the kinetics of physicochemical processes developed in PETN under the action of a pulsed electron beam with a power density P in the range from 1×10^6 to 5×10^9 W/cm^2. The excitation source was a high-current electron accelerator producing electron pulses with an average electron energy of 250 keV and a full width at half maximum (FWHM) of ~25 ns. The electron beam pulse power density P was controlled by changing the vacuum diode geometry [4] and the distance from the target to the accelerator anode. Samples in the form of disks with a diameter of 4 mm and a thickness of 1.8 mm were prepared from a disperse PETN powder with a surface area of $S = 6000$ cm^2/g by pressing at a load of 10^9 Pa. The samples were excited by the electron beam at a temperature of $T = 300$ K in a vacuum chamber with a residual gas pressure of 10^{-2} Pa. The spectrum and kinetics of cathodoluminescence (CL) from PETN were studied using an optical pulse spectrometer with a time resolution of ~10 ns and a spectral resolution of ~0.008 eV.

The CL pulses were measured at an electron excitation power density not exceeding the mechanical fracture threshold of PETN. Figure 1 shows a typical emission spectrum of PETN measured for $P \sim 3 \times 10^6$ W/cm^2 at a moment of maximum CL intensity and corrected for the spectral sensitivity of the optical tract. As can be seen, the spectrum is complicated, representing a superposition of at least three emission bands. The time of emission decay in the entire spectral range did not exceed the electron pulse duration.

Upon excitation at a higher power density level, $P \geq 5 \times 10^6$ W/cm^2, the PETN sample surface was damaged by the electron beam. The action of multiply repeated electron pulses resulted in the formation of a crater with

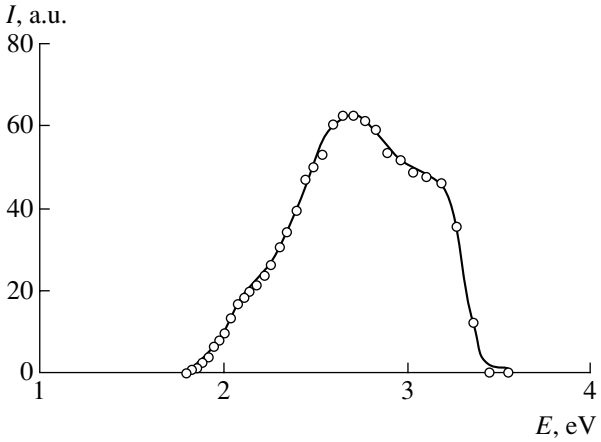

Fig. 1. The spectrum of pulsed room-temperature cathodoluminescence from PETN.

1063-7850/03/2908-0669$24.00

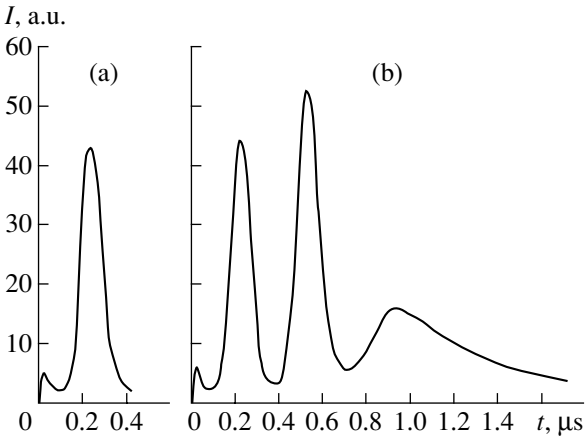

Fig. 2. Typical oscillograms showing kinetics of the optical emission intensity from an electron-beam-initiated explosion of a PETN sample, measured with (a) freely expanding explosion products and (b) in the presence of two obstacles.

a diameter equal to that of the electron beam. The crater increased in depth and acquired a cone shape with increasing power density and the number of pulses. It was established that this mechanical damage of the samples was not related to the chemical decomposition of PETN. This conclusion was confirmed by the absence of effects (optical and acoustic signals and a sharp increase in the pressure) characteristic of the explosive decomposition, by the lack of any traces of fusion and evaporation on the crater surface at an electron pulse power density of up to $P \sim 1 \times 10^8$ W/cm^2, and by proximity of the PETN fracture threshold to those of other (inert) materials [5].

The excitation of PETN samples by the electron beam at a power density of $P > 4 \times 10^9$ W/cm^2 (pulse energy ~1 J) led to detonation of the explosive. Such a high power density was achieved in the regime of self-focusing of the electron beam. The initiation threshold was experimentally determined from data on the formation of erosion spots on the surface of metals with different sublimation temperatures and calculated using the formulas presented in [6]. According to our estimates, the volume energy density at the PETN initiation site (determined for $\rho = 1.5$ g/cm^3 and $c = 1.67$ J/(g K)) amounts to ~2200 J/cm^3, the temperature in the near-surface region reaches ~1100 K, and the shock wave amplitude is ~$(5–7) \times 10^8$ Pa. Thus, the temperature and pressure at the detonation site in PETN initiated by the electron beam are comparable in the order of magnitude with analogous values observed for the other means of excitation [7]. These estimates are evidence for a thermal mechanism of the electron beam initiation of PETN.

In order to study the optical emission and expansion kinetics of the PETN explosion products, we used the following experimental scheme. A PETN sample was mounted on the anode provided with a 1.5 mm hole for the electron beam passage. An image of the sample surface and the adjacent region of expansion of the explosive decomposition products was projected by a lens (with double magnification) onto the exit slit of an MDR-23 grating monochromator. The optical emission was detected at a wavelength of 600 nm using a FEU-118 photomultiplier and measured with an S8-14 oscillograph. The velocity of expansion of the explosion products was determined using obstacles (1-mm-diam wires) placed at a distance of 2 and 4 mm from the rear surface (opposite to that exposed to the beam).

Figures 2a and 2b show typical oscillograms of the optical emission intensity from a PETN sample measured with a freely expanding plasma jet and in the presence of two obstacles, respectively. The first peak reflects the bremsstrahlung emission pulse of the electron accelerator and serves as a reference mark for the sample exposure onset. The second peak represents the optical emission pulse delayed by ~100 ns relative to the initial moment. Both the duration (FWHM ~ 120 ns) and amplitude of this peak vary by no more than 15% under the same sample excitation conditions. Using the duration of this pulse and the PETN sample size, we have estimated the average rate of the chemical decomposition of PETN. Under the experiential conditions studied, the combustion velocity was about 1×10^4 m/s. However, this is only a rough estimate, since more exact calculation requires data on the depth of the energy deposition zone that can hardly be determined in experiment.

The high estimated rate of the chemical decomposition of PETN is indicative of a rapid detonation development in the explosive. The initial stages of the chemical reaction (slow combustion and low- rate detonation with a velocity of 1×10^3 m/s) were not revealed in the experimental kinetic curves. This is probably related to the fact that the time of these processes is comparable with the time of substance ejection from the energy deposition zone. The results of preliminary experiments (involving several measurements at various wavelengths) showed that the explosive optical emission spectrum is predominantly continuous.

The third and fourth emission peaks in Fig. 2b correspond to the impact of the plasma jet (formed due to the explosive decomposition of PETN) upon the obstacles, after which a part of the kinetic energy of the plasma converts into optical emission. The velocity of expansion of the explosive decomposition products, calculated from the emission intensity oscillograms, amounted to 5×10^3 m/s.

Thus, pulsed electron beams, in contrast to laser radiation pulses, are capable of initiating an explosive decomposition process on the open surface of PETN. The detonation process development is most probably explained as follows. The electron beam energy is virtually completely spent to heat the target volume with a diameter equal to that of the beam and a depth equal to the electron mean free path. As the pulse power density reaches a level sufficient to evaporate PETN, a shock

wave is generated with an amplitude rapidly increasing with the electron beam power. When the shock wave amplitude reaches a critical pressure level, PETN exhibits detonation. As a result of the explosion, a compact zone of low-temperature plasma is formed from the sample that begins to expand at a supersonic velocity. The possibility of reliably initiating the detonation of PETN, without suppressing the expansion of substance from the excitation zone, is probably determined by a volume character of the electron beam energy deposition in the target, which results in the formation of a shock wave with the critical amplitude at a much lower energy as compared to that required in the case of a laser action.

REFERENCES

1. V. I. Korepanov, V. M. Lisitsyn, and V. I. Oleshko, Izv. Vyssh. Uchebn. Zaved. Fiz. **43** (3), 22 (2000).
2. Yu. A. Zakharov, É. D. Aluker, B. P. Aduev, *et al.*, *Pre-Explosion Phenomena in Heavy Metal Azides* (Khimmash, Moscow, 2002).
3. A. A. Brish, I. A. Galleev, and B. N. Zaĭtsev, Fiz. Goreniya Vzryva **2** (3), 132 (1966).
4. V. I. Korepanov, V. M. Lisitsyn, and V. I. Oleshko, RF Patent No. 2157988 (2000).
5. V. I. Oleshko and V. F. Shtan'ko, Fiz. Tverd. Tela (Leningrad) **29**, 320 (1987) [Sov. Phys. Solid State **29**, 182 (1987)].
6. G. A. Mesyats and D. I. Proskurovskiĭ, *Pulse Electric Discharge in Vacuum* (Nauka, Novosibirsk, 1984).
7. V. I. Tarzhanov, A. D. Zinchenko, V. I. Sdobnov, *et al.*, Fiz. Goreniya Vzryva **32** (4), 113 (1996).

Translated by P. Pozdeev

Technical Physics Letters, Vol. 29, No. 8, 2003, pp. 672–675. Translated from Pis'ma v Zhurnal Tekhnicheskoĭ Fiziki, Vol. 29, No. 16, 2003, pp. 29–38.

Optical Properties of a Polyimide–Fullerene System in the Near Infrared Range (λ = 1047 nm)

N. V. Kamanina[a,*], M. O. Iskandarov[b], and A. A. Nikitichev[b]

[a] *Vavilov Optical Institute, State Scientific Center of the Russian Federation, St. Petersburg, Russia*

[b] *Institute of Laser Physics, St. Petersburg, Russia*

* *e-mail: kamanin@ffm.ioffe.rssi.ru*

Received February 18, 2003

Abstract—The optical properties of polyimide sensitized with fullerenes C_{60} and C_{70} have been studied for the first time in the near infrared range. It is shown that materials based on the polyimide–fullerene system can be used for limitation of the laser radiation power in this spectral range. © *2003 MAIK "Nauka/Interperiodica".*

Introduction. Optimization of the characteristics of materials applicable in various fields of science and technology is a difficult task. However, there is a class of substances which, being introduced in a given matrix, significantly modify the spectrum, photoconductivity, and nonlinear optical properties of the medium. This class includes, in particular, fullerenes. It was shown [1] that the introduction of fullerene C_{60} into poly[(disilanylene)oligophenylene] leads to a significant increase in the photoconductivity and gives rise to luminescence quenching. The optical absorption spectra of fullerene-containing polysilanes measured in a wavelength range from 200 to 500 nm showed an increase in the intensity of absorption at 250–275 nm in samples containing 5–10 mol % C_{60}.

An increase in the photoconductivity was also observed for poly(vinyl carbazole) sensitized with fullerenes C_{60} and C_{70} [2]. Investigation of the photoinduced charge transfer in an analogous system of C_{60}–poly(N-vinylcarbazole) [3] showed that a broad absorption band in the range from 400 to 700 nm appears upon the introduction of 0.7 mol % C_{60}. An increase in photoconductivity of the fullerene-containing poly(vinyl carbazole) was related to the formation of a new complex between C_{60} molecules and carbazole fragments of the organic matrix. Analogous structures were successfully used for the recording of holographic gratings [4]. This result not only showed prospects for the application of carbazole-containing matrices with fullerenes as unique photosensitive conducting media, but also pointed out to their possible use as materials for nonlinear optics.

Recently, the unique optical and photoelectric properties of water-soluble aromatic polyimides, determined by the possibility of exciting the π electron system in these materials, allowed the fullerenes C_{60} and C_{70} to be used as dopants effectively controlling the donor–acceptor interaction, leading to the effects of optical power limitation and light-induced variation of the refractive index in the visible and near infrared (NIR) spectral intervals [5, 6].

Thus, it has been established that there is a reliable possibility of modifying the optical properties of materials by doping with fullerenes. However, until recently, investigations of the optical properties of such organic structures in the IR range were very seldom and there is a need to study this spectral range more thoroughly. Ruani *et al.* [7] observed nonlinear transmission of nanosecond laser radiation pulses at λ = 1064 nm in a zinc-containing phthalocyanine (Zn-Pc) system sensitized with fullerene C_{60}. It was found that this system is virtually transparent (transmitting 75–80% of the incident radiation) at low energy densities, but attenuates the laser beam by half at elevated incident energy levels. The results were explained [7] by the process of complex formation in this system with pronounced donor– acceptor interactions. Riehl and Fougeanet [8] studied the properties of carbon-containing suspensions in water and CS_2 and observed an eightfold attenuation of nanosecond laser radiation pulses at λ = 1064 nm. It was shown that the nonlinear absorption is related to complex thermodynamic processes in the liquid phase heated by laser pulses at an incident beam energy density within 10–100 J/cm^2.

Lee *et al.* [9] studied the manifestations of nonlinear absorption in thin films of C_{60}–poly(3-octylthiophene), a system featuring intermolecular interaction with the formation of charge transfer complexes, and determined the light-induced variation of the refractive index in a wavelength region of 1100–1130 nm. These results showed prospects in the search for nonlinear absorption of the C_{60}–poly(3-octylthiophene) films in

1063-7850/03/2908-0672$24.00 © 2003 MAIK "Nauka/Interperiodica"

the millimeter wavelength range. Konarev *et al.* [10] detected charge transfer complexes between the molecules of fullerenes (C_{60} and C_{70}) and a group of organic donors responsible for the absorption at λ = 900 nm.

Recently, the two-step character of the optical power limitation at λ = 1315 nm by means of the double spectral control was demonstrated [11] for the system of π-conjugated polyimide molecules and fullerene C_{70}. The third harmonic generation in an analogous system was studied [12] for picosecond pulses of a Nd:YAG laser with the first harmonic at λ = 1064 nm.

The present work was aimed at studying the nonlinear optical properties of a nanocomposite material based on the polyimide–fullerene system and evaluating the possibility of using these fullerene-containing nanocomposites for the optical power limitation in the NIR range. Here we report the first results on the laser radiation intensity attenuation in this system at λ = 1047 nm and present comparative data on the optical power limitation in the visible spectral range for analogous systems.

Experimental conditions and results. The experiments were performed with films of a photosensitive grade 6B polyimide (PI-6B) prepared from 3–5% solutions in tetrachloroethane. The films were sensitized by adding fullerenes C_{60} and/or C_{70}. Since the use of anisotropic C_{70} molecules led to more pronounced manifestations of the nonlinear optical properties, all subsequent experiments were performed with the samples prepared using this fullerene type. The films were applied by centrifuging on quartz substrates with preliminarily deposited indium–tin electrodes, followed by drying for 12–20 h. The sample film thicknesses varied within 2–5 μm. The fullerene content was varied in the interval from 0.1 to 0.5 wt %.

The optical absorption spectra were measured on a Perkin-Elmer Lambda-9 spectrophotometer in a wavelength range from 200 to 3000 nm. The attenuation of laser radiation in the fullerene-containing media described above was studied using a single-pass scheme [13]. The radiation source was a pulsed Nd:$YLiF_4$ laser operating at a wavelength of 1047 nm and a pulse duration of 8 ns. The laser spot diameter on a sample was ~2 mm. The laser beam energy incident onto and transmitted through the sample was directly measured using laser radiation detectors.

Figure 1 shows a typical IR absorption spectrum of a polyimide–C_{70} film. As can be seen, the transmission of this polyimide based system in the range studied (in particular, at λ = 1047 nm) amounts to 79–85%. Figure 2 shows the absorption spectra of pure fullerene C_{70} solutions in tetrachloroethane and toluene.

Figure 3 presents the results of investigation of the laser radiation power limitation at λ = 1047 nm in the

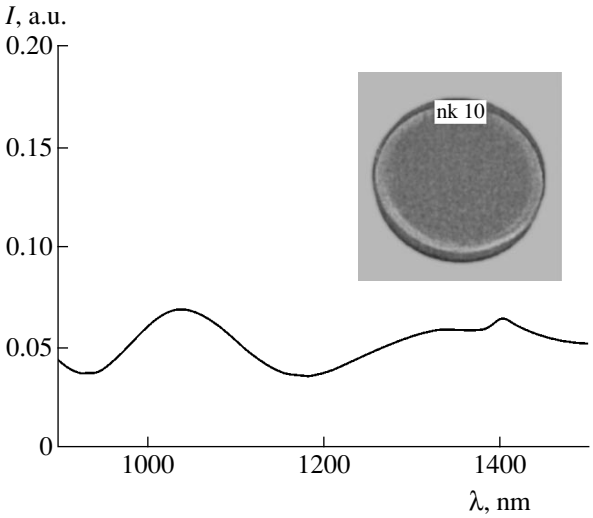

Fig. 1. The IR absorption spectrum of a polyimide–fullerene C_{70} system (*I* is the optical density). The inset shows a sample of PI-6B polyimide sensitized with 0.2 wt % C_{70}.

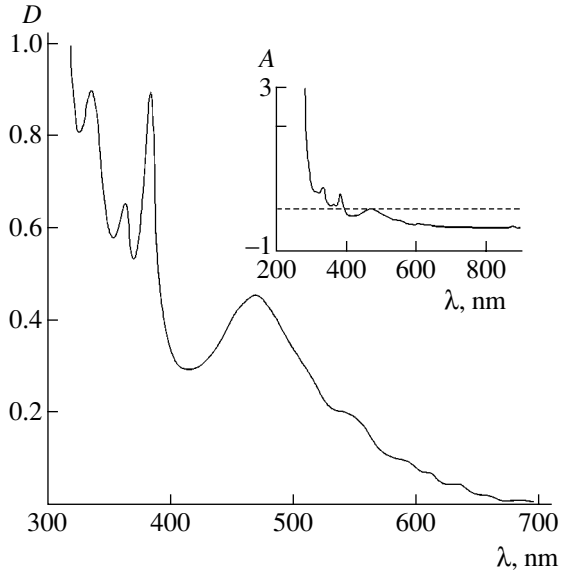

Fig. 2. The optical absorption spectrum of fullerene C_{70} in tetrachloroethane (*D* is the optical density). The inset shows the analogous spectrum in toluene (*A* is the logarithmic absorption).

polyimide–C_{70} system. The data are presented in the form of plots of the output radiation energy density (W_{out}) versus the input energy density (W_{in}) for three polyimide films containing 0.5, 0.2, or 0.1 wt % C_{70} (Fig. 3, curves *1–3*, respectively). Taking into account that the linear transmission of the system studied was 79–85% and the experimental error did not exceed 5–7%, these data provide reliable evidence of the nonlinear power limitation at 1047 nm in the polyimide–fullerene system studied. A summary of the results of

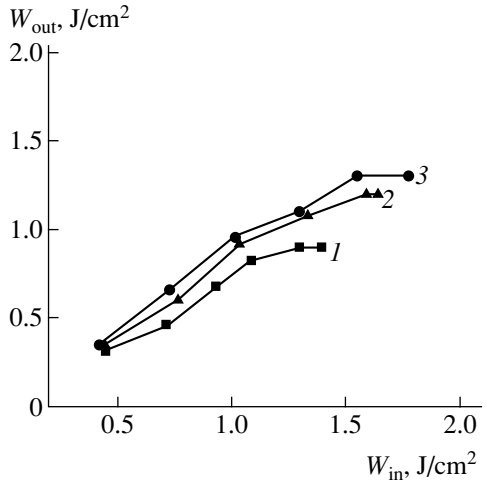

Fig. 3. Plots of the output radiation energy density (W_{out}) versus input energy density (W_{in}) at λ = 1047 nm for polyimide 6B sensitized with (*1*) 0.5, (*2*) 0.2, and (*3*) 0.2 wt % C_{70}.

this investigation, in comparison to the data available in the literature [14–18] on the optical power limitation in solid state systems, solutions, and suspensions irradiated by micro-, nano-, and picosecond pulses of laser radiation in the IR spectral range, is given in the table (including data for the structures sensitized with fullerene C_{60}).

Thus, the polyimide–fullerene C_{70} system exhibits the effect of nonlinear limitation of the IR radiation power in the region of λ = 1047 nm. This behavior is probably explained by the following factors. First, the fundamental absorption of polyimide systems occurring in the region of 270–275 nm neither excludes manifestations of the multiphoton absorption in the IR range nor contradicts the features of the IR spectrum of the polyimide–fullerene C_{70} system (Fig. 1). Second, the resonance absorption of pure fullerene C_{70} takes place at 430–520 nm (Fig. 2), which is also consistent with two-photon absorption at 1047 nm. Third, the optical limitation threshold observed for the polyimide–fullerene system at 0.6–0.7 J/cm^2 implies the light-induced change in the refractive index related to the high-frequency Kerr effect. Indeed, it was recently demonstrated [5, 19] that changes in the refractive index for the incident radiation power densities employed and nanosecond pulse durations amount

Comparative data on the optical power limitation in the IR spectral range

System	Initial transmission, %	Wavelength, nm	Pulse duration, ns	Limitation threshold, J/cm^2	Fracture threshold, J/cm^2	Possible mechanisms of limitation	Ref.
Silver halide based composite with metallic silver nanoparticles		3800–4200	250	0.005–0.025		Simultaneous shift and increase in plasmon resonance absorption; thermoinduced change in dielectric permittivity of composite components	[14]
2-(*p*-Prolinol)-5-nitropyridine–C_{60}	65–70	2940	500 μs	0.9–1	≥1.5	Light-induced complex formation	[15]
Polyimide–C_{70}	~80	1315	50	0.08–0.1	~2	Light-induced complex formation; double spectral control effect	[6, 11]
Zn-Pc–C_{60}	75–80	1064	nanosecond range			Light-induced complex formation	[7]
Carbon black suspensions in water and CS_2	~80	1064	10	0.12–0.7		Thermodynamic processes in suspensions heated by laser pulses of high energy density (≥10 J/cm^2)	[8]
Carbon nanotube suspensions in water and chloroform	≥90	1064	6	0.15–0.35		Nonlinear scattering; sublimation of carbon nanoparticles	[16]
C_{60} solution	~85	1064	35 ps	~3		Two-photon absorption	[17]
Polyimide–C_{70}	~79–85	1047	8	0.6–0.7	~2.5–3	Two-photon absorption of C_{70}; multiphoton absorption of polyimide matrix; refractive index variation due to high-frequency Kerr effect	This study
C_{60} solution	84	710–740	10	2		Inverse saturation absorption	[18]

to ~10^{-3}, which can also contribute to the power attenuation due to diffraction losses.

Conclusion. (i) We have studied the optical properties of a conjugated polyimide–fullerene system in the region of $\lambda = 1047$ nm for assessing the prospects of creating nonlinear attenuators functioning in the NIR spectral range.

(ii) The experimental data can be interpreted considering the possible contributions of the multiphoton absorption, two-photon processes, and high-frequency Kerr effect to the nonlinear optical properties of the system studied, which can account for the optical power limitation effect at the given wavelength.

(iii) The first experimental results can provide the basis for creating nonlinear optical attenuators and space–time modulators operating in the NIR range, based on fullerene-sensitized polyimides.

Acknowledgments. The authors are grateful to V.I. Berendyaev (Karpov Institute of Physical Chemistry, Moscow) for his help in the work.

This study was supported in part by the Russian Foundation for Basic Research (project nos. 00-15-99067 and 01-03-33162).

REFERENCES

1. K. Hosoda, R. Tada, M. Ishikawa, and K. Yoshino, Jpn. J. Appl. Phys., Part 2 **36** (3B), L372 (1997).
2. Y. Wang, N. Herron, and J. Casper, Mater. Sci. Eng., B **19**, 61 (1993).
3. A. Itaya, I. Sizzuki, Y. Tsuboi, and H. Miyasaaka, J. Phys. Chem. B **101**, 5118 (1997).
4. M. E. Orczyk, J. Zieba, and P. N. Prasad, Proc. SPIE **2025**, 298 (1993).
5. N. V. Kamanina, Synth. Met. **127**, 121 (2002).
6. N. V. Kamanina, I. V. Bagrov, I. M. Belousova, *et al.*, Opt. Commun. **194**, 367 (2001).
7. G. Ruani, M. Biscarini, M. Cavallini, *et al.*, in *Abstracts of the 2nd International Symposium on Optical Power Limiting, Venice (Italy), 2000*, p. 69.
8. D. Riehl and F. Fougeanet, Nonlinear Opt. **21**, 391 (1999).
9. K. Lee, E. K. Miller, N. S. Sariciftci, *et al.*, Phys. Rev. B **54**, 10525 (1996).
10. D. V. Konarev, Y. V. Zubavichus, Yu. L. Slovokhotov, *et al.*, Synth. Met. **92**, 1 (1998).
11. N. V. Kamanina, I. V. Bagrov, I. M. Belousova, and A. P. Zhevlakov, Opt. Spektrosk. **91**, 5 (2001) [Opt. Spectrosc. **91**, 1 (2001)].
12. R. A. Ganeev, A. I. Ryasnuansky, N. V. Kamanina, *et al.*, J. Opt. B: Quantum Semiclassical Opt. **3** (3), 88 (2001).
13. V. P. Belousov, I. M. Belousova, V. P. Budtov, *et al.*, Opt. Zh. **64** (12), 3 (1997).
14. I. V. Bagrov, A. P. Zhevlakov, O. P. Mikheeva, *et al.*, Pis'ma Zh. Tekh. Fiz. **28** (13), 40 (2002) [Tech. Phys. Lett. **28**, 552 (2002)].
15. N. V. Kamanina, M. O. Iskandarov, and A. A. Nikitichev, Pis'ma Zh. Tekh. Fiz. **29** (8), 62 (2003) [Tech. Phys. Lett. **29**, 337 (2003)].
16. L. Vivien, D. Riehl, P. Lancon, *et al.*, Nonlinear Opt. **27**, 395 (2001).
17. R. A. Ganeev, N. V. Kamanina, I. A. Kulagin, *et al.*, Kvantovaya Élektron. (Moscow) **32**, 781 (2002).
18. S. R. Mishra, H. S. Rawat, and S. C. Mehendale, Appl. Phys. Lett. **71**, 46 (1997).
19. N. V. Kamanina, Opt. Spektrosk. **90**, 960 (2001) [Opt. Spectrosc. **90**, 867 (2001)].

Translated by P. Pozdeev

Technical Physics Letters, Vol. 29, No. 8, 2003, pp. 676–678. Translated from Pis'ma v Zhurnal Tekhnicheskoĭ Fiziki, Vol. 29, No. 16, 2003, pp. 39–44.

Phenomenological Derivation of the Onsager Reciprocal Relations

M. M. Mamedov

Center of Physicomathematical Research, Turkmenian State University, Ashgabat, Turkmenia

e-mail: Nazarov@online.tm

Received January 17, 2003

Abstract—The Onsager reciprocal relation for a linear dissipative system with two fluxes is derived within the framework of a phenomenological approach using the property of nonnegative definiteness of the dissipative function. It is established that the Onsager relations are valid when the generalized fluxes are zero for nonzero generalized thermodynamic forces. In the general case, the Onsager reciprocal relations can be phenomenologically derived based on the theory of matrices and determinants or on the Prigogine principle of the entropy production minimum. *© 2003 MAIK "Nauka/Interperiodica".*

Introduction. In 1931, L. Onsager established a general relationship for the linear phenomenological equations of nonequilibrium thermodynamics, which are known as the Onsager reciprocal relations [1]. Although more than seventy years have passed since then, no phenomenological derivation of these relations has been found.

This Letter reports on the first successful attempt, whereby the Onsager reciprocal relations are derived for a linear dissipative system with two fluxes:

$$J_1 = \gamma_{11}X_1 + \gamma_{12}X_2, \quad \text{(I)}$$

$$J_2 = \gamma_{21}X_1 + \gamma_{22}X_2, \quad \text{(II)}$$

where γ_{ik} are the kinetic coefficients and X_1, X_2 are the generalized thermodynamic forces. The entropy production in this system is

$$\delta = J_1X_1 + J_2X_2 \quad \text{(III)}$$

or

$$\delta = \gamma_{11}X_1^2 + (\gamma_{12} + \gamma_{21})X_1X_2 + \gamma_{22}X_2^2. \quad \text{(IV)}$$

According to the second law of thermodynamics $\delta \geq 0$, whence

$$\gamma_{11} > 0; \quad \gamma_{22} > 0; \quad (\gamma_{12} + \gamma_{21})^2 \leq 4\gamma_{11}\gamma_{22}. \quad \text{(V)}$$

According to the Onsager theory, the coefficients in Eqs. (I) and (II) obey the relation

$$\gamma_{12} = \gamma_{21}, \quad \text{(VI)}$$

which must be valid for arbitrary J_1 and J_2 corresponding nonzero values of the generalized thermodynamic forces X_1 and X_2. However, finding the fluxes J_1 and J_2 corresponding to the minimum of the function $\delta(X_1, X_2)$,

$$J_1 = \pm\frac{1}{2}\sqrt{\frac{\gamma_{11}}{\gamma_{22}}}(\gamma_{21} - \gamma_{12})X_1, \quad \text{(VII)}$$

$$J_2 = \mp\frac{1}{2}\sqrt{\frac{\gamma_{22}}{\gamma_{11}}}(\gamma_{21} - \gamma_{12})X_2, \quad \text{(VIII)}$$

one has to conclude that the Onsager reciprocal relations are valid then and only then, when $J_1 = 0$ and $J_2 = 0$. Therefore, the Onsager reciprocal relations are not valid in the traditional sense.

Phenomenological theory. Thus, we consider a linear dissipative system described by the linear equations

$$J_1 = \gamma_{11}X_1 + \gamma_{12}X_2, \quad (1)$$

$$J_2 = \gamma_{21}X_1 + \gamma_{22}X_2 \quad (2)$$

for which the Onsager reciprocal relation is expressed as [2]

$$\gamma_{12} = \gamma_{21}, \quad (3)$$

where J_1 and J_2 are the generalized thermodynamic fluxes; γ_{ik} are the phenomenological kinetic coefficients; and X_1 and X_2 are the generalized thermodynamic forces.

The theory developed by Onsager [1] is general and does not specify particular mechanisms of transfer processes in the system studied. The main premises of the theory are as follows [2]: (i) the principle of microscopic reversibility (Onsager's principle); (ii) the equilibrium fluctuation theory; (iii) the postulate of a relationship between spontaneous fluctuations and irreversible processes (Onsager's hypothesis); and (iv) the linear phenomenological transfer equations.

1063-7850/03/2908-0676$24.00 © 2003 MAIK "Nauka/Interperiodica"

The Onsager reciprocal relations constitute a basis of the so-called classical linear nonequilibrium thermodynamics. Therefore, it is expedient to consider the question concerning the consistency and adequacy of this basis. There are various opinions in this respect, some of which are as follows [2].

The theory is based on the principle of microscopic reversibility, which was considered by Onsager as an important supplement to the first and second laws of thermodynamics. According to Denbigh [3], the Onsager principle is essentially of a molecular nature, and it might appear that this principle cannot serve as a basis for the new thermodynamics.

According to Tribus [4], no convincing procedure has been proposed that would show, proceeding from first principles, that the Onsager principle is always valid and universally applicable. Onsager gave arguments for the validity of this principle in some cases and the conclusions have been experimentally corroborated. However, no proof was proposed that would be as convincing as, for example, evidence of the laws of thermostatics. Therefore, the Onsager rules should be considered as empirical [4].

Petrov and Brankov [2] pointed out that the classical thermodynamics is subject to considerable criticism of the followers of rational thermodynamics, up to complete repudiation of the meaning and value of the Onsager reciprocal relations. On the other hand, some other researchers ascertain that these relations can be considered as an empirically established axiom, irrespective of the existence of derivation based on the principles of statistical mechanics.

Thus, there are various, even opposite, opinions concerning the validity of the Onsager reciprocal relations. In this situation, a phenomenological derivation of these relations is definitely of considerable importance. The possibility of such derivation was admitted by some researchers. Dyarmati [5] fully agreed with Truthdell in that "if the Onsager reciprocal relations are valid, there must be a possibility of purely phenomenological derivation."

Here, a variant of such derivation is proposed. For the sake of simplicity, a phenomenological analysis is applied to the case of a linear dissipative system with two fluxes.

As is known, the central place in the classical nonequilibrium thermodynamics belongs to an equation for the entropy production δ [6]:

$$\delta = J_1X_1 + J_2X_2 \geq 0 \tag{4}$$

or

$$\delta = \gamma_{11}X_1^2 + (\gamma_{12} + \gamma_{21})X_1X_2 + \gamma_{22}X_2^2 \geq 0. \tag{5}$$

In Eq. (4), J_i and X_i denote the scalar thermodynamic fluxes and forces, as well as the Cartesian components of both vector and tensor quantities describing the corresponding processes [2].

The aforementioned nonnegative definiteness of the quadratic form (5), following from the second law of thermodynamics, poses certain limitations on the coefficients γ_{ij} [6]:

$$\gamma_{11} > 0, \quad \gamma_{22} > 0, \quad (\gamma_{12} + \gamma_{21})^2 - 4\gamma_{11}\gamma_{22} \leq 0. \tag{6}$$

Adding the term $-4\gamma_{12}\gamma_{21}$ to both parts of the latter inequality, we obtain

$$(\gamma_{12} + \gamma_{21})^2 - 4\gamma_{11}\gamma_{22} - 4\gamma_{12}\gamma_{21} \leq -4\gamma_{12}\gamma_{21} \tag{7}$$

and, after transformations,

$$(\gamma_{12} - \gamma_{21})^2 \leq 4(\gamma_{11}\gamma_{22} - \gamma_{12}\gamma_{21}). \tag{8}$$

Let us consider relation (8) in various particular cases.

1. First, consider the equality

$$(\gamma_{12} - \gamma_{21})^2 = 4(\gamma_{11}\gamma_{22} - \gamma_{12}\gamma_{21}) \tag{9}$$

for $X_1 \neq 0$ and $X_2 \neq 0$. In this case, there are two possible variants.

(i) If

$$\gamma_{11}\gamma_{22} - \gamma_{12}\gamma_{21} = 0, \tag{10}$$

then

$$\gamma_{12} - \gamma_{21} = 0 \text{ or } \gamma_{12} = \gamma_{21}, \tag{11}$$

and vice versa. In this variant, relations (10) and (11) yield

$$\gamma_{11}\gamma_{22} - \gamma_{12}^2 = 0, \tag{12}$$

which ensures the conditions

$$J_1 = 0 \quad \text{and} \quad J_2 = 0, \tag{13}$$

provided that $X_1 \neq 0$ and $X_2 \neq 0$.

(ii) If

$$\gamma_{11}\gamma_{22} - \gamma_{12}\gamma_{21} \neq 0, \tag{14}$$

then

$$\gamma_{12} - \gamma_{21} \neq 0 \text{ or } \gamma_{12} \neq \gamma_{21}, \tag{15}$$

and vice versa. In this variant, relation (14) implies that the generalized thermodynamic fluxes are not equal to zero simultaneously.

2. Now consider the case of inequality

$$(\gamma_{12} - \gamma_{21})^2 < 4(\gamma_{11}\gamma_{22} - \gamma_{12}\gamma_{21}) \tag{16}$$

for $X_1 \neq 0$ and $X_2 \neq 0$. Let us rewrite this condition in the form of equality

$$(\gamma_{12} - \gamma_{21})^2 = 4\alpha(\gamma_{11}\gamma_{22} - \gamma_{12}\gamma_{21}), \tag{17}$$

by introducing a certain coefficient α, which falls within the interval

$$0 < \alpha < 1. \tag{18}$$

In the case of

$$\gamma_{11}\gamma_{22} - \gamma_{12}\gamma_{21} \neq 0, \tag{19}$$

we have

$$\gamma_{12} - \gamma_{21} \neq 0 \quad \text{or} \quad \gamma_{12} \neq \gamma_{21}, \tag{20}$$

and vice versa. Thus, relation (19) implies that both generalized thermodynamic fluxes are not equal to zero simultaneously.

Discussion. The above phenomenological derivation of the Onsager reciprocal relations shows that these relations are valid, but only for zero generalized thermodynamic fluxes rather than for arbitrary values (as has been believed since 1931). This is essentially a new scientific result.

In this context, the traditional statement concerning equality (3) of the cross coefficients in Eqs. (1) and (2) is no longer valid. It has to be replaced by the following statement: equality (3) of the cross coefficients in Eqs. (1) and (2) takes place, provided that all generalized thermodynamic fluxes are simultaneously equal to zero for nonzero thermodynamic forces.

Thus, the classical linear nonequilibrium thermodynamics (also referred to as Onsager's linear nonequilibrium thermodynamics) based on the Onsager reciprocal relations represents essentially the thermodynamics of a very particular case of the dissipative systems with zero generalized thermodynamic fluxes.

In conclusion, note that a phenomenological derivation of the Onsager reciprocal relations in the general case can be based on the theory of matrices and determinants or on the Prigogine principle of the entropy production minimum.

REFERENCES

1. L. Onsager, Phys. Rev. **37**, 405 (1931); Phys. Rev. **38**, 2265 (1931).
2. N. Pertrov and I. Brankov, *Modern Problems of Thermodynamics* (Mir, Moscow, 1986).
3. K. Denbigh, *Thermodynamics of the Steady State* (London, 1951; IL, Moscow, 1954).
4. M. Traibus, *Thermostatics and Thermodynamics* (London, 1967; Énergiya, Moscow, 1970).
5. I. Gyarmati, *Non-Equilibrium Thermodynamics* (Springer-Verlag, Berlin, 1970; Mir, Moscow, 1974).
6. S. R. de Groot and P. Mazur, *Nonequilibrium Thermodynamics* (North-Holland, Amsterdam, 1962; Mir, Moscow, 1964).

Translated by P. Pozdeev

Technical Physics Letters, Vol. 29, No. 8, 2003, pp. 679–682. Translated from Pis'ma v Zhurnal Tekhnicheskoĭ Fiziki, Vol. 29, No. 16, 2003, pp. 45–53.

Electron Beam Formation in Helium at Elevated Pressures

S. B. Alekseev[a,*], V. M. Orlovskiĭ[a], V. F. Tarasenko[a], A. N. Tkachev[b], and S. I. Yakovlenko[b,]**

[a] *Institute of High-Current Electronics, Siberian Division, Russian Academy of Sciences, Tomsk, Russia*
* *e-mail: vft@loi.hcei.tsc.ru*
[b] *Institute of General Physics, Russian Academy of Sciences, Moscow, 117924 Russia*
** *e-mail: syakov@kapella.gpi.ru*

Received December 6, 2002; in final form, January 3, 2003

Abstract—The formation of a beam of runaway electrons in a diode filled with helium at a pressure from 0.1 to 760 Torr was studied under conditions of a pulsed (≈4 ns) high (≈200 kV) voltage applied to the discharge gap. Both theoretical results and experimental data indicate that the electron beam is generated both at a large strength of the electric field, when the fraction of runaway electrons is large, and in a field of low strength, where intensive electron multiplication takes place. In the latter case, a high current can be obtained despite a small fraction of runaway electrons relative to their total number. The electron beams obtained in the helium-filled diode had a current amplitude of up to 140 A (corresponding to a current density above 10 A/cm^2) at an electron energy of ~150 keV. © *2003 MAIK "Nauka/Interperiodica".*

Introduction. Problems pertaining to the generation of X-ray and electron beams in gases at high pressures have been given much attention (see, e.g., [1–8] and references therein). However, electron beams with a high current density can be effectively generated only at relatively low gas pressures [5, 7, 8]. Although some papers reported on the obtaining of accelerated electron beams at pressures on the order of one atmosphere, either the beam currents (and current densities) were small [2, 3] or the beam was formed using additional pulses for the plasma generation [6].

The aim of our experimental and theoretical investigations was to assess the possibility of obtaining high-current electron beams in helium at elevated pressures.

Theoretical analysis and numerical simulation. In order to determine the conditions of electron runaway, we have theoretically analyzed and numerically simulated the process of electron multiplication in a discharge gap. The main results are as follows.

A certain fraction of electrons (~1%) exhibits runaway under the condition when an electron traveling a distance equal to the mean free path ($l = 1/\sigma_i N$) gains an energy $\varepsilon \equiv m_e v^2/2 = eEl$ on the order of the double ionization energy. Here, σ_i is the ionization cross section, N is the density of neutral atoms, v and m_e are the electron velocity and effective mass, respectively, and E is the electric field strength. Accordingly, a condition for the anode–cathode voltage U at which the electron beam is formed can be expressed as $U > U_{cr1} \equiv NL\sigma_0\varepsilon_0/e$, where L is the distance between plane electrodes and σ_0 is the ionization cross section at an electron energy of $\varepsilon \sim \varepsilon_0 \sim 2J$.

The runaway of a considerable fraction of electrons (~50%) takes place under the condition that

$$\frac{m_e N}{eE}\int_0^{\sqrt{2U/m_e}} \sigma_i(v) v dv > 1.$$

If the ionization cross section in the energy interval $\varepsilon_1 < \varepsilon < eU$ (which is most significant for the integration) can be approximated by the law $\sigma_i(\varepsilon) = \sigma_1\varepsilon_1/\varepsilon$ the condition of significant runaway electron fraction can be written in the following form:

$$U > U_{cr2} \equiv NL\sigma_1\varepsilon_1 \ln(eU/\varepsilon_1)/e.$$

For helium, $\sigma_1 \approx 4 \times 10^{-17}$ cm^2 and $\varepsilon_1 \approx 500$ eV. Assuming that $U \sim 100$ kV, the reduced critical field strength can be estimated as $E_{cr2}/N \equiv U_{cr2}/LN = \sigma_1\varepsilon_1\ln(eU/\varepsilon_1)/e \approx 10^{-13}$ (cm^3 V)/cm or $E_{cr2}/p \equiv U_{cr2}/Lp = (N/p)\sigma_0\varepsilon_1\ln(eU/\varepsilon_1)/e \approx 3.4$ kV/(Torr cm), where p is the room-temperature gas pressure.

The process of electron multiplication and runaway at a potential difference of U between two planes spaced by a distance L was numerically simulated using a modified particle-in-cell code described elsewhere [9]. The results of numerical calculations (Fig. 1a) agree with the above theoretical estimate. For example, a runaway electron fraction of $\eta = 50\%$ (relative to the total number of electrons reaching the anode) for the pressures of 13.5 Torr (E = 62.5 kV/cm) and 25 Torr (E = 125 kV/cm) corresponds to $E/p = 4.6$ and 5 kV/(Torr cm), respectively.

It should be noted, however, that the electron beam current for $E < E_{cr2}$ (i.e., under intense electron multiplication conditions) has proved to be much higher than

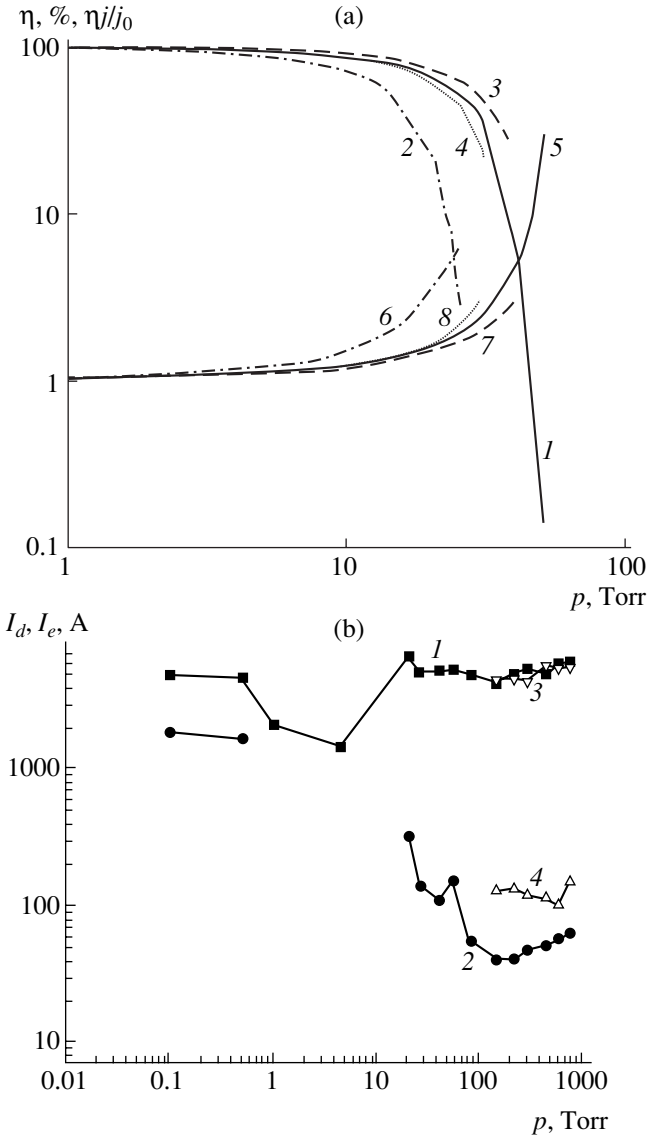

Fig. 1. Plots of the electron beam current characteristics versus helium pressure: (a) theoretical results showing (*1–4*) the fraction of runaway electrons η relative to the total number of electrons reaching anode and (*5–8*) the beam current per runaway electron $\eta j/j_0$ (j_0 and j being the current from cathode and the current to anode, respectively); the beam electrons are those with the energies $\varepsilon > 2eU/3$ [(*1*, *5*) L = 16 mm, U = 200 kV; (*2*, *6*) L = 16 mm, U = 100 kV; curves *3*, *4*, *7*, *8* are obtained for the same field strength E = 200 kV/16 mm = 125 kV/cm as curves *1* and *5*, but for different anode–cathode spacing H = 7.5 mm (*3*, *7*) and 28 mm (*4*, *8*)]; (b) experimental results showing (*1*, *3*) total diode current I_d and (*2*, *4*) electron beam current I_e behind the foil, for the diode with (*1*, *2*) foil cathode 1 and (*3*, *4*) graphite cathode 2 (anode–cathode distance, 28 mm; AlBe foil thickness, 45 μm).

that for $E > E_{cr2}$, although the runaway electron fraction η in the former case is smaller than that in the latter (Fig. 1a). In other words, the beam current generated at a given voltage applied between the electrodes can increase both with the pressure (Fig. 1a) and with the spacing H between electrodes (Fig. 2a). However, this takes place only as long as the field strength in the plasma is not reduced as a result of screening by the free charge.

Experiment. The investigation was conducted with a nanosecond pulse generator developed previously for the study of electron beam generation in vacuum [10]. The generator possessed a wave impedance of 30 Ω and produced in a matched load a voltage pulse of ~200 kV amplitude, a full width at half maximum (FWHM) of 4 ns, and a front width of ~1 ns.

The electron beams were generated in a diode filled with helium at a pressure variable from 0.1 to 760 Torr. The experiments were performed with two cathodes. Cathode 1 comprised a set of three coaxial cylinders (12, 22, and 30 mm in diameter) made of a 50-μm-thick titanium foil, embedded into one another and fastened on a duralumin substrate (36 mm in a diameter). The cylinder height decreased by 2 mm on the passage from smaller to greater ring. Cathode 2 represented a graphite disk with a diameter of 29 mm and rounded edges. The disk surface facing the output foil was convex with a curvature radius of 10 cm. The graphite disk was mounted on a round copper cathode holder with a diameter of 30 mm.

The electron beam was extracted from the diode via a 45-μm-thick AlBe foil mounted on the diode end flange. The beam current was measured with a graphite electrode placed at a distance of 10 mm from the foil and connected with a low-ohmic shunt to an amplifier case. We have also measured the "total" beam current to the end flange connected by another shunt to a cylindrical case of the vacuum diode. During the pressure measurements, a part of the diode current could be closed to the internal surface of a cylindrical case of the pulse generator in the diode.

Experimental results. We have observed four characteristic regimes of the diode operation (Fig. 1b). The first regime was observed at a low helium pressure (0.1–1 Torr; E/p > 70 kV/(Torr cm)) in the diode with cathode 1, which provided additional field enhancement at the foil edge. This well-known accelerator operation mode ensured the maximum beam currents (>1 kA) behind the foil. When the residual gas pressure was further reduced (>0.01 Torr), the beam current amplitude in the diode became equal to the "total" diode current.

The second regime, observed at a medium pressure of helium (1–10 Torr; E/p > 7 kV/(Torr cm)), was characterized by a considerable instability from pulse to pulse because of the gas breakdown at low voltages. In this operation mode, the beam current could be measured only in separate pulses and only with the foil cathode 1. The total diode current measured on the edge flange was significantly lower as compared to that in the first regime. No beam current was detected in the first two regimes with the graphite cathode 2.

The third regime was observed at a medium pressure of helium (10–40 Torr; $E/p > 1.5$ kV/(Torr cm)), also only with the foil cathode 1. Additional increase in the helium pressure led, in comparison to the second regime, to an increase in the breakdown delay, a growth in the voltage drop on the interelectrode gap, and the appearance of a beam current (which amounted to about 30% of that in the first regime). As the helium pressure was increase above 100 Torr, the fourth regime was observed with both foil and graphite cathodes. This operation mode is characterized by very small values of the parameter E/p (<0.7 kV/(Torr cm)).

It should be noted that operation of the given generator with a pulse duration of 4 ns was accompanied by a shunting discharge and/or a discharge between foil anode and cathode. This resulted in "shorting" of the diode at the end of the voltage pulse. Accordingly, the total diode current was close to the short-circuit current and the beam current pulse was shorter than the voltage pulse measured on the matched load.

Figure 2 shows a plot of the beam current versus interelectrode gap width for the diode with cathode 1. As can be seen, the beam current behind the foil grows when the anode–cathode distance is increased from 7.5 to 28 mm. The electron energy estimated from the foil thickness indicates that half of the current is carried by electrons with an energy above 100 keV (see Fig. 2 for the electron beam transmitted via two foils), the fraction of such electrons being proportional to the total beam current.

As for the graphite cathode 2, the maximum of the electron energy distribution in the beam corresponded to ~150 keV. It should be noted that we have detected electrons with anomalously high energies (exceeding eU), which was also reported in [2, 3].

The discharge shapes observed in the gas-filled diode operating in the fourth regime were different for cathodes 1 and 2. A discharge with the foil cathode 1 represented separate channels, while that with the graphite cathode 2 was more homogeneous. Such a difference was also reported previously [1, 3].

In our opinion, the most important experimental result consists in that using the graphite cathode 2 allowed the beam current to be significantly increased (up to 140 A, at a current density above 10 A/cm^2). Under these conditions, electrons reached the anode at greater interelectrode distances (in contrast to what was observed in [1]). The electron beam spot size on the foil in the diode with cathode 2 was ~40 mm (the spot color was uniform across the beam).

Discussion of results. A quantitative comparison of the theoretical and experimental results is hindered by the fact that it is still impossible to correctly take into account the electric field screening effects. Indeed, the gas breakdown leads to the formation of plasma which possessing higher conductivity as compared to that in the remaining part of the discharge gap and is capable of shunting the gap within a time period from fractions of nanosecond to a few nanoseconds. This plasma can also serve as a source of electrons (plasma cathode, see [11]). Nevertheless, some qualitative conclusions are possible.

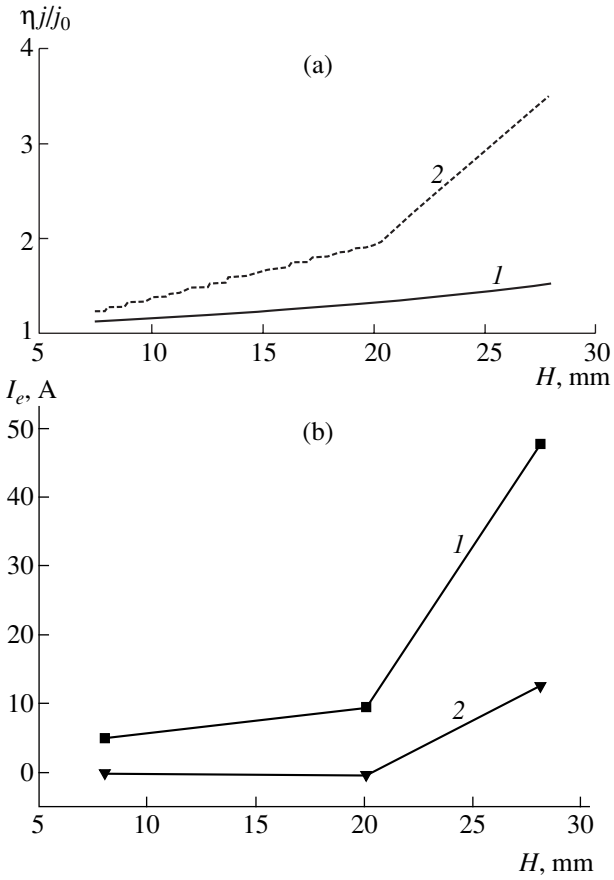

Fig. 2. Plots of the beam current characteristics versus anode– cathode distance H: (a) theoretical $\eta j/j_0$ values calculated for a helium pressure of (*1*) 10 Torr and (b) 20 Torr; (b) experimental electron beam current I_e behind AlBe foils with a thickness of (*1*) 45 and (*2*) 90 μm (foil cathode 1; helium pressure, 1 atm).

Using Fig. 1b (curve *2*), it is possible to determine the value of E/p at which the beam current exhibits significant growth (>3 kV/(Torr cm)). This estimate agrees with the calculated E/p value (Fig. 1a) at which the fraction of runaway electrons tends to increase (third regime). Some discrepancy can be related to a difference in voltage across the gap under real experimental conditions. The voltage pulse duration of 4 ns was sufficient to shorten the gap in all regimes featuring stable electron beam formation.

In the experiments, the beam current behind the foil was detected with both cathodes for $E/p <$ 0.7 kV/(Torr cm), when the fraction of runaway electrons is small. For the foil cathode 1, the beam current exhibited growth with the gas pressure from 150 to 760 Torr, whereby the parameter E/p decreases from 0.5 to 0.1 kV/(Torr cm). This behavior can be compared

to the results of calculations in Fig. 1a, where the beam current also increases with decreasing E/p. The experimentally observed growth of the beam current with the interelectrode distance (Fig. 2b) is also consistent with the results of calculations presented in Fig. 2a.

Thus, the results of experimental and theoretical investigations of the conditions for the electron beam formation in helium show that accelerated runaway electrons are generated both for $E/p > 3$ kV/(Torr cm) (this regime ensuring the electron beam formation at a high efficiency) and for relatively small values of this parameter, $E/p = 0.1$–0.5 kV/(Torr cm). The electron beams obtained in the helium-filled diode had a current amplitude of up to 140 A (with a beam current density above 10 A/cm^2) at an electron energy of ~150 keV.

Acknowledgments. The authors are grateful to S.D. Korovin for kindly providing the nanosecond pulse generator.

This study was supported by the International Scientific-Technological Center, grant no. 1270.

REFERENCES

1. L. V. Tarasova and L. N. Khudyakova, Zh. Tekh. Fiz. **39**, 1530 (1969) [Sov. Phys. Tech. Phys. **14**, 1148 (1969)].
2. L. V. Tarasova, L. N. Khudyakova, T. V. Loiko, and V. A. Tsukerman, Zh. Tekh. Fiz. **44**, 564 (1974) [Sov. Phys. Tech. Phys. **19**, 351 (1974)].
3. L. P. Babich, T. V. Loiko, and V. A. Tsukerman, Usp. Fiz. Nauk **160** (7), 49 (1990) [Sov. Phys. Usp. **33**, 521 (1990)].
4. Yu. D. Korolev and G. A. Mesyats, *The Physics of Pulse Breakdown in Gases* (Nauka, Moscow, 1991).
5. G. V. Kolbychev, P. D. Kolbycheva, and I. V. Ptashnik, Zh. Tekh. Fiz. **66** (2), 59 (1996) [Tech. Phys. **41**, 144 (1996)].
6. Yu. E. Kolyada, Pis'ma Zh. Tekh. Fiz. **26** (16), 52 (2000) [Tech. Phys. Lett. **26**, 721 (2000)].
7. A. R. Sorokin, Pis'ma Zh. Tekh. Fiz. **28** (9), 14 (2002) [Tech. Phys. Lett. **28**, 361 (2002)].
8. A. P. Bokhan and P. A. Bokhan, Pis'ma Zh. Tekh. Fiz. **28** (11), 21 (2002) [Tech. Phys. Lett. **28**, 454 (2002)].
9. A. N. Tkachev and S. I. Yakovlenko, Laser Phys. **12**, 1022 (2002).
10. V. P. Gubanov, S. D. Korovin, I. V. Pegel', *et al.*, Izv. Vyssh. Uchebn. Zaved. Fiz., No. 12, 110 (1996).
11. E. Arnold, M. I. Lomaev, V. S. Skakun, *et al.*, Laser Phys. **12**, 1227 (2002).

Translated by P. Pozdeev

Technical Physics Letters, Vol. 29, No. 8, 2003, pp. 683–686. Translated from Pis'ma v Zhurnal Tekhnicheskoĭ Fiziki, Vol. 29, No. 16, 2003, pp. 54–62.

The Mechanism of Electron Runaway in a Gas and a Criterion of the Self-Sustained Discharge Initiation

A. N. Tkachev and S. I. Yakovlenko

Institute of General Physics, Russian Academy of Sciences, Moscow, 117924 Russia

Received March 11, 2003

Abstract—The results of simulations using a particle-in-cell technique show that the phenomenon of electron runaway in a gas is determined by the condition that the interelectrode distance must be comparable with the Townsend electron multiplication length, rather than by local criteria commonly accepted at present. For a given gas, a critical voltage between the electrodes, for which the fraction of runaway electrons is relatively large, is a universal function of the product of the electrode spacing and the gas pressure. The same function determines a condition of the self-sustained discharge initiation in which the electron multiplication plays a significant role. This function has, besides the well-known Paschen branch, an additional upper branch describing breakage of the self-sustained discharge operation as a result of a sufficiently rapid application of a high voltage between the electrodes. © *2003 MAIK "Nauka/Interperiodica".*

Introduction

The phenomenon of electron runaway from a fully ionized plasma consists essentially in that, in a sufficiently large electric field, the energy gained by an electron during free flight is higher than that lost in collisions with particles of the plasma. If an external electric field penetrates through the plasma, a certain fraction of high-energy electrons will be repeatedly accelerated. The runaway effect for electrons in a plasma was predicted long ago [1] and supported by numerical calculations [2, 3] and analytical description in the case of weak fields [4]. This phenomenon plays an important role in the diagnostics and energy balance of impurities in tokamak plasmas [5].

The phenomenon of electron runaway is also observed in gases [6, 7]. This effect underlies operation the so-called open discharge [8–11] used, in particular, for pumping lasers [2, 13].

Below we will demonstrate that, in contrast to the commonly accepted notions, the mechanism of electron runaway in a gas- discharge plasma is substantially different from that operating in a fully ionized plasma. In the former case, the electron runaway takes place under conditions of Townsend ionization (see, e.g., [14]), whereby the energy gained in the field is compensated by the losses for excitation and ionization of the gas molecules. The runaway electrons appear only when the characteristic electron multiplication length (or the Townsend reciprocal multiplication factor) becomes comparable with or greater than the interelectrode distance.

Electron Multiplication and Runaway

Description of model. In order to confirm the above assumption, we have simulated the process of electron multiplication and runaway in helium and xenon using a modified particle-in-cell technique [15]. According to the model adopted, electrons were generated on a cathode with randomly directed initial velocities and the Poisson energy distribution with a mean value of $\varepsilon_0 = 0.2$ eV.

The equations of motion for all electrons were solved within small time steps and the elastic and inelastic collisions were played with the probabilities determined by cross sections of the corresponding elementary events. We took into account excitation of the 2^3S, 2^1S, 2^3P, and 2^1P states in helium and the $5p^56s$ ($J = 1$) state with $E = 8.44$ eV in xenon, using the published data for helium [16–18] and xenon [14, 21, 22].

The Townsend ionization regime. The results of our calculations showed that the Townsend ionization actually takes place, while the runaway electrons are absent, at all values of the reduced field strength E/p in the range from 5 to 10^4 V/(Torr cm) and a sufficiently large distance d between the electrodes. The number of excitation and electron generation events exponentially increases with the distance x from the cathode, while certain constant mean velocity and energy of the electrons are established at a sufficiently large distance from the cathode. The maximum of the energy distribution function for electrons reaching the anode is observed at low energies. The Townsend multiplication coefficient α_i is determined by the slope of a plot of the logarithm of the number of ionization events versus current.

In agreement with the commonly accepted behavior, the α_i value has proved to be proportional to the gas density (pressure) and can be written in the form of $\alpha_i(E, p) = p\xi(E/p)$. For helium and xenon, the function

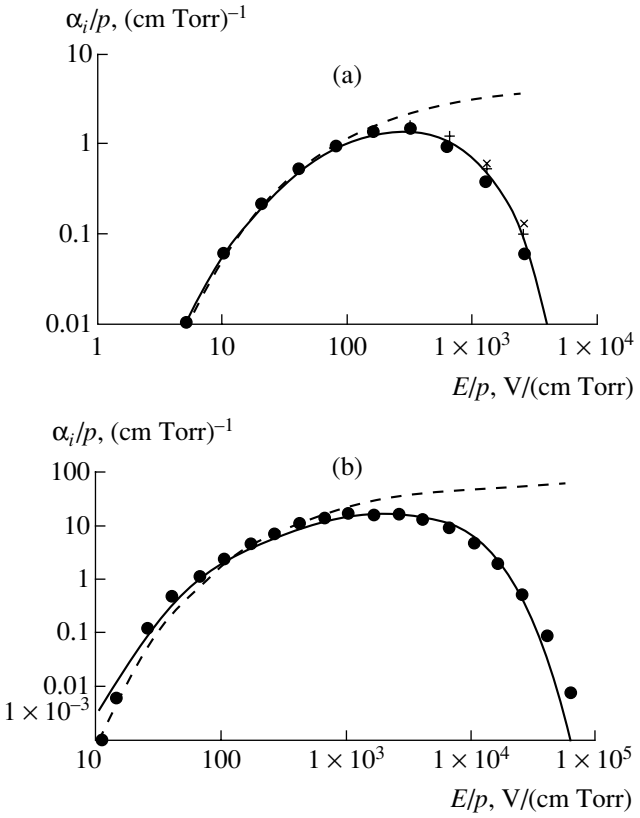

Fig. 1. Plots of the normalized Townsend coefficient α_i/p versus reduced electron energy E/p for (a) helium and (b) xenon, calculated for (•) p = 100 Torr ($N_{He} = 3.22 \times 10^{18}$ cm^{-3}), (+) p = 10 Torr, and (×) p = 1 Torr. Solid and dashed curves correspond to the approximation functions (2) and (1), respectively.

$\xi(E/p)$ obeys an experimentally established approximation [14, 23]

$$\xi(E/p) = A\exp\left(-B\left(\frac{p}{E}\right)^{1/2}\right), \qquad (1)$$

where A = 4.4 (cm Torr)$^{-1}$ and B = 14 (V/(cm Torr))$^{1/2}$ for helium and A = 65.3 (cm Torr)$^{-1}$ and B = 36.1 (V/(cm Torr))$^{1/2}$ for xenon.

However, our calculations showed (Fig. 1) that the approximation (1) is valid only for relatively small reduced field strengths $E/p < (E/p)_{cr}$, where $(E/p)_{cr}$ = 200 V/(Torr cm) for helium and 1500 V/(Torr cm) for xenon. As the E/p value increases above the critical level, the multiplication coefficient α_i begins to decrease. The drop of α_i with increasing E/p is related to a decrease in the ionization cross section at large energies.

In connection with this, we propose the following approximation of the Townsend multiplication coefficient, which correctly describes a decrease in this parameter:

$$\xi(E/p) = A\exp\left(-B\left(\frac{p}{E}\right)^{1/2} - C\frac{E}{p}\right), \qquad (2)$$

where A = 5.4 (cm Torr)$^{-1}$, B = 14 (V/(cm Torr))$^{1/2}$, and C = 0.0017 (cm Torr)/V for helium and A = 45 (cm Torr)$^{-1}$, B = 31.1 (V/(cm Torr))$^{1/2}$, and C = 1.7 (cm Torr)/V for xenon.

Electron runaway. The results of our calculations showed that the Townsend ionization regime is established at a certain distance from the cathode $x \sim \alpha_i^{-1}$, which corresponds to the characteristic multiplication length. This conclusion was verified by numerical calculations. For $d < \alpha_i^{-1}$, the pattern of electron multiplication dramatically changes and a significant fraction of electrons are continuously accelerated with increasing distance to the anode. The peak of the energy distribution function for electrons reaching the anode corresponds to the maximum energy $eU = eEd$ acquired by the particle upon the flight from cathode to anode.

In contrast to the commonly accepted notions, the results of our calculations showed that the Townsend electron multiplication mechanism remains valid for any E and p values, provided that the distance d is sufficiently large. Accordingly, we suggest that a criterion for the appearance of a significant proportion of runaway electrons should be formulated as follows:

$$\alpha_i(E_{cr}, p)d = 1. \qquad (3)$$

This is at variance with the common opinion that the runaway electrons appear when the E/p ratio exceeds a certain critical value that is independent of d [6, 7, 14].

The proposed criterion (3) can be written in a universal form based on the knowledge of the dependence of α_i on E and p. Assuming that $\alpha(E, p) = p\xi(E/p)$, where $\xi(E/p)$ is a function characteristic of a given gas, we obtain

$$pd\xi(U_{cr}/pd) = 1. \qquad (4)$$

This formula implicitly takes into account a dependence of the critical voltage U_{cr} (corresponding to the onset of a significant electron runaway) on the product pd of the gas pressure and the interelectrode distance. The curve $U_{cr}(pd)$ separates the regions of effective electron multiplication from that of effective runaway, where electrons can leave the discharge gap before being involved into multiplication process. This curve is universal for a given gas.

Figure 2 presents the curves of $U_{cr}(pd)$ calculated for helium and xenon using formula (4) and the numerical data. Note that electrons always leave the discharge gap without significant multiplication, provided that pd is smaller than pd_{min} ($pd_{min} \approx 0.17$ and 0.055 Torr cm for helium and xenon, respectively). At low voltages, the system features the drift of low-energy electrons inca-

pable of effectively ionizing the gas. At large voltages, electrons exhibit runaway due to a small ionization cross section.

A Criterion for the Self-Sustained Discharge Formation

Upper branch of the curve of self-sustained discharge operation. A curve determining the criterion of discharge initiation is usually constructed based on the condition that each electron generates a number of ions sufficiently large to provide that the secondary emission ensures the production of another electron on the cathode. Accordingly, the discharge initiation (gas breakdown) potential $U_{br}(pd)$ is determined by the condition (see, e.g., [14])

$$\alpha_i(E, p)d = \ln(1 + 1/\gamma) \quad \text{or} \quad pd\xi(U_{br}/pd) = L, \quad (5)$$

where $L \equiv \ln(1 + 1/\gamma)$ and γ is the secondary electron emission coefficient. Comparing the criteria of discharge initiation (5) and electron runaway (4), we obtain a relation $U_{br}(pd) = LU_{cr}(pd/L)$ that was used to construct the $U_{br}(pd)$ curves in Fig. 2.

The function $U_{br}(pd)$ obtained as described above contains essentially new information as compared to that provided by the well-known Paschen curve. As is known, the Paschen curve consists of the right and left branches corresponding to the regions of large and small pd values relative to the minimum. These branches are in fact present in the calculated $U_{br}(pd)$ curves. However, according to the results of our analysis, the curve describing the self-sustained discharge initiation must have an additional (upper) branch corresponding to the drop of α_i with increasing E/p. Another important result is the existence of a minimum pd value ($pd_{\min}$) at which the self-sustained discharge can form due to the electron multiplication.

The existence of the upper branch of the self-sustained discharge initiation curve is quite clear from the general considerations. This branch reflects a drop of the inelastic interaction cross section with increasing electron energy.

Comparison of theory and experiment. It should be noted that $U_{br}(pd)$ is not as general characteristic as $U_{cr}(pd)$. The "runaway curve" $U_{cr}(pd)$ is universal for a given gas, while the "breakdown curve" $U_{br}(pd)$ depends on the model describing the discharge initiation, in particular, on the properties of electrodes. This can be seen from as comparison of the results of our model calculations to the experimental data (Fig. 2).

As demonstrated by Penning [24], the Paschen curve for helium exhibits a loop with the turning point at $pd \approx 1.5$ Torr cm. This feature agrees well with the results of our calculations. Penning correctly suggested that the loop is related to the presence of the maximum in the ionization cross section as a function of the electron energy, but the hypothesis is still not commonly accepted. This is probably related to the fact (see, e.g., [25]) that the analogous curves for other inert gases exhibit no such loops, although the ionization cross sections also exhibit maxima. A similar loop was reported only for mercury [26].

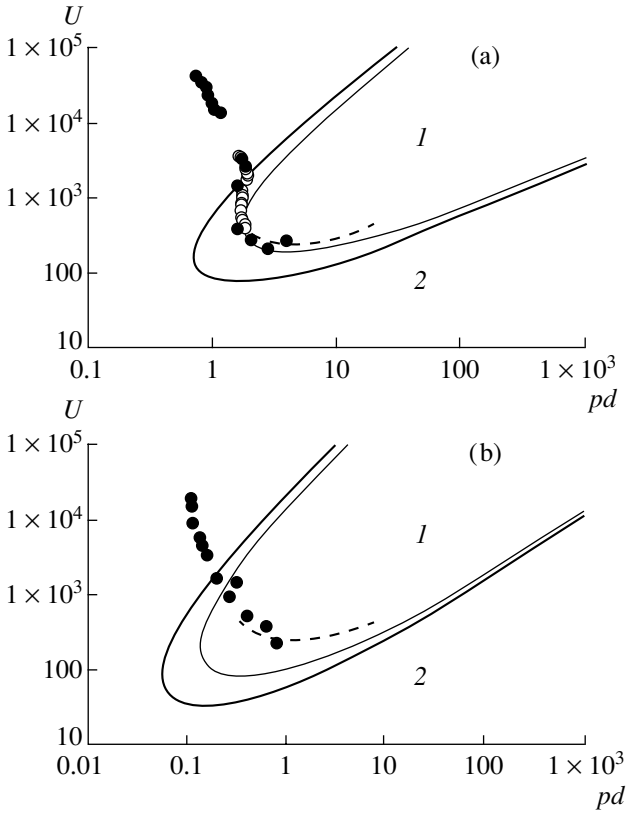

Fig. 2. Criteria of the electron runaway $U_{cr}(pd)$ (thick solid curves) and the self-sustained discharge initiation $U_{br}(pd)$ for $L = \ln(1 + 1/\gamma) = 2.45$ (thin solid curves) in (a) helium and (b) xenon: (•) experimental data from [25]; (dashed curves) experimental data from [14]; (○) experimental data of Penning [24]; (*1*) the region of electron multiplication in a self-sustained discharge; (*2*) the region of electron runaway from a discharge gap without multiplication.

Apparently, the part of the Paschen curve to the left of $pd_{\min}$ corresponds to a different mechanism of discharge initiation, which is weakly related to the phenomenon of electron multiplication in the gas. This is evidenced by the fact that this Paschen curve in this region depends not only on the cathode material, but on the anode material as well [25]. Additional investigations are necessary in order to elucidate a mechanism corresponding to this part of the curve.

Conclusions

The effect of electron runaway in a gas is observed when a distance between electrodes is comparable with or smaller than the characteristic electron multiplication length. This is a substantial difference between the runaway phenomena in the Coulomb plasma and in a

gas. The distinction is related to the fact that fully ionized plasma features acceleration of the existing electrons, rather than the production of new electrons with relatively small velocities. In a gas discharge between spaced electrodes, the number of generated electrons exponentially increases with the interelectrode distance. On this background, the fraction of fast electrons exhibiting no collisions becomes negligibly small.

It is also established that a critical voltage between the electrodes, for which the fraction of runaway electrons becomes relatively large, is a universal function of the product of the electrode spacing and the pressure of a given gas. The same function determines a condition of the self-sustained discharge initiation for which the electron multiplication plays a significant role. This function has an additional upper branch describing breakage of the self-sustained discharge operation as a result of a sufficiently rapid application of a high voltage between the electrodes. Approximations of this function for helium and xenon have been found.

Acknowledgments. The authors are grateful to V.F. Tarasenko for stimulating discussions.

This study was supported by the International Scientific-Technological Center, grant no. 1270.

REFERENCES

1. R. G. Giovanelly, Philos. Mag. **40**, 206 (1949).
2. H. Dreiser, Phys. Rev. **115**, 238 (1959); Phys. Rev. **117**, 329 (1960).
3. R. M. Kurlsrud, Y. C. Sun, N. K. Winson, and H. A. Fallon, Phys. Rev. Lett. **31**, 690 (1973).
4. A. V. Gurevich, Zh. Éksp. Teor. Fiz. **39**, 1296 (1960) [Sov. Phys. JETP **12**, 904 (1960)].
5. V. S. Marchenko and S. I. Yakovlenko, Fiz. Plazmy **5**, 590 (1979) [Sov. J. Plasma Phys. **5**, 331 (1979)].
6. L. P. Babich, T. V. Loĭko, and V. A. Tsukerman, Usp. Fiz. Nauk **160** (7), 49 (1990) [Sov. Phys. Usp. **33**, 521 (1990)].
7. Yu. D. Korolev and G. A. Mesyats, *The Physics of Pulse Breakdown in Gases* (Nauka, Moscow, 1991).
8. G. V. Kolbychev, P. D. Kolbycheva, and I. V. Ptashnik, Zh. Tekh. Fiz. **66** (2), 59 (1996) [Tech. Phys. **41**, 144 (1996)].
9. A. R. Sorokin, Pis'ma Zh. Tekh. Fiz. **26** (24), 89 (2000) [Tech. Phys. Lett. **26**, 1114 (2000)].
10. A. R. Sorokin, Pis'ma Zh. Tekh. Fiz. **28** (9), 14 (2002) [Tech. Phys. Lett. **28**, 361 (2002)].
11. A. P. Bokhan and P. A. Bokhan, Pis'ma Zh. Tekh. Fiz. **28** (11), 21 (2002) [Tech. Phys. Lett. **28**, 454 (2002)].
12. V. I. Derzhiev, V. F. Tarasenko, S. I. Yakovlenko, and A. M. Yancharina, in *Collection of Scientific Works of the Institute of General Physics, Russian Academy of Sciences*, Vol. 21: *Plasma Lasers of Visible and Near IR Ranges*, Ed. by S. I. Yakovlenko (Nauka, Moscow, 1989), pp. 5–41.
13. S. I. Yakovlenko, in *Encyclopedia of Low-Temperature Plasma*, Vol. 4: *Gas and Plasma Lasers*, Ed. by V. E. Fortov, pp. 262–291.
14. Yu. P. Raĭzer, *The Physics of Gas Discharge* (Nauka, Moscow, 1992), p. 43.
15. A. N. Tkachev and S. I. Yakovlenko, Proc. SPIE **4747**, 271 (2002); Laser Phys. **12**, 1022 (2002).
16. E. Krishnakumar and S. K. Srivastava, J. Phys. B **21**, 1055 (1988).
17. D. V. Fursa and I. Bray, Phys. Rev. A **52**, 1279 (1995).
18. J. C. Nickel, K. Imre, D. F. Register, and S. Trajmar, J. Phys. B **18**, 125 (1985).
19. M. Surendra, D. B. Graves, and G. M. Jellum, Phys. Rev. A **41**, 1112 (1990).
20. *Physical Quantities. Handbook*, Ed. by I. S. Grigor'ev and E. Z. Meĭlikhov (Énergoatomizdat, Moscow, 1991).
21. E. Krishnakumar and S. K. Srivastava, J. Phys. B **21**, 1055 (1988).
22. A. M. Eletskiĭ and B. M. Smirnov, *Physical Processes in Gas Lasers* (Énergoatomizdat, Moscow, 1985), p. 44.
23. A. L. Ward, J. Appl. Phys. **33**, 2789 (1962).
24. F. M. Penning, Physica **12** (4), 65 (1932).
25. A. N. Dikidzhi and B. N. Klyarfel'd, Zh. Tekh. Fiz. **25**, 1038 (1955).
26. L. G. Guseva and B. N. Klyarfel'd, Zh. Tekh. Fiz. **24**, 1169 (1954).

Translated by P. Pozdeev

Technical Physics Letters, Vol. 29, No. 8, 2003, pp. 687–690. Translated from Pis'ma v Zhurnal Tekhnicheskoĭ Fiziki, Vol. 29, No. 16, 2003, pp. 63–71.

The Surface Conductivity of Gamma-Irradiated Ceramic Dielectrics

M. I. Muminov and V. N. Sandalov*

Institute of Nuclear Physics, Academy of Sciences of the Republic of Uzbekistan, Ulugbek, Tashkent District, Uzbekistan

** e-mail: sandalov@suninp.tashkent.su*

Received February 11, 2003

Abstract—We have studied the surface dc conductivity of commercial alumina based ceramic dielectrics of the UF-46 and GB-7 types in a temperature interval from 200 to 400 K before and after gamma irradiation to a dose of 10^4–10^5 Gy. The two ceramics differ in the content of the α-Al_2O_3 crystal phase (72 wt % for UF-46 versus 86 wt % for GB-7) and in the total specific area of the grain boundaries (3.40 m^2/kg for UF-46 versus 4.56 m^2/kg for GB-7). In the temperature interval studied, the surface conductivity obeys a power law with the exponent dependent on the grain boundary area and the gamma radiation dose. Irradiation leads to a significant decrease in the exponent, the effect being more pronounced for ceramics with a greater grain boundary area. It is suggested that the electric conductivity proceeds according to a polaron mechanism, with a multiphoton character of the corresponding electron transitions. © *2003 MAIK "Nauka/Interperiodica".*

Introduction. In recent years, increasing application of thin dielectric films and other coatings has posed the task of elucidating the mechanisms of electric conductivity in such systems and, in particular, the role of grain boundaries (GBs) in the total surface electric charge transfer. The bulk conductivity of commercial ceramics of the UF-46 and GB-7 types before and after exposure to ionizing radiations has been studied in sufficient detail in a broad temperature range. It was established that the bulk conductivity in these materials proceeds by various mechanisms, including migration of weakly bound alkali metal ions (at $T > 420$ K), hopping charge transfer via nonlocalized states (300 K < T < 420 K), and electron hopping via localized states near the Fermi level at lower temperatures [1–5].

The surface conductivity of alumina based ceramics at low temperatures ($T < 300$ K) is mostly due to the migration of electrons and can be satisfactorily described by the Mott law: $\sigma_s = B\exp((A_0/T)^{1/4})$ [3]. Experimental data revealed a decisive role of GBs in the conductivity, especially in multicomponent dielectrics such as ceramics [3–5]. Investigations of the surface conductivity in gamma-irradiated ceramics at $T >$ 300 K showed that $\sigma(T)$ possesses the activation character, whereby the activation energy is inversely proportional to the radiation dose rate [6].

This Letter reports the results of our measurements of the low-temperature ($T < 400$ K) surface conductivity in disordered dielectrics before and after exposure to ionizing radiation.

Experimental method. The surface conductivity was studied in plane-parallel samples of commercial ceramics of the UF-46 and GB-7 types. The measurements were performed in the temperature interval from 200 to 440 K before and after gamma irradiation of the samples to a dose of 10^4–10^5 Gy. This dose range was selected because electrons generated upon exposure to a gamma radiation dose above 10^4 are known to fill shallow traps [7]. As the temperature increases, these traps inject additional carriers, which increase the experimental resolution. The two ceramics differ in the content of the α-Al_2O_3 crystal phase (72 wt % for UF-46 versus 86 wt % for GB-7) and in the total specific GB area (3.40 m^2/kg for UF-46 versus 4.56 m^2/kg for GB-7) [4].

The surface current was measured by a three-electrode voltammetric technique using silver electrodes deposited onto the sample surface. The measuring cell with a sample and an electric heater was placed in a hermetic chamber connected to a vacuum system. Prior to measurements, the air containing water vapor was evacuated from the chamber and the system was cooled to 200 K. Then, a dc bias voltage was applied to the electrodes and the surface current was measured in the course of gradual heating of the sample. The sample temperature was controlled by changing voltage applied from a transformer to the electric heater and measured with a chromel–copel thermocouple. The sample was heated at a constant rate of 3 K/min. A dc voltage applied to the sample was 300 V, which corresponds to the interval of validity of Ohm's law [1].

The surface electric resistance of a flat sample is given by the formula

$$R_s = \frac{1}{\sigma_s}\int_{D/2}^{d/2}\frac{dr}{2\pi r} = \frac{1}{\sigma_s}\ln\frac{d}{D}, \qquad (1)$$

1063-7850/03/2908-0687$24.00 © 2003 MAIK "Nauka/Interperiodica"

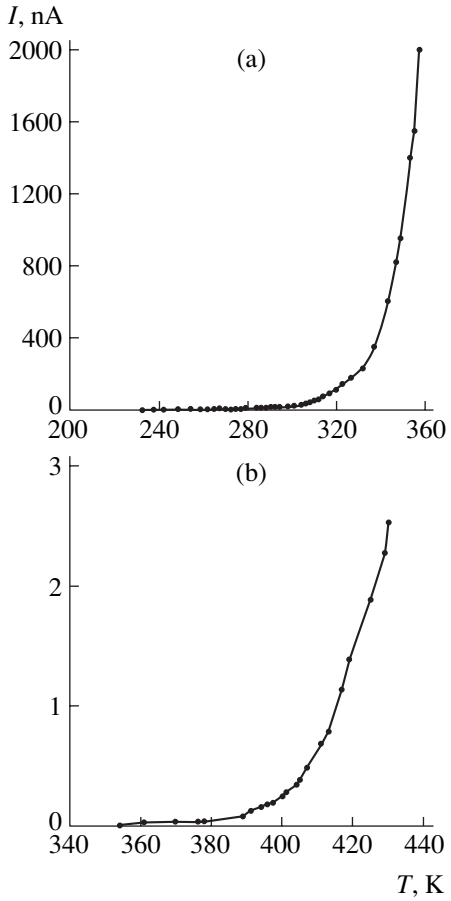

Fig. 1. Temperature dependence of the surface current in unirradiated ceramics: (a) UF-46 and (b) GB-7.

where D is the working electrode diameter and d id the internal diameter of the storage electrode. Expanding $\ln(d/D)$ into series, we obtain

$$\sigma_s = \frac{(D+d)}{(d-D)}\frac{J}{\pi U}, \quad (2)$$

where J is the currents passing in the surface layer of the sample and U is the applied dc bias voltage.

Experimental results. Figure 1 shows the experimental temperature dependences of the surface current measured in unirradiated samples of the UF-46 and GB-7 ceramics. As can be seen from these data, the current in UF-46 is constant at temperatures below 280 K and then exhibits nonlinear growth (Fig. 1a). In GB-7, an analogous growth in the current begins at $T > 380$ K (Fig. 1b), but the current is significantly (approximately, by three orders of magnitude) lower than in the former material. According to these results, the plots of $\sigma_s(T)$ are nonlinear in the temperature interval from 280–440 K. Moreover, the nonlinear character was retained when the experimental data were replotted as σ_s versus $(1/T)^{1/4}$, which indicated that the temperature dependence of σ_s did not obey the Mott–Davies law. A more thorough analysis of this temperature dependence showed that it can be satisfactorily described by a power law of the type

$$\sigma = \sigma_0 T^n. \quad (3)$$

The activation energy of the bulk conductivity in UF-46 calculated for the same temperature interval is lower (approximately, two times) than the activation energy of the surface charge transfer [3, 5]. The same relations are valid for GB-7 ceramics. Irradiation of the samples leads to an increase in the surface conductivity of both ceramics. However, the relative change in σ_s of UF-46 is more significant than that of GB-7. As the radiation dose grows, the activation energy of the surface charge transfer decreases (Table 1).

Table 1. Activation energies of the surface charge transfer in UF- 46 ceramics gamma-irradiated to various doses

Material	Activation energy, eV			
	unirradiated	10^4 Gy	5×10^4 Gy	10^5 Gy
UF-46	1.21	1.07	0.87	0.74

A change in the activation energy of the bulk charge transfer in ceramics below room temperature was reported in [6], where this behavior was explained by an increase in the free charge carrier density as a result of the radiation-induced electron production. As can be seen from Table 2, the power exponent for both ceramics decrease with increasing radiation dose. This variation is correlated with decreasing activation energy of the surface charge transfer.

Discussion of results. A special feature of the ceramic technology is that the material is composed of crystal grains or grain clusters uniformly dispersed in an amorphous matrix. The ceramic grain dimensions may vary significantly, ranging from a few nanometers (for nuclei in a glassy phase) to tens of micrometers in a crystal phase. For this reason, the electrical properties of ceramics above room temperature are very much like those of glasses [5]. In particular, the temperature dependence of σ_s for ceramics, plotted in the Arrhenius coordinates of $\ln\sigma$ versus $1/T$, differs very slightly from the analogous plots for classes. In both cases, this is a curve with an activation energy smoothly varying with the temperature. This behavior complicates the analysis of the charge transport in such materials. In interpretation of the temperature variation of σ, different conductivity mechanisms have to be used in various narrow temperature intervals. In particular, the conductivity of ceramic dielectrics is described in terms of the Mott law, inverse Arrhenius law, etc. [1–7].

Explanation of the surface conductivity presents an even more complicated problem, because various relations can be simultaneously obeyed. Gudaev and Malinovskii [7–9] proposed a general conductivity mechanism which is common for all disordered materials and

adequately describes the experimentally observed behavior of $\sigma(T)$. This mechanism is based on the following assumption: for materials with dominating multiphonon transitions between the polaron states, the temperature dependence of the transition probability obeys the relation $W \sim [kT/h\omega]^n$, where the exponent n depends on the number of phonons [5]. This leads to a power law for the temperature dependence of the conductivity, $\sigma = \sigma_0 T^n$, with $n \gg 1$. The value of the parameter n depends on the sample composition and preparation technology. Thus, on plotting the temperature dependence of the electric conductivity in the coordinates of $\ln\sigma_s$ versus T, we have to obtain a curve composed of straight segments, the slope of each segment determining the corresponding exponent. Table 2 presents the values of n determined in this way.

Figure 2 shows the power temperature dependences of conductivity for the samples of UF-46 ceramics irradiated to various doses. In this case, a dominating mechanism of the electric conductivity is the carrier migration on the percolation level, which corresponds to a percolation cluster occurring on the tail of the density of states (exponentially decaying in depth of the forbidden band). The power law is obeyed primarily in disordered materials, where the electron transitions accompanied by the phonon interactions are highly probable [7–9]. However, the experiments showed that multiphonon transitions are also possible when the radius of a localized state is as large as that for transitions between states in the band tails, an example being offered by the surface conductivity of strongly disordered dielectrics. The polaron effects in the conductivity can be also expected in materials with ionic or partly ionic bonds, where the electron–phonon interaction is much stronger than that in materials with covalent bonds.

The samples studied in our experiments consist by more than 70 wt % of α-Al_2O_3 grains representing crystals with predominantly ionic bonds. The crystals of corundum are strongly doped, both with technologically controlled dopants and with uncontrolled impurities. The atoms and ions of metals (Ca, Mg, Na, Ti, etc.) substitute Al^{3+} ions to form point defects and defect regions (with modified grain boundaries). Such disordered regions are active sinks for radiation-induced defects. Irradiation is accompanied by continuous recharging of the existing defects and by the formation of new charged regions. The probability of the polaron conductivity becomes substantial when the time of the dielectric relaxation of polarized ions in the electron field is sufficiently large for the corresponding structural rearrangement around the electron to take place for a given drift rate and the electron–phonon interaction conditions, that is, at sufficiently low temperatures.

A decrease in E_s after gamma irradiation can be explained by the fact that gamma quanta generate a large number of additional charge carriers. These carriers, besides directly contributing to the conductivity, fill shallow traps at the surface [1, 4]. A common feature of ceramics is the absence of preferred orientation in the arrangement of grains. This peculiarity is especially well manifested on the surface. The surface of any solid always contains local electron states determining an overall energy state of the surface [4, 5]. These local states are related to the following main factors: (i) lattice periodicity broken on the surface; (ii) the presence of uncompensated (dangling) valence bonds of the surface atoms; (iii) adsorption of atoms from environment. In such systems, the order is usually violated on the GBs.

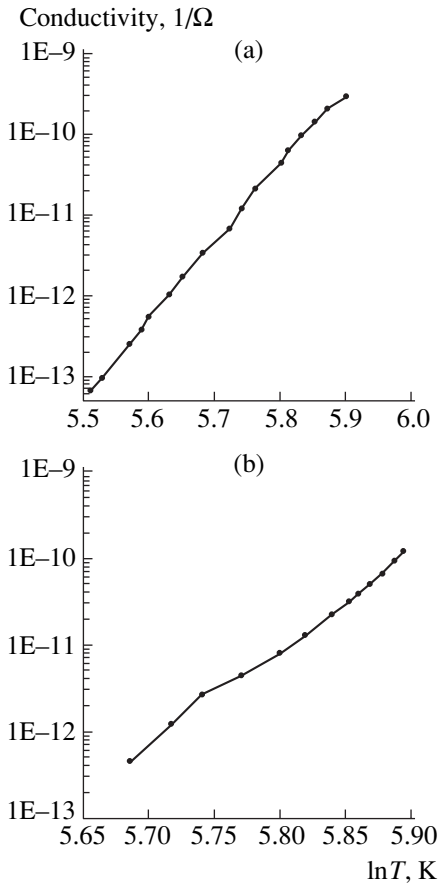

Fig. 2. Temperature dependence of the surface conductivity in UF-46 ceramics irradiated to (a) 10^4 Gy and (b) 5×10^4 Gy.

Table 2. Exponent n in the temperature dependence of the surface conductivity of ceramics gamma-irradiated to various doses

Material	Exponent n			
	unirradiated	10^4 Gy	5×10^4 Gy	10^5 Gy
UF-46	30	28	20	13
GB-7	33	26	18	12

The surface of ceramics possesses a higher GB density than does the bulk. The mutual orientation of grains and GBs is usually random. Although the mean density of atoms on the surface is equal to that in the bulk, superposition of the lattices of two grains leaves almost half of the lattice sites in the boundary layer mismatched [10]. Therefore, the GB traps on the surface are unsaturated and their density is sufficiently large to provide for a fast annihilation of the radiation-induced defects, which is primarily manifested by a decrease in the activation energy. The strong radiation-stimulated filling of shallow traps is unavoidably accompanied by increasing electron–phonon interaction [6, 9]. For this reason, a subsurface layer of the material, where the gamma radiation energy is dissipated, will unavoidably exhibit reconstruction. These transformations may also change the mechanical properties of this layer. Indeed, gamma radiation rather significantly changes the electrical characteristics, predominantly at the expense of elastic characteristics directly related to the mechanical properties. A decrease in the charge transfer activation energy under irradiation reflects the radiation-induced changes including (i) an increase in the density of shallow traps, (ii) a decrease in the carrier lifetime, and (iii) modification of the potential relief, predominantly of the most disordered surface layer [11]. Thus, a change in the elastic microcharacteristics of a subsurface layer can modify macrocharacteristics of the irradiated material.

Conclusion. (i) The surface dc conductivity of commercial alumina based ceramic dielectrics of the UF-46 (76 wt % α-Al_2O_3) and GB-7 (87 wt % α-Al_2O_3) types, also differing by the total specific GB area, was studied in a temperature interval from 200 to 400 K before and after gamma irradiation to a dose of 10^4–10^5 Gy.

(ii) In the temperature interval studied, the surface conductivity obeys a power law with the exponent dependent on the grain boundary area and the gamma radiation dose.

(iii) It is suggested that the electric conductivity in the materials studied proceeds according to a polaron mechanism, with a multiphoton character of the corresponding electron transitions.

(iv) Irradiation leads to a significant decrease in the exponent, the effect being more pronounced for the ceramics with a total GB area.

REFERENCES

1. N. S. Kostyukov, M. I. Muminov, S. M. Atrash, *et al.*, *Insulators and Radiation*, Vol. 1: *Radiation Electrical Conductivity* (Nauka, Moscow, 2001).
2. N. S. Kostyukov, M. I. Muminov, S. M. Atrash, *et al.*, *Insulators and Radiation*, Vol. 2: *Dielectric Permittivity and Dielectric Losses* (Nauka, Moscow, 2001).
3. E. S. Astapova, E. B. Pivchenko, and E. A. Vanina, Dokl. Akad. Nauk **376**, 611 (2001) [Dokl. Phys. **46**, 75 (2001)].
4. V. N. Sandalov and M. A. Mukhamedzhanov, in *Proceedings of the 11th International Workshop "Radiation Physics of Solids," Sevastopol, 2001*, pp. 23–25.
5. M. I. Muminov and V. N. Sandalov, in *Proceedings of the 4th International Conference "Modern Problems of Nuclear Physics" (MPNP-4), Tashkent, 2001*, pp. 190–191.
6. A. Stesmans and V. V. Afanasev, Appl. Phys. Lett. **80**, 1957 (2002).
7. O. A. Gudaev and V. K. Malinovskiĭ, Fiz. Tverd. Tela (St. Petersburg) **34**, 548 (1992) [Sov. Phys. Solid State **34**, 293 (1992)].
8. O. A. Gudaev and V. K. Malinovskiĭ, Fiz. Tverd. Tela (St. Petersburg) **37**, 81 (1995) [Phys. Solid State **37**, 41 (1995)].
9. O. A. Gudaev and V. K. Malinovskiĭ, Fiz. Tverd. Tela (St. Petersburg) **44**, 805 (2002) [Phys. Solid State **44**, 837 (2002)].
10. A. S. Bakaĭ, Pis'ma Zh. Tekh. Fiz. **9**, 1477 (1983) [Sov. Tech. Phys. Lett. **9**, 632 (1983)].
11. O. Perevezentsev, Zh. Tekh. Fiz. **71** (11), 136 (2001) [Tech. Phys. **46**, 1481 (2001)].

Translated by P. Pozdeev

Technical Physics Letters, Vol. 29, No. 8, 2003, pp. 691–693. Translated from Pis'ma v Zhurnal Tekhnicheskoĭ Fiziki, Vol. 29, No. 16, 2003, pp. 72–79.

Quantum Dots in InAs Layers of Subcritical Thickness on GaAs(100)

A. A. Tonkikh[a], G. E. Cirlin[b], V. G. Dubrovskii[a], Yu. B. Samsonenko[a], N. K. Polyakov[a], V. A. Egorov[a], A. G. Gladyshev[b], N. V. Kryzhanovskaya[b], and V. M. Ustinov[b]

[a] *Institute of Analytical Instrument Building, Russian Academy of Sciences, St. Petersburg, Russia*
e-mail: iap@ianin.spb.su

[b] *Ioffe Physicotechnical Institute, Russian Academy of Sciences, St. Petersburg, Russia*

Received March 5, 2003

Abstract—Ensembles of InAs quantum dots formed at the GaAs(100) surface have been studied by the methods of reflection high-energy electron diffraction and photoluminescence. The amount of deposited InAs corresponds to a wetting layer thickness smaller than the critical value necessary for the transition from two- to three-dimensional growth. It is experimentally shown that, at a deposited film thickness of 1.5 and 1.6 monolayers, islands are formed after keeping the sample in a flow of As_4. The influence of the substrate temperature on the kinetic characteristics of the formation of InAs/GaAs islands has been studied. © *2003 MAIK "Nauka/Interperiodica".*

In recent years, the number of papers devoted to the formation of quantum dots (QDs) in lattice-mismatched heteroepitaxial systems, in particular, in the In(Ga,Al)As/GaAs system, has been growing steadily. This is explained to a considerable extent by the progress in the development of semiconductor laser diodes with the active area based on QD ensembles [1, 2]. However, many effects associated with the QD formation are still insufficiently studied. For example, the so-called "parquet" structures were observed [3, 4] when the InAs films with an intermediate thickness of 1.0–1.5 monolayer (ML) were deposited onto a GaAs surface. A specific feature of such structures is their periodicity. Nanoobjects with a mean height of about 2–3 ML and a mean lateral size of about 25 nm were spaced from each other on the average by 30 nm. In addition, it was shown [4] that the period of such structures increases up to 40–50 nm after keeping the sample in a flow of As_4.

We have continued investigations in this direction. In contrast to the previous investigations [3, 4], this study is devoted to transformation of an elastically strained InAs wetting layer (WL) with a thickness of 1.5–1.6 ML into an ensemble of nanodimensional islands and a residual layer, whose thickness depends on the conditions of InAs deposition.

The samples were grown on semi-insulating GaAs(100) substrates using an EP1203 molecular beam epitaxy setup. The process of deposition of the initial InAs layer and reconstruction of the elastically strained layer into the islands–WL system was studied *in situ* using the patterns of reflection high-energy electron diffraction (RHEED). Two series of samples were grown, with an initial InAs layer thickness of 1.6 ML in the first series and 1.5 ML in the second series. The samples of each series differed by the substrate temperatures in the course of InAs deposition, which varied in the range from 420 to 485°C. After the InAs layer deposition, the samples were kept in a flow of As_4 for a certain period of time variable from 1.5 to 2.5 min. Immediately after that, the surface was covered with a 50-Å-thick GaAs layer at the same temperature of the substrate. In order to prevent the transport of nonequilibrium carriers into a subsurface region and the substrate during the optical investigations, the active region was bounded from both sides by short-period superlattices $Al_{0.25}Ga_{0.75}As$/GaAs (5 pairs, 25 Å/25 Å). From the top, the structure was covered by a 5-nm-thick GaAs layer. The buffer area, the superlattices, and the upper GaAs layer were grown at a temperature of 585°C. The photoluminescence (PL) was excited by an Ar^+ laser operating at $\lambda = 514.5$ nm with an excitation power density of ~100 W/cm^2. The emission was detected by a cooled Ge photodiode.

The main parameters and data measured for the samples studied are summarized in the table. The RHEED patterns observed *in situ* showed no island formation upon deposition of a 1.6 ML thick InAs film. The characteristic diffraction pattern in this case consists of lines representing only the main reflections, superstructure reflections being absent. Keeping the samples in a flow of As_4 after the InAs film deposition leads in most cases to significant changes in the RHEED pattern. There appear bulk diffraction reflections characteristic of the island growth. After the appearance of these reflections, the surface is kept in the As_4 flow for some time, which results in the forma-

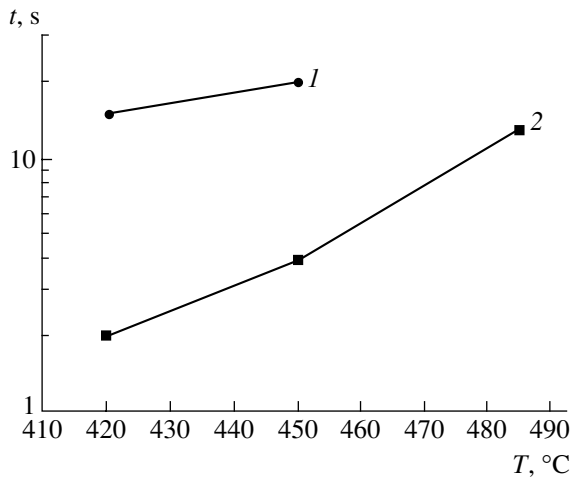

Fig. 1. Plots of the QD formation time versus substrate temperature for the structures with an InAs layer thickness of (*1*) 1.5 and (*2*) 1.6 ML.

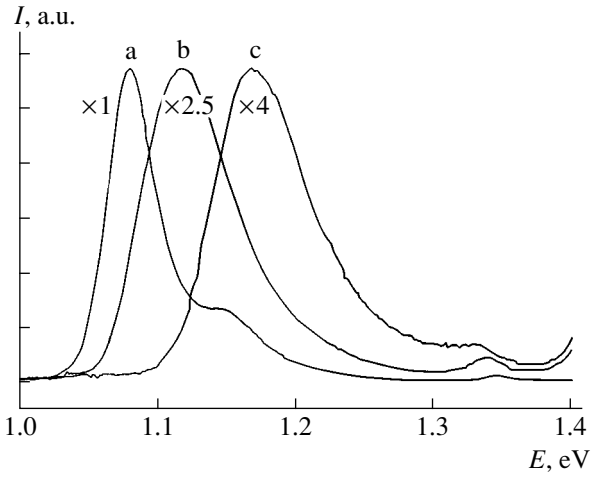

Fig. 2. Effect on the deposition temperature on the PL peak positions for the structures with an InAs layer thickness of 1.6 ML.

tion of tilted line reflections originating from the volume ones, which corresponded to the electron diffraction from side faces of the islands. As a characteristic time of the QD formation, we take the moment of the appearance of point reflections, while the appearance of the additional tilted reflections was used to estimate the time when the islands reach a quasi-equilibrium size.

Figure 1 shows the plots of the QD formation time versus the substrate temperature for the structures with 1.5 and 1.6 ML thick InAs layers. It is seen that the islands are formed in both cases. For the deposited film thickness of 1.5 ML and the substrate temperature of 485°C, no formation of QDs was observed for the exposure time exceeding 90 s. The formation of QDs in the structures with 1.5-ML-thick InAs layer takes place much later than in the samples with 1.6-ML-thick InAs layer.

Figure 2 shows the PL spectra of the structures with an effective InAs layer thickness of 1.6 ML. The spectra correspond to the samples grown at a temperature of (a) 485, (b) 450, and (c) 420°C. The typical PL spectrum contains at least two peaks. The first of these (a long-wavelength peak at about 1.1–1.2 eV) corresponds to the emission from QDs, and the second (a short-wavelength peak at about 1.35 eV) corresponds to the emission from the WL. An analysis of the PL spectra reveals several characteristic features. First, the PL intensity decreases on lowering the growth temperature of the InAs layer and the covering GaAs layer. This is evidently caused by a decrease in the quality of epitaxial layers formed at lower substrate temperatures due to uncontrolled incorporation of impurity centers responsible for nonradiative recombination. This trend is also manifested in the second series of samples. The second specific feature is that, as the substrate temperature decreases, the QD and WL photoluminescence peaks shift to shorter and longer wavelengths, respectively (Figs. 3 and 4). A comparison of these figures shows that the characteristic QD size increases both with decreasing total amount of the deposited material and with increasing temperature. The characteristic time of the QD formation is shorter for lower temperatures of the substrate and for greater total amounts of deposited InAs. It should be noted that a special feature of the system studied is that the time of QD formation decreases with decreasing temperature of the substrate, irrespective of the thickness of deposited InAs.

The results obtained in this study can be interpreted within the framework of a theoretical model of the QD formation in mismatched heteroepitaxial systems [5]. This model considers the process of QD nucleation and

Sample parameters and PL peak positions

Sample	InAs film thickness, ML	T_{sub}, °C	QD formation time, s	QD peak position, eV	WL peak position, eV
a	1.6	485	13	1.079	1.346
b	1.6	450	4	1.117	1.339
c	1.6	420	2	1.169	1.333
d	1.5	485	>90	–	1.377
e	1.5	450	20	1.130	1.345
f	1.5	420	15	1.140	1.341

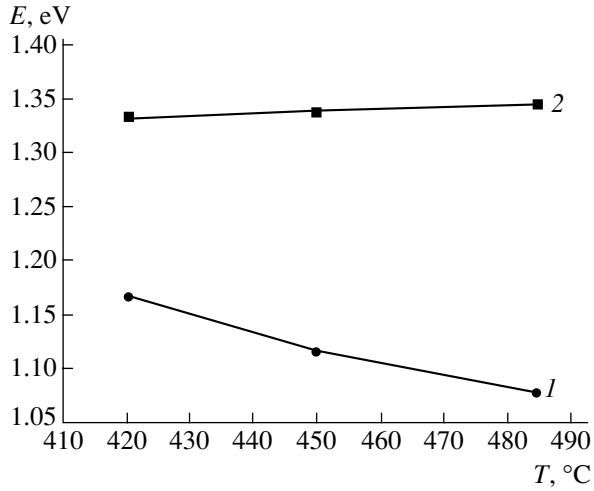

Fig. 3. Plots of the positions of the PL peaks of (*1*) quantum dots and (*2*) wetting layer versus substrate temperature for the structures with an InAs layer thickness of 1.6 ML.

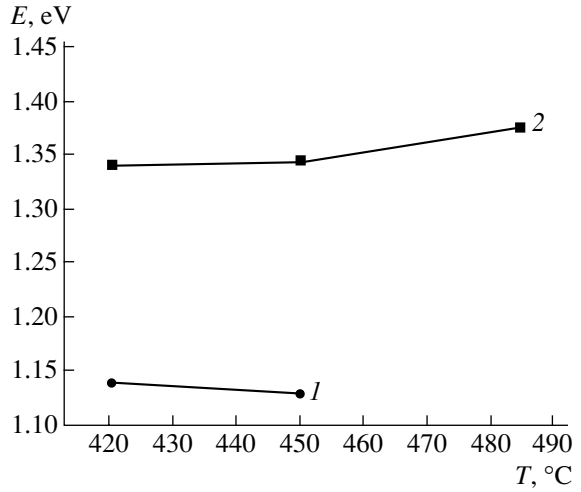

Fig. 4. Plots of the positions of the PL peaks of (*1*) quantum dots and (*2*) wetting layer on the substrate temperature for the structures with an InAs layer thickness of 1.5 ML.

growth according to the Stranski–Krastanov mechanism from a metastable WL with a thickness exceeding an equilibrium value determined by the balance of elastic and wetting forces [6]. The driving force of the transition from 2*D* to 3*D* growth is the relaxation of elastic stresses in the islands; and the basic growth mechanism is the supply of material from the WL with the diffusion flux due to a difference between the elastic energies in the WL and the island [7]. Estimations show that an equilibrium thickness of the WL for the InAs/GaAs(100) system is approximately 1 ML. The critical thickness of the WL, which corresponds to the maximum rate of the island nucleation with the In flux on, is approximately 1.7 ML. Hence, the range from 1 to 1.7 ML (subcritical interval) corresponds to a region of the WL metastability such that the formation of coherent islands is already energetically profitable but still occurs at a noticeably lower rate than that in the case of supercritical thicknesses. A theoretical analysis of the nucleation and growth of islands at subcritical thicknesses within the framework of the model adopted [5] leads to the following conclusions. The nucleation rate and the QD density increase, while the characteristic QD size decreases, with increasing amount of the deposited material. This conclusion completely agrees with our experimental results. The temperature dependence of the characteristic QD size exhibits two different trends depending on the WL thickness. With increasing temperature, the quasi-equilibrium size of QDs decreases for thin WLs and increases for WLs with the thicknesses close to critical, as it does in the case of supercritical thicknesses [5]. This very case is observed in our experiments with the WL thicknesses of 1.5–1.6 ML. Behavior of the characteristic QD formation time requires special investigation. The results of a theoretical investigation of the QD formation at a subcritical WL thickness will be presented in more detail in a separate publication.

Thus, we have experimentally found that islands in the InAs/GaAs(100) system are formed when the thickness of the deposited InAs film is below the critical value for the transition from two- to three-dimensional growth. It was shown that the island formation time depends both on the thickness of the deposited InAs film and on the substrate temperature. As the InAs film thickness decreases by 0.1 ML, all other factors being the same, the island formation time increases by an order of magnitude; at lower substrate temperatures, the transition to the islands–WL system proceeds faster. The results obtained in this paper have been interpreted within the framework of a theoretical model of the kinetics of the QD formation in mismatched heteroepitaxial systems.

Acknowledgments. This study was partly supported by the scientific programs of the Ministry of Industry, Science, and Technology of the Russian Federation.

G.E. Cirlin is grateful to Alexander von Humboldt Stiftung.

REFERENCES

1. V. M. Ustinov *et al.*, Nanotechnology **11**, 397 (2000).
2. V. M. Ustinov and A. E. Zhukov, Semicond. Sci. Technol. **15**, R41 (2000).
3. G. E. Cirlin, G. M. Guryanov, A. O. Golubok, *et al.*, Appl. Phys. Lett. **67**, 97 (1995).
4. G. M. Guryanov, G. E. Cirlin, A. O. Golubok, *et al.*, Surf. Sci. **352–354**, 646 (1996).
5. A. A. Tonkikh, V. G. Dubrovskiĭ, G. E. Cirlin, *et al.*, Phys. Status Solidi B **236**, R1 (2003).
6. P. Müller and R. Kern, Appl. Surf. Sci. **102**, 6 (1996).
7. A. V. Osipov, F. Schmitt, S. A. Kukushkin, and P. Hess, Appl. Surf. Sci. **188**, 156 (2002).

Translated by M. Basieva

Technical Physics Letters, Vol. 29, No. 8, 2003, pp. 694–697. Translated from Pis'ma v Zhurnal Tekhnicheskoĭ Fiziki, Vol. 29, No. 16, 2003, pp. 80–88.

Justification of the Method of Moments in the Theory of Diffraction

S. I. Éminov

Novgorod State University, Novgorod, Russia
e-mail: tel@novsu.ac.ru; theorphy@novsu.ac.ru

Received March 11, 2003

Abstract—Questions related to justification of the method of moments are considered. It is shown that the structure of many equations of the theory of diffraction ensures convergence of the approximated solutions to exact ones. The operators of the diffraction problems can be presented as the sums of a positive operator and a completely continuous operator. *© 2003 MAIK "Nauka/Interperiodica".*

Formulation of the problem. The problem of electromagnetic wave diffraction on an ideally conducting surface is described by an equation of the following type:

$$Lj = e, \tag{1}$$

where L is a linear, integral or integrodifferential, operator (integration is performed over the surface of diffraction), j is the surface current density, and e is the primary electric field on the diffraction surface.

Equation (1) can be solved by analytical methods, but numerical techniques such as the method of moments are also frequently employed.

For formulating the method of moments, consider two systems of functions, $\{\varphi_n\}_{n=1}^{+\infty}$ and $\{\psi_n\}_{n=1}^{+\infty}$, which are complete in a certain functional space. Expanding an unknown function in the former basis set,

$$j = \sum_{m=1}^{N} C_m \varphi_m, \tag{2}$$

we substitute this expression into Eq. (1) and multiply both parts of the relation by ψ_n in the L_2 space. As a result, we obtain a system of linear algebraic equations

$$\sum_{m=1}^{N} C_m (L\varphi_m, \psi_n) = (e, \psi_n), \quad 1 \le n \le N, \tag{3}$$

where $(\cdot, \cdot)$ denotes multiplication in L_2 (i.e., multiplication with subsequent integration).

Upon solving system (3), we obtain the unknown coefficients C_m and determine by formula (2) an approximate value of the current density corresponding to a preset value of N. This is the essence of the method of moments; for $\psi_n = \varphi_n$, the procedure coincides with that according to the Galerkin method.

The method of moments was used to solve a large number of diffraction problems [1–4]. Note, however, that the books cited almost do not consider the problems related to justification of the numerical methods employed and the convergence of approximate solutions to the exact ones. Development of the numerical methods for solving the integral equations has proved to be much simpler than justification of these methods. The latter requires a profound analysis of the structure of integral equations.

The aim of this study was to justify the method of moments in application to a broad range of diffraction problems.

The equation of *H*-polarized wave diffraction on a stripe. Reduction to an integral equation of the second kind. The equation of H-polarized wave diffraction on a stripe can be written in the following form [5]:

$$Lj \equiv \int_{-\infty}^{+\infty} f(\xi)\tilde{j}(\xi)\exp(-ix\xi)d\xi = e(x). \tag{4}$$

Here, $\tilde{j}(\xi)$ is the Fourier transform of the unknown function,

$$\tilde{j}(\xi) = \int_{-e}^{e} j(x')\exp(ix'\xi)dx' \tag{5}$$

(where the integral is taken over the stripe width), and the function $f(\xi)$ is expressed as

$$f(\xi) = \sqrt{\xi^2 - k^2}, \tag{6}$$

where k is the wavenumber. For simplicity, all constants in writing Eq. (4) are related to the right-hand side.

The problem of electromagnetic wave diffraction on a round cylinder or a dipole [6] can be also reduced to an equation of the type (4), in which case $f(\xi)$ is expressed in terms of the Bessel functions. For the subsequent considerations, it is important to note that the

1063-7850/03/2908-0694$24.00 © 2003 MAIK "Nauka/Interperiodica"

asymptotic behavior of this function is the same as that of function (6):

$$f(\xi) - |\xi| \longrightarrow 0 \quad \text{for} \quad \xi \longrightarrow \pm\infty. \tag{7}$$

According to (7), the operator L can be represented as a sum of two operators,

$$Lj \equiv Aj + Bj = e, \tag{8}$$

where

$$Aj = \int \sqrt{\xi^2 + 1}\,\tilde{j}(\xi)\exp(-ix\xi)d\xi, \tag{9}$$

$$Bj = \int (f(\xi) - \sqrt{\xi^2 + 1})\,\tilde{j}(\xi)\exp(-ix\xi)d\xi. \tag{10}$$

The integration in (9) and (10) is performed over the entire line (here and below, the integration limits are omitted).

Now let us consider the properties of operator A, which is positive in L_2 because

$$(Aj, j) = \int \sqrt{\xi^2 + 1}\,|\tilde{j}(\xi)|\,d\xi.$$

In fact, operator A is not only positive, it is positively definite in L_2 [6, 7]. Being positive, operator A has the inverse operator A^{-1}. Multiplying both parts of Eq. (8) by A^{-1}, we obtain

$$j + A^{-1}B = A^{-1}e. \tag{11}$$

Consider Eq. (11) in the energy space of the positively definite operator A, which coincides [7] with the Sobolev–Slobodetskii space $\overset{\circ}{H}_{1/2}$.

Using the aforementioned asymptotic behavior (7), it is possible to show that the operator $A^{-1}B$ is completely continuous in the $\overset{\circ}{H}_{1/2}$ space. Therefore, Eq. (11) is a Fredholm-type equation of the second kind, to which the method of moments is applicable.

Substituting expression (2) into Eq. (11) and multiplying both parts of the relation by ψ_n in the $\overset{\circ}{H}_{1/2}$ space, we obtain a system of linear algebraic equations

$$\sum_{m=1}^{N} C_m[\varphi_m, \psi_n] + \sum_{m=1}^{N} (B\varphi_m, \psi_n) = (e, \psi_n), \quad 1 \le n \le N, \tag{12}$$

where $[\cdot, \cdot]$ denotes the scalar product in $\overset{\circ}{H}_{1/2}$ determined by the formula

$$[u, v] = (Au, v). \tag{13}$$

Using the Fredholm character of Eq. (11), it is possible to show that the system of equations (12) for large N has a unique solution and that an approximate equation obtained using formula (2) converges to the exact solution of Eq. (11). Here, the functions $\{\varphi_n\}_{n=1}^{+\infty}$ and $\{\psi_n\}_{n=1}^{+\infty}$ must be complete exactly in the $\overset{\circ}{H}_{1/2}$ space.

In the theory of diffraction, the functions φ_n are usually chosen so as to exactly describe the properties of a solution. Then, by properly selecting the functions ψ_n, it is possible to facilitate calculation of the matrix elements for the system of equations (12).

According to the definition of operators A and B, the system of equations (3), obtained upon application of the method of moments to the initial equation, exactly coincides with the system of equations (12) obtained by applying the same method to a Fredholm- type integral equation of the second kind. This coincidence ensures a strict mathematical justification of the method of moments.

Although operator A is not uniquely determined, the energy space is uniquely defined by Eq. (1). This is a remarkable property of equations of the theory of diffraction: the functional space is uniquely defined by an operator entering into the equation, admitting no uncertainty in choosing the space of solutions.

The equation of *E*-polarized wave diffraction on a stripe. Reduction to an integral equation of the second kind. The equation of E-polarized wave diffraction on a stripe, whereby the currents flow parallel to the stripe edge, can be written in the following form [5]:

$$Lj \equiv \int_{-\infty}^{+\infty} f(\xi)\tilde{j}(\xi)\exp(-ix\xi)d\xi = e(x), \tag{14}$$

where $f(\xi) = \dfrac{1}{\sqrt{\xi^2 - k^2}}$.

Let us separate the principal positive operator in Eq. (14),

$$Lj = Aj + Bj = e, \tag{15}$$

where

$$Aj = \int \frac{1}{\sqrt{\xi^2 + 1}}\,\tilde{j}(\xi)\exp(-ix\xi)d\xi, \tag{16}$$

$$Bj = \int \left(f(\xi) - \frac{1}{\sqrt{\xi^2 + 1}} \right) \tilde{j}(\xi)\exp(-ix\xi)d\xi. \tag{17}$$

Note that this operator is only positive, rather than positively definite, in the L_2 space. For this reason, the energy space is wider than L_2. As is known, the energy space coincides [7] with the Sobolev–Slobodetskii space $\overset{\circ}{H}_{1/2}$. Being positive, operator A has the inverse operator A^{-1}. Multiplying both parts of Eq. (15) by A^{-1}, we obtain

$$j + A^{-1}Bj = A^{-1}e. \tag{18}$$

Again, it is possible to show that the operator $A^{-1}B$ is completely continuous in the energy space of operator A and, hence, in the $\overset{\circ}{H}_{1/2}$ space. Here, operator A is unbounded and e must belong to the domain of operator A^{-1}. Therefore, Eq. (18) is a Fredholm-type equation of the second kind.

Once Eq. (18) is a Fredholm-type equation of the second kind, we the method of moments is applicable to this equation in the corresponding energy space. As a result, we obtain the same system of linear algebraic equations as that corresponding to the application of the method of moments to the initial equation in the L_2 space. Therefore, the method of moments is completely justified.

Thus, the justification of the method of moments in the problems of *E*- and *H*-polarized wave diffraction is based on separation of the principal positive operator and reduction of the equation to a Fredholm-type equation of the second kind. This approach is also applicable to the problems of diffraction on a cylindrical curvilinear surface, on a surface of revolution, and on periodic structures.

The above problems belong to the class of scalar problems. The next section is devoted to a vector problem of the diffraction of electromagnetic waves on a flat surface.

The equation of electromagnetic wave diffraction on a plane screen. Reduction to a Fredholm-type equation of the second kind. The diffraction of electromagnetic waves on a plane screen is described by a vector equation of the type

$$L\mathbf{j} = \mathbf{e}, \tag{19}$$

where L is a linear integral operator, $\mathbf{e}$ is the primary electric field on the screen, and $\mathbf{j}$ is the surface current density induced on both sides of the screen.

In order to formulate the method of moments, we introduce two systems of vector functions, $\{\boldsymbol{\varphi}_n\}$ and $\{\boldsymbol{\psi}_n\}$, expand the unknown function in the former basis set,

$$\mathbf{j} = \sum_{m=1}^{N} C_m \boldsymbol{\varphi}_m, \tag{20}$$

and substitute this expression into Eq. (19). Multiplying both parts of the relation by $\boldsymbol{\psi}_n$ in the $L_2 \oplus L_2$ space, we obtain a system of linear algebraic equations

$$\sum_{m=1}^{N} C_m (L\boldsymbol{\varphi}_m, \boldsymbol{\varphi}_n) = (\mathbf{e}, \boldsymbol{\varphi}_n), \tag{21}$$

where $(\cdot, \cdot)$ denotes multiplication in $L_2 \oplus L_2$ (i.e., the scalar product with subsequent integration over the screen surface S).

The vector equation describing the diffraction of electromagnetic waves on a plane screen is as follows [8]:

$$L\mathbf{j} = \iint \frac{1}{\sqrt{|\boldsymbol{\xi}|^2 - k^2}} (-\boldsymbol{\xi}(\boldsymbol{\xi} \cdot \tilde{\mathbf{j}}) + k^2 \tilde{\mathbf{j}}) \times \exp(-i(\mathbf{x} \cdot \boldsymbol{\xi})) d\boldsymbol{\xi}_1 d\boldsymbol{\xi}_2 = \mathbf{e}, \tag{22}$$

where $\mathbf{j}(j_1(x_1, x_2), j_2(x_1, x_2))$ is the surface current density, $\mathbf{x} \cdot \boldsymbol{\xi} = x_1\xi_1 + x_2\xi_2$, and $\tilde{\mathbf{j}}(\tilde{j}_1(\xi_1, \xi_2), \tilde{j}_2(\xi_1, \xi_2))$ is the Fourier transform of the current density,

$$\tilde{j}_1(\xi_1, \xi_2) = \iint_S j_i(x_1, x_2) \exp(ix_1\xi_1 + ix_2\xi_2) dx_1 dx_2, \quad i = 1, 2,$$

where the integral is taken over the screen surface S.

What are the conditions that the boundary of the diffraction region must satisfy? For the continuity of operators encountered in this problem, it is sufficient that the boundary satisfy the Lifshits conditions. This circumstance allows us to consider the regions with smooth boundaries and rectangular screens.

Let us introduce the operator

$$A\mathbf{j} = \iint \frac{1}{\sqrt{|\boldsymbol{\xi}|^2 + 1}} (\boldsymbol{\xi}(\boldsymbol{\xi} \cdot \tilde{\mathbf{j}}) + \tilde{\mathbf{j}}) \exp(-i(\mathbf{x} \cdot \boldsymbol{\xi})) d\boldsymbol{\xi}_i d\boldsymbol{\xi}_2. \tag{23}$$

Since this operator is positive, we can define the energy space H of this operator. The scalar product in H is defined as

$$[\mathbf{j}, \mathbf{j}] = (A\mathbf{j}, \mathbf{j}) = \iint \frac{1}{\sqrt{|\boldsymbol{\xi}|^2 + 1}} (|\boldsymbol{\xi} \cdot \tilde{\mathbf{j}}|^2 + |\tilde{\mathbf{j}}|^2) d\xi_1 d\xi_2. \tag{24}$$

As was demonstrated in [8], the space H can be presented as a direct sum of subspaces H_1 and H_2 such that

$$H_1 = \{\mathbf{j} \in H : \xi_1 \tilde{j}_1 + \xi_2 \tilde{j}_2 = 0\},$$
$$H_2 = \{\mathbf{j} \in H : \xi_2 \tilde{j}_1 - \xi_1 \tilde{j}_2 = 0\}.$$

Multiplying both parts of Eq. (22) by A^{-1}, we obtain

$$K\mathbf{j} \equiv A^{-1}L\mathbf{j} = A^{-1}\mathbf{e}. \tag{25}$$

Let us consider this vector equation in the energy space H. As can be readily shown, for $\mathbf{u}_i \in H_i$, $\mathbf{v}_j \in H_j$ ($i = 1, 2$; $j = 1, 2$) and $i \neq j$,

$$[Ku_i, v_j] = 0, \tag{26}$$

which implies that subspaces H_1 and H_2 are invariant subspaces of the operator K. For this reason, Eq. (25) can be separated into two independent equations

$$K\mathbf{j}_i = \mathbf{f}_i, \quad i = 1, 2, \tag{27}$$

where $\mathbf{j} = \mathbf{j}_1 + \mathbf{j}_2$, $A^{-1}\mathbf{e} = \mathbf{f}_1 + \mathbf{f}_2$, $\mathbf{j}_1 \in H_1$, $\mathbf{j}_2 \in H_2$, $\mathbf{f}_1 \in H_1$, and $\mathbf{f}_2 \in H_2$.

Separating a positive operator for $\mathbf{j}_1 \in H_1$ and $\mathbf{v}_1 \in H_1$, we obtain

$$[K\mathbf{j}_1, \mathbf{v}_1] = [A^{-1}L\mathbf{j}_1, \mathbf{v}_1] = (L\mathbf{j}_1, \mathbf{v}_1)$$
$$= \iint \frac{k^2}{\sqrt{|\boldsymbol{\xi}|^2 - k^2}} \tilde{\mathbf{j}}_1 \cdot \bar{\tilde{\mathbf{v}}}_1 d\xi_1 d\xi_2 = \iint \frac{k^2}{\sqrt{|\boldsymbol{\xi}|^2 + 1}} \tilde{\mathbf{j}}_1 \cdot \bar{\tilde{\mathbf{v}}}_1 d\xi_1 d\xi_2 \quad (28)$$
$$+ \iint \left(\frac{k^2}{\sqrt{|\boldsymbol{\xi}|^2 - k^2}} - \frac{k^2}{\sqrt{|\boldsymbol{\xi}|^2 + 1}} \right) \tilde{\mathbf{j}}_1 \cdot \bar{\tilde{\mathbf{v}}}_1 d\xi_1 d\xi_2.$$

By the same token, separating the principal positive operator for $\mathbf{j}_2 \in H_2$ and $\mathbf{v}_2 \in H_2$, we have

$$[-K\mathbf{j}_2, \mathbf{v}_2] = -[A^{-1}L\mathbf{j}_2, \mathbf{v}_2] = -(L\mathbf{j}_2, \mathbf{v}_2)$$
$$= \iint \sqrt{|\boldsymbol{\xi}|^2 - k^2} \tilde{\mathbf{j}}_2 \cdot \bar{\tilde{\mathbf{v}}}_2 d\xi_1 d\xi_2$$
$$= \iint \sqrt{|\boldsymbol{\xi}|^2 + 1} \tilde{\mathbf{j}}_2 \cdot \bar{\tilde{\mathbf{v}}}_2 d\xi_1 d\xi_2 \quad (29)$$
$$+ \iint (\sqrt{|\boldsymbol{\xi}|^2 + k^2} - \sqrt{|\boldsymbol{\xi}|^2 + 1}) \tilde{\mathbf{j}}_2 \cdot \bar{\tilde{\mathbf{v}}}_2 d\xi_1 d\xi_2.$$

Using representation (28) and (29), one can readily show that Eqs. (27) are equivalent to Fredholm-type equations of the second kind.

Applying the method of moments to Fredholm-type equation of the second kind, we obtain a system of linear algebraic equations coinciding with that obtained to the application of the same method to the initial equation. Therefore, the method of moments is completely justified in application to the vector problems of diffraction.

REFERENCES

1. *Computer Techniques for Electromagnetics*, Ed. by R. Mitra (Pergamon, Oxford, 1973; Mir, Moscow, 1977).
2. E. V. Zakharov and Yu. V. Pimenov, *Numerical Analysis of Radio Wave Diffraction* (Radio i Svyaz', Moscow, 1982).
3. V. V. Panasyuk, M. P. Savruk, and Z. T. Nazarchuk, *Method of Singular Integral Equations in Two-Dimensional Problems of Diffraction* (Naukova Dumka, Kiev, 1984).
4. E. N. Vasil'ev, *Excitation of Axi-Symmetric Bodies* (Radio i Svyaz', Moscow, 1987).
5. A. S. Il'inskiĭ and Yu. G. Smirnov, Radiotekh. Élektron. (Moscow) **39**, 23 (1994).
6. S. I. Éminov, Radiotekh. Élektron. (Moscow) **38**, 2160 (1993).
7. S. I. Éminov, Zh. Vychisl. Mat. Mat. Fiz. **41**, 450 (2001).
8. Yu. G. Smirnov, Differ. Uravneniya **28** (1), 136 (1992).

Translated by P. Pozdeev

Technical Physics Letters, Vol. 29, No. 8, 2003, pp. 698–700. Translated from Pis'ma v Zhurnal Tekhnicheskoĭ Fiziki, Vol. 29, No. 16, 2003, pp. 89–94.

The Efficiency of Enhanced Microwave Scattering on High-Frequency Fluctuations of the Plasma Density

E. Z. Gusakov and A. V. Surkov*

Ioffe Physicotechnical Institute, Russian Academy of Sciences, St. Petersburg, 194021 Russia

** e-mail: a.surkov@mail.ioffe.ru*

Received March 25, 2003

Abstract—The enhanced scattering of the extraordinary wave in an inhomogeneous magnetically active plasma in the vicinity of the upper hybrid resonance has been theoretically studied in the case when the scattering proceeds with a significant frequency shift. An approximated formula is obtained, which describes the scattering efficiency as a function of the radial wavenumber of the scattering fluctuation. This approximation can be used for numerical modeling. © *2003 MAIK "Nauka/Interperiodica".*

Introduction. The method of enhanced microwave scattering in an inhomogeneous plasma [1], based on the measurement of a signal backscattered in the vicinity of the upper hybrid resonance, offers a convenient tool for studying fluctuations and waves in tokamak plasmas. Using this method, it is possible to measure both frequency and radial wavenumber spectra of the plasma density fluctuations. The efficiency of the enhanced microwave scattering on low-frequency oscillations [1] is described by a rapidly varying function of the radial wavenumber of the scattering fluctuation, which possesses a sharp dominating maximum hindering the measurement of the turbulence spectrum on the wavenumber scale.

However, the situation is more favorable when the scattering takes place on the high-frequency fluctuations. In this case, according to the results of numerical calculations, the scattering efficiency as a function of the radial wavenumber has a broad plateau predicted by the Wentzel–Kramers–Brillouin (WKB) approximation. This behavior simplifies interpretation of the results obtained using the enhanced microwave scattering on the oscillations of sufficiently high frequency, for example, in the region of lower hybrid waves [2, 3].

We have studied the efficiency of enhanced microwave scattering for a significant frequency shift between the scattered signal and the probing wave, determined the peak position, and evaluated the plateau level. Based on these results, we propose an approximate formula describing a transition of the scattering efficiency in the WKB approximation to the plateau regime.

Frequency dependence of the enhanced scattering efficiency. Consider a plasma in a magnetic field directed along the z axis. Let a probing extraordinary wave with the frequency ω_1, possessing an upper hybrid resonance in the plasma, to propagate in the plasma density gradient direction x. Following [1], let us use the reciprocity theorem to write an expression for the backscattered wave signal intensity, assuming that the probing wave and the scattered signal are received by the same antenna:

$$A_s(\omega_2) = \frac{i\omega_1}{16\pi n_e}\sqrt{P_i}\int_{-\infty}^{+\infty}\frac{d\mathbf{q}}{(2\pi)^3}\delta n_{\mathbf{q},\Omega} \times \int_{-\infty}^{+\infty} d\mathbf{r}E^+(x_2 - x, y, z)E(x_1 - x, y, z)e^{-i\mathbf{qr}}. \quad (1)$$

Here, ω_2 is the scattered wave frequency, $\omega_1 = \omega_2 + \Omega$, $x_{1,2}$ are the upper hybrid resonance positions corresponding to $\omega_{1,2}$ (in cases when the resonance frequency difference is insignificant, $x_{1,2} \approx x_{UH}$), $\delta n_{\mathbf{q},\Omega}$ is the spectral density of fluctuations, P_i is the probing wave power, E is the distribution of the resonance electric field component of the probing weave (per unit power), and E^+ is the same field for the reverse direction of magnetic field in the plasma.

Assuming that the plasma density has a linear profile in the vicinity of the upper hybrid resonance, the resonance component of the extraordinary wave field can be written according to [1] as

$$E(\xi_{1,2}, y, z) = \sqrt{\frac{8}{\gamma^2 l\omega_{1,2}}}D(y, z) \times \int_0^{+\infty}\exp\left[i\left(\frac{\kappa^3}{3} - \frac{b}{\kappa} + \xi_{1,2}\kappa\right)\right]d\kappa, \quad (2)$$

where $\gamma = (l_T/l)^{2/3}$, $l_T^2 = 3v_{Te}^2/(3\omega_{ce}^2 - \omega_{pe}^2)|_{x = x_{UH}}$ is a parameter related to the thermal motion of electrons, l is the scale of the plasma density inhomogeneity, $D(y, z)$ is a factor related to the antenna directivity,

$\xi_{1,2} = (x - x_{1,2})/(\gamma l)$, $b = (k_c l)^2\gamma$, $k_c = \omega_{ce}(x_{UH})/c$, and ω_{ce} is the electron cyclotron frequency.

Assuming statistical spatial homogeneity of the plasma density fluctuations, the average square modulus of the scattered signal intensity can be expressed as

$$\langle |A_s|^2 \rangle = \frac{P_i}{\gamma^2 n_e^2} \int_{-\infty}^{+\infty} \frac{d\mathbf{q}}{(2\pi)^3} |\delta n_{\mathbf{q},\Omega}|^2 |F(q_y, q_z)|^2 U(\gamma l q_x), \quad (3)$$

where

$$F(q_y, q_z) = \int_{-\infty}^{+\infty} dy dz D(y, z) D^+(y, z) e^{-iq_y y - iq_z z}, \quad (4)$$

$$U(p) = \frac{p^2}{4} \left| \int_{-1}^{1} \exp\left[\frac{ip^3}{4}\kappa^2 - \frac{4ib}{p(1-\kappa^2)} + \frac{ip\Delta}{2}\kappa \right] d\kappa \right|^2, \quad (5)$$

$p = \gamma l q_x$ and $\Delta = (x_1 - x_2)/(\gamma l)$. Figure 1 shows a plot of $U(\gamma l q_x)$ versus radial projection of the fluctuation wavevector q_x calculated using the typical experimental values of parameters (electron temperature and density in the vicinity of the upper hybrid resonance, $T_e \sim 100$ eV and $n_e \sim 1.8 \times 10^{12}$ cm^{-3}, respectively; magnetic induction, $B \sim 9$ kG; characteristic inhomogeneity length, $l \sim 1$ cm [3]) determined on the FT-2 tokamak for the scattering on lower hybrid waves excited by an external generator at a frequency of $f_{LH} = 917.6$ MHz. The probing wave frequency is $f_i = \omega_1/(2\pi) = 27.975$ GHz. In this case,

$$x_1 - x_2 = \frac{8\pi^2 f_i f_{LH}}{\left| \partial\omega_{pe}^2/\partial x + \partial\omega_{ce}^2/\partial x \right|_{x = x_{UH}}} \approx l \frac{8\pi^2 f_i f_{LH}}{\omega_{pe}^2(x_{UH})}. \quad (6)$$

Let us determine the position of the sharp maximum of $U(\gamma l q_x)$ by equating to zero the first and second derivatives of the phase in the exponent of expression (5). The position of the maximum, $p_{\max}$, is determined by the value of $\alpha = \Delta/p_*^2 = (x_1 - x_2)/(4k_c l l_T)$, where $p_* = 2b^{1/4}$. The function $p_{\max}(\alpha)$ is virtually linear and can be written (in a broad range of the problem parameter $\Delta/p_*^2 \sim 2$–7) as $p_{\max}/p_* \approx 0.22\alpha + 1.6$. The corresponding radial wavenumber of the scattering fluctuations is

$$q_{\max} = 2\sqrt{\frac{k_c}{l_T}} \left[0.22 \frac{x_1 - x_2}{4k_c l l_T} + 1.6 \right]. \quad (7)$$

The maximum scattering efficiency in the range under consideration is roughly described as $U_{\max} \sim 2 - 0.1\alpha$. In the above case, $\alpha \approx 5.7$ yields $p_{\max} \approx 2.9 p_*$, which corresponds to $q_x \approx 270$ cm^{-1} and a peak height of $U_{\max} \sim 1.5$.

An analysis of the integral in expression (5) using the stationary phase method reveals three regions in $U(p)$ at $p < p_{\max}$. The region of $p \ll p_*$ corresponds to scattering under the conditions of applicability of the approximation of geometric optics. Here, the scattering efficiency is independent of the resonance shift Δ:

$$U(\gamma l q_x) \approx \frac{\pi\gamma^2 l q_x^3}{16 k_c^2}. \quad (8)$$

A plateau appears for $\alpha^{-1/3} < p/p_* < \alpha^{1/2}$. In this region, the scattering efficiency is independent of q_x:

$$U(\gamma l q_x) \approx \frac{\pi\gamma^2 k_c l^{5/2}}{(x_1 - x_2)^{3/2}}. \quad (9)$$

As the parameter p increases in the interval of $p_*\alpha^{1/3} < p < p_{\max}$, the function $U(p)$ exhibits a decrease. All the expressions for U can be approximated by a general formula

$$U(p) = \frac{\pi p^3}{p_*^4 \{1 + 4(p/p_*)^3 [(p/p_*)^2 + \Delta/p_*^2]^{3/2}\}}, \quad (10)$$

which is applicable for $p < p_{\max}$. This function is depicted by a dashed curve in Fig. 2.

Thus, the efficiency of the enhanced microwave scattering is successfully approximated by formula (10), pro-

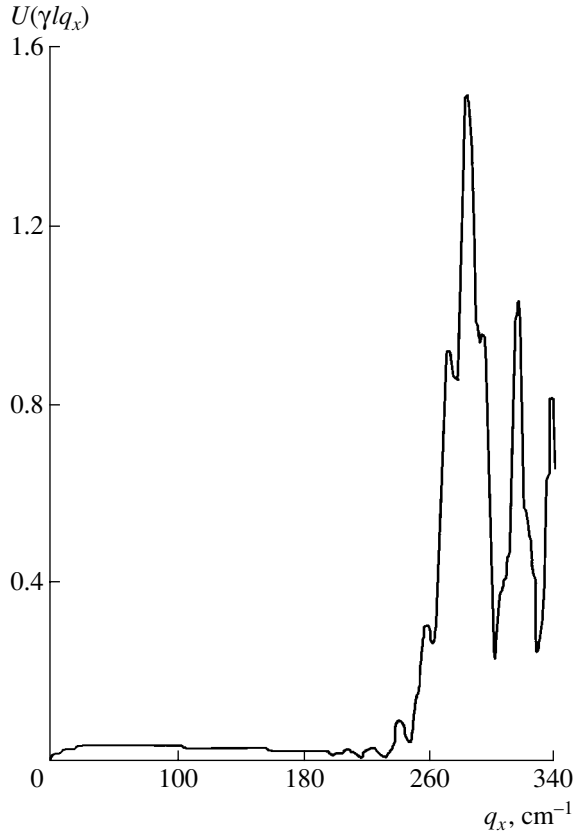

Fig. 1. The efficiency of enhanced microwave scattering versus radial projection of the scattering fluctuation wavevector.

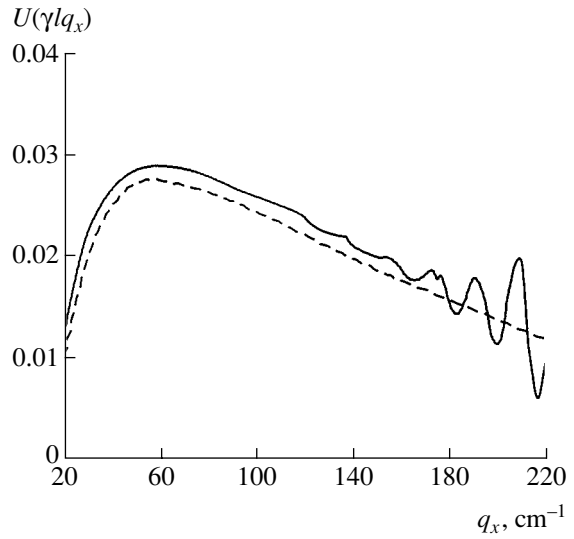

Fig. 2. Approximation of the scattering efficiency for $p < p_{\max}$.

vided that the short-wave component with $q_x \gtrsim q_{\max}$ corresponding to the maximum of $U(\gamma l q_x)$ is suppressed in the spectrum of excited oscillations.

Conclusions. We have analytically described the efficiency of the enhanced microwave scattering as a function of the radial projection of the scattering fluctuation wavevector in the case of a significant frequency shift between the scattered signal and the probing wave. The position of the maximum and the level of plateau agree well with the results of numerical calculations. An approximated formula is proposed that describes the transition of the scattering efficiency predicted by the WKB approximation to the plateau regime. This formula considerably simplifies calculations of the scattering efficiency and makes possible rapid simulation of the enhanced microwave scattering by means of the numerical codes describing the extraordinary wave propagation in a real experimental geometry.

Acknowledgments. This study was supported by the Russian Foundation for Basic Research (project nos. 02-02-17591 and 03-02-06148) and by a contract with the Ministry of Industry, Science, and Technology of the Russian Federation (no. 40.006.1.1.1128).

REFERENCES

1. K. M. Novik and A. D. Piliya, Plasma Phys. Controlled Fusion **36**, 357 (1994).
2. A. D. Gurchenko, E. Z. Gusakov, V. V. Korkin, *et al.*, Fiz. Plazmy **28**, 532 (2002) [Plasma Phys. Rep. **28**, 489 (2002)].
3. A. B. Altukhov, A. D. Gurchenko, E. Z. Gusakov, *et al.*, in *Proceedings of the 29th EPS Conference on Plasma Physics and Controlled Fusion, Montreux, 2002*, Vol. 26B.

Translated by P. Pozdeev